Heinrich Heine
Universität
Düsseldorf

Interfacial Assembly of Core-Shell Microgels: Surface Tension-Driven Evolution and Structural Discrepancies between *in-situ* and *ex-situ* Observations

Inaugural-Dissertation

zur Erlangung des Doktorgrades
der Mathematisch-Naturwissenschaftlichen Fakultät
der Heinrich-Heine-Universität Düsseldorf

vorgelegt von

Yichu Zhou
geboren in Xuzhou

Düsseldorf, March 2025

aus dem Institut für Physikalische Chemie I
der Heinrich-Heine-Universität Düsseldorf

Gedruckt mit der Genehmigung der
Mathemathisch-Naturwissenschaftlichen Fakultät der
Heinrich-Heine-Universität Düsseldorf

Berichterstatter:

1. Prof. Dr. Matthias Karg
2. Prof. Dr. Ivo Buttinoni

Tag der mündlichen Prüfung: 01.03.2025

Eidesstattliche Erklärung

Ich, Yichu Zhou, versichere an Eides statt, dass die Dissertation von mir selbständig und ohne unzulässige fremde Hilfe unter Beachtung der „Grundsätze zur Sicherung guter wissenschaftlicher Praxis an der Heinrich-Heine-Universität Düsseldorf „erstellt worden ist. Alle verwendeten Quellen und Hilfsmittel sind als solche gekennzeichnet und im Literaturverzeichnis aufgelistet.
Die vorliegende Dissertation wurde ausschließlich an der Mathemathisch-Naturwissenschaftlichen Fakultät der Heinrich-Heine-Universität Düsseldorf vorgelegt. Es wurden keine früheren Promotionsversuche unternommen.

_____ _____

Ort, Datum Unterschrift

Table of Content

Danksagung

An erster Stelle möchte ich Prof. Matthias Karg meinen tief empfundenen Dank für seine außergewöhnliche Betreuung und unerschütterliche Unterstützung während meiner Promotion aussprechen. Seine strenge und zugleich äußerst detaillierte Anleitung, sein hoher Anspruch sowie seine bemerkenswerte Geduld haben nicht nur diese Dissertation maßgeblich geprägt, sondern auch mein persönliches Wachstum als Wissenschaftler gefördert. Besonders profitiert habe ich von seinem präzisen Arbeitsstil und seinem ausgeprägten Gespür für zukunftsweisende Forschungsthemen. In den herausforderndsten Phasen meiner Promotion waren es seine herzlichen Worte und sein festes Vertrauen in mich, die mir die Kraft gegeben haben, weiterzumachen. Seine Begeisterung, mich aktiv in Konferenzen und wissenschaftliche Austauschformate einzubinden, hat meinen Horizont erheblich erweitert und mich zu einer noch leidenschaftlicheren Auseinandersetzung mit der Forschung inspiriert.

Mein aufrichtiger Dank gilt auch Prof. Dr. Ivo Buttinoni für die Übernahme der Koreferatsrolle dieser Arbeit. Ich schätze seinen Einsatz und die investierte Zeit zur Begutachtung sehr. Sein konstruktives Feedback war von großem Wert für mich.

Ein besonderer Dank geht an Prof. Dr. Jérôme J. Crassous für seine maßgebliche Unterstützung bei unserer Arbeit zur Monolayer Evolution. Seine fundierten Anregungen haben entscheidend dazu beigetragen, die Ausrichtung unserer Forschung zu klären und die theoretischen Grundlagen zu stärken. Seine Unterstützung hat wesentlich dazu beigetragen, dass dieses Projekt Gestalt annehmen konnte. Ebenso möchte ich Prof. Dr. Igor I. Potemkin meinen tiefen Dank für die inspirierende Zusammenarbeit aussprechen. Die Einbindung von DPD-Simulationen

unter seiner Anleitung hat die wissenschaftliche Tiefe unserer Studie erheblich gesteigert und ihr eine neue Dimension verliehen.

Ganz besonders danke ich Dr. Andrey A. Rudov für seine herausragenden Beiträge im Bereich der Simulationen. Sein unermüdlicher Einsatz bei der Durchführung und wiederholten Überarbeitung der Simulationen war von unschätzbarem Wert. Ich bin ihm besonders dankbar, dass er während einer Konferenz aktiv auf mich zukam, was letztlich der Beginn einer sehr fruchtbaren und richtungsweisenden Zusammenarbeit war. Mein herzlicher Dank gilt auch Julia Fink, deren sorgfältige und gewissenhafte experimentelle Arbeit unsere Forschungsergebnisse wesentlich vertieft und untermauert hat. Ihre Präzision und Zuverlässigkeit haben das Gesamtbild unserer Kooperation entscheidend bereichert.

Ebenso danke ich von Herzen Marcel Krüsmann, Julian Sindram, Ekaterina Ponomareva, Kirsten Volk, Keumkyung Kuk, Marco Hildebrandt, Marius Otten, Vahan Abgarjan, Déborah Feller, Philipp Hammers, Julian Ringling und Jonathan Garthe für ihre tatkräftige Unterstützung – sowohl im beruflichen als auch im privaten Kontext. Ihre Hilfsbereitschaft und Freundschaft haben mir über all die Jahre hinweg viel bedeutet. Die Zusammenarbeit und die Zeit mit ihnen haben das tägliche Leben im Labor nicht nur produktiv, sondern auch sehr angenehm gemacht. Allen Mitgliedern unserer Arbeitsgruppe danke ich für das freundliche und kollegiale Miteinander. Die geteilten Erlebnisse, Diskussionen und gegenseitige Unterstützung haben meine Promotionszeit zu einer wertvollen und unvergesslichen Erfahrung gemacht.

Abschließend möchte ich meiner Familie und meinen Freunden von ganzem Herzen für ihre bedingungslose Liebe und emotionale Unterstützung danken. In den

schwersten Momenten haben mir ihre Ermutigung und ihr Vertrauen die nötige Kraft und Ausdauer gegeben. Ohne ihren unerschütterlichen Rückhalt wäre diese Dissertation nicht möglich gewesen.

List of Publications

1. **Yichu Zhou**, Jérôme J. Crassous, and Matthias Karg
   Core-shell microgels at air/water interfaces: Role of interfacial tension on monolayer evolution

   Published in *Langmuir*, 2025, 10.1021/acs.langmuir.4c05050

2. **Yichu Zhou**, Andrey A. Rudov, Julia Fink, Igor I. Potemkin, and Matthias Karg
   New insights into the assembly of core-shell microgels at air/water interfaces: Do we see what we are looking at?

   In preparation

3. Keumkyung Kuk, Vahan Abgarjan, Lukas Gregel, **Yichu Zhou**, Virginia Carrasco Fadanelli, Ivo Buttinoni, and Matthias Karg
   Compression of colloidal monolayers at liquid interfaces: in situ vs. ex situ investigation

   Published in *Soft Matter*, 2023, 19, 175-188

List of Conference Contributions

1. **Yichu Zhou** and Matthias Karg
   Poster presentation: Time-dependent extension behaviour of freely floating monolayers of hard-core/soft-shell colloids at air/water interfaces

   *School on Thermodynamics and energetics of soft matter systems (**2018**), Grenoble, France*

2. **Yichu Zhou** and Matthias Karg
   Poster presentation: Time-dependent extension behaviour of freely floating monolayers of hard-core/soft-shell colloids at air/water interfaces

   *Particle Based Materials Symposium (**2019**), Ulm, Germany*

3. **Yichu Zhou** and Matthias Karg
   Poster presentation: Poster presentation: Time-dependent extension behaviour of freely floating monolayers of hard-core/soft-shell colloids at air/water interfaces

   *The 33rd Conference of the European Colloid and Interface Society (ECIS) (**2019**), Leuven, Belgium*

4. **Yichu Zhou** and Matthias Karg
   Poster presentation: Poster presentation: Time-dependent extension behaviour of freely floating monolayers of hard-core/soft-shell colloids at air/water interfaces

   *16th Zsigmondy Colloquium of the German Colloid Society (**2020**), Dusseldorf, Germany*

5. **Yichu Zhou** and Matthias Karg
   Attended speaker and session chair
   Oral Presentation: Hard-core-/soft-shell colloids at air/water interfaces: Role of cross-linking density and interfacial tension

   *Virtual Symposium on Microgels (**2021**), Aachen, Germany*

List of Abbreviations and Symbols

2D	Two-dimensional
α	Deswelling ratio
α_{SW}	Interaction parameter between the shell (S) and water (W) beads
A	Hamaker constant (DLVO theory), Area
A_{ring}	Area of the ring
AFM	Atomic force microscopy
a. u.	Arbitrary units
β	Swelling ratio
b_i	Bound coherent scattering length of a nucleus
BIS	N,N'-methylenebisacrylamide
C	Empirical constants relating to volume fraction (Flory-Rehner theory)
CMC	Critical Micelle Concentration
CS	Core-shell
D	Diffusion coefficient / Empirical constants relating to volume fraction (Flory-Rehner theory) / separation distance (DLVO theory)
ΔS	Non-combinatorial entropy change
ΔH	Equivalent enthalpic contribution
$\Delta\rho_{\mathrm{SLD}}$	Difference in SLD between the polymer and solvent
d_{c-c}	Center-to-center distance
d_{core}	Core diameter
d_h	Hydrodynamic diameter
d_i	Average dimensions of the inhomogeneities
$d_{nominal}$	Nominal particle diameter
d_{ST}	Stern layer thickness
DLS	Dynamic Light Scattering
DLVO	Derjaguin-Landau-Verwey-Overbeek (theory)
DPD	Dissipative particle dynamics
E	Adsorption energy (at interfaces)
ε	Dielectric permittivity
ε_0	Dielectric permittivity of the suspending medium

ε_{ST}	Dielectric constant of the stern layer
η	Dynamic viscosity
et al.	And others (from Latin: et alii)
Ψ_6	Hexagonal bond-order parameter
F_{DLVO}	DLVO force for two spheres
$f(r_1, r_2)$, (r_1, r_2)	Grayscale of an image and related positional coordinate in the real 2D space
$F(k_1, k_2)$	Fourier Transform of $f(r_1, r_2)$.
FFT	Fast fourier transform
$g(r)$	Pair correlation function
Γ	Decay rate
γ	Surface/interfacial tension
$I(q)$	Scattering intensity
$I(t+\tau)$	Time-averaged intensity of scattered intensities
h	Planck's constant
h_{air}, h_{water}	Protrusion height, the region where the microgel extends into the air or water
κ	Inverse Debye length (DLVO theory)
k_B	Boltzmann constant
λ	Wavelength of incident radiation
LCST	Lower critical solution temperature
M_w	Molecular weight
MPS	Methacryloxypropyltrimethoxysilane
n	Number density of the particles / Exponent that controls the stiffness of the potential (DLVO theory)
N_A	Avogadro's number
N_c	Number of chains in the network
NIPAM	N-isopropylacrylamide
NMR	Nuclear magnetic resonance
Π	Osmotic pressure
Π_e, Π_{mix}	Elastic and mixing osmotic pressures (Flory-Rehner theory)
$P(k_1,k_2)$	Power spectrum
$P(q)$	Normalized form factor
PDI	Polydispersity index
PNIPAM	Poly(N-isopropylacrylamide)
PPS	Potassium peroxodisulfate

q	Momentum transfer
ρ_0	Bulk density, the number of molecules per unit volume
ρ_{app}	Apparent specific density
$\rho(r)$	Local density
r_c	Effective size of a simulation bead corresponding to a cluster of four water molecules
R_{core}	Radius of the core
R, R_h	Radius, Hydrodynamic radius
R_{2D}, R_{3D}, R_{HCR}	The radii of the contact areas of 2D, 3D and the contact spot for the inner shell of the microgels parts of the microgels at the interface when z=0
R_{SANS}	Effective microgel radius from SANS
σ_{surf}	Width of smeared microgel surface (SANS model)
$S(q)$	Interference of scattering from different particles
SAXS	Small-angle X-ray scattering
SANS	Small-angle neutron scattering
SDS	Sodium dodecyl sulfate
SEM	Scanning electron microscopy
SLD	Scattering length density
τ	Time lag
θ	Scattering angle / Contact angle (interface adsorption) / theta temperature
t	Time
T	Temperature
TEOS	Tetraethyl orthosilicate
TEM	Transmission electron microscopy
u	Soft-sphere effective interparticle potential
v_0, ϕ_0	Microgel volume and volume fraction in reference state
V_{core}	Volume of the rigid core
V_{cs}	Volume of the core-shell particle
V_{poly}	Volume of polymer in a particle
v_s	Molar volume of the solvent
VPT	Volume phase transition
VPTT	Volume phase transition temperature
χ	Flory-Huggins interaction parameter

Abstract

Core-shell microgels with rigid cores and soft, deformable hydrogel shells can assemble at air/water interfaces forming 2D microstructures. Understanding their interfacial behaviours is essential for controlling the monolayer structures and optimizing their further applications. Two critical aspects of this behaviour remain to be elusive: the impact of interfacial tension on monolayer evolution, and the accuracy of atomic force microscopy (AFM) in representing real interfacial microstructures. In this study, we systematically investigate these aspects through experimental and theoretical approaches, providing insights into both macroscopic and microscopic interfacial behaviours.

The strong adsorption of core-shell microgels at air/water interfaces is related to the reduction in interfacial tension that also causes the microgels to laterally deform. The degree of this deformation is typically controlled through the applied surface pressure. The impact of interfacial tension imbalances between monolayer-covered and microgel-free areas on monolayer evolution is a crucial factor in understanding the microgel monolayer evolution. By the addition of SDS or linear PNIPAM to adjust tension in microgel-free regions, freely floating monolayers expand, compress, or remain stable depending on the resulting tension imbalance, which can induce Marangoni flow. The global evolution of the monolayer was tracked, while local structural changes were analyzed using AFM. A comparison of core-shell microgels with identical silica cores but varying crosslinker densities reveals how deformability affects interfacial behaviour. These findings provide valuable insights into controlling 2D microstructures without relying on a Langmuir trough.

The study also addresses discrepancies between AFM imaging and the actual interfacial arrangement of microgels. While AFM is widely used for *ex-situ* analysis, whether it accurately reflects *in-situ* structures remains uncertain. Under high compression, AFM imaging suggests solid-solid phase transitions marked by abrupt reductions in interparticle distance. However, simulations predict continuous hexagonal ordering, indicating that these transitions are artefacts introduced during monolayer transfer and drying. Additionally, substrate hydrophobicity is shown to influence the

final AFM-observed structure: hydrophilic substrates promote clustering and void formation, while hydrophobic substrates better preserve the native monolayer arrangement. This discrepancy highlights potential limitations of *ex-situ* AFM imaging in capturing true interfacial behaviour, which can be mitigated by using hydrophobic substrates.

By investigating the interplay between interfacial tensions and monolayer microstructure at liquid interface, this study provides a deeper understanding of microgel assembly at liquid interfaces. The findings offer valuable insights for designing and optimizing microgel-based materials with tunable interfacial properties, highlighting the limitations of AFM in capturing true interfacial structures and emphasize the importance of considering both intrinsic microgel properties and external conditions when analyzing interfacial organization.

Zusammenfassung

Kern-Schale-Mikrogele mit starren Kernen und weichen, deformierbaren Hydrogel-Schalen können sich an Luft/Wasser-Grenzflächen zu 2D-Mikrostrukturen anordnen. Das Verständnis ihres Grenzflächenverhaltens ist entscheidend für die Kontrolle der Monoschichtstrukturen und die Optimierung ihrer weiteren Anwendungen. Zwei zentrale Aspekte dieses Verhaltens bleiben jedoch ungeklärt: der Einfluss der Grenzflächenspannung auf die Monoschichtentwicklung sowie die Genauigkeit der Rasterkraftmikroskopie (AFM) bei der Darstellung realer Grenzflächenmikrostrukturen. In dieser Studie untersuchen wir diese Aspekte systematisch durch experimentelle und theoretische Ansätze und liefern Erkenntnisse sowohl über makroskopische als auch mikroskopische Grenzflächenverhalten.

Die starke Adsorption von Kern-Schale-Mikrogelen an Luft/Wasser-Grenzflächen steht in Zusammenhang mit der Reduktion der Grenzflächenspannung, die auch eine laterale Deformation der Mikrogele verursacht. Der Grad dieser Deformation wird typischerweise durch den angelegten Oberflächendruck gesteuert. Das Ungleichgewicht der Grenzflächenspannung zwischen mikrogelbedeckten und mikrogel-freien Bereichen ist ein entscheidender Faktor für die Entwicklung der Monoschicht. Durch die Zugabe von SDS oder linearer PNIPAM zur Anpassung der Spannung in mikrogel-freien Regionen expandieren, komprimieren oder stabilisieren sich frei schwimmende Monoschichten in Abhängigkeit vom resultierenden Spannungsungleichgewicht, das einen Marangoni-Fluss induzieren kann. Die globale Entwicklung der Monoschicht wurde verfolgt, während lokale strukturelle Veränderungen mittels AFM analysiert wurden. Der Vergleich von Kern-Schale-Mikrogelen mit identischen Silicakernen, jedoch unterschiedlicher Vernetzungsdichte, zeigt, wie die Deformierbarkeit das Grenzflächenverhalten beeinflusst. Diese Erkenntnisse liefern wertvolle Ansätze zur Steuerung von 2D-Mikrostrukturen ohne die Notwendigkeit einer Langmuir-Trog-Methode.

Darüber hinaus behandelt die Studie Diskrepanzen zwischen AFM-Bildgebung und der tatsächlichen Grenzflächenanordnung von Mikrogelen. Obwohl AFM häufig für ex-situ-Analysen verwendet wird, bleibt unklar, ob es in-situ-Strukturen korrekt wiedergibt. Bei hoher Kompression suggerieren AFM-Aufnahmen feste-feste

Phasenübergänge, die sich durch abrupte Verringerungen der interpartikulären Abstände auszeichnen. Simulationen hingegen prognostizieren eine kontinuierliche hexagonale Anordnung, was darauf hinweist, dass diese Übergänge Artefakte sind, die während des Transfers und der Trocknung der Monoschicht entstehen. Zudem beeinflusst die Substrathyrophobie die endgültige, durch AFM beobachtete Struktur: Hydrophile Substrate begünstigen Clusterbildung und Hohlraumbildung, während hydrophobe Substrate die native Monoschichtanordnung besser bewahren. Diese Diskrepanz unterstreicht die potenziellen Einschränkungen der ex-situ-AFM-Bildgebung zur Erfassung des tatsächlichen Grenzflächenverhaltens, die durch die Verwendung hydrophober Substrate verringert werden können.

Durch die Untersuchung des Zusammenspiels zwischen Grenzflächenspannungen und Monoschichtmikrostruktur an Flüssigkeitsgrenzflächen bietet diese Studie ein tieferes Verständnis der Mikrogelassemblierung an flüssigen Grenzflächen. Die Ergebnisse liefern wertvolle Erkenntnisse für die Gestaltung und Optimierung mikrogelbasierter Materialien mit einstellbaren Grenzflächeneigenschaften, verdeutlichen die Grenzen der AFM zur Erfassung realer Grenzflächenstrukturen und betonen die Bedeutung der Berücksichtigung sowohl intrinsischer Mikrogeleigenschaften als auch äußerer Bedingungen bei der Analyse der Grenzflächenorganisation.

1. Introduction

Microgels have garnered significant interest in recent years for their fascinating properties and wide-ranging applications in science and technology[1-4]. Compared to rigid particles, soft, porous microgels are highly deformable, allowing them to conform to various environments, such as interfaces or confined spaces, providing enhanced surface coverage and utility in coatings and surface patterning[5-7]. Soft microgels are also often responsive to environmental stimuli—such as pH[8], temperature[9, 10], or ionic strength[11, 12]—enabling reversible changes in size or charge, which are beneficial for controlled drug release[13], biosensing[14], and optical devices[15]. Additionally, soft microgels exhibit favourable interfacial behaviour, forming stable, well-ordered arrays that are ideal for surface patterning[16], structural colour[17], and plasmonics[18-20].

Among the microgels, those composed of PNIPAM microgels are well-known due to their ease of synthesis and thermo-responsive properties[21-24]. Monodispersed micrometre-size PNIPAM microgels can be prepared through free radical precipitation polymerization of the monomer N-isopropylacrylamide (NIPAM) and N, N'-methylenebisacrylamide (BIS) as a cross-linker[25-27]. PNIPAM microgels undergo a volume phase transition (VPT) in water from a swollen state to a collapsed state at around 32 °C[28, 29]. Furthermore, PNIPAM microgels can be easily modified and functionalized with other molecules or embedded with inorganic cores, making them suitable for creating core-shell particles with specific properties (**Figure 1. 1f**) [30-34]. Such core-shell microgels exhibit the combined properties of a hard core and a soft shell, enabling them to assemble into complex patterns at solid and fluid interfaces with tunable inter-particle distances[35-40].

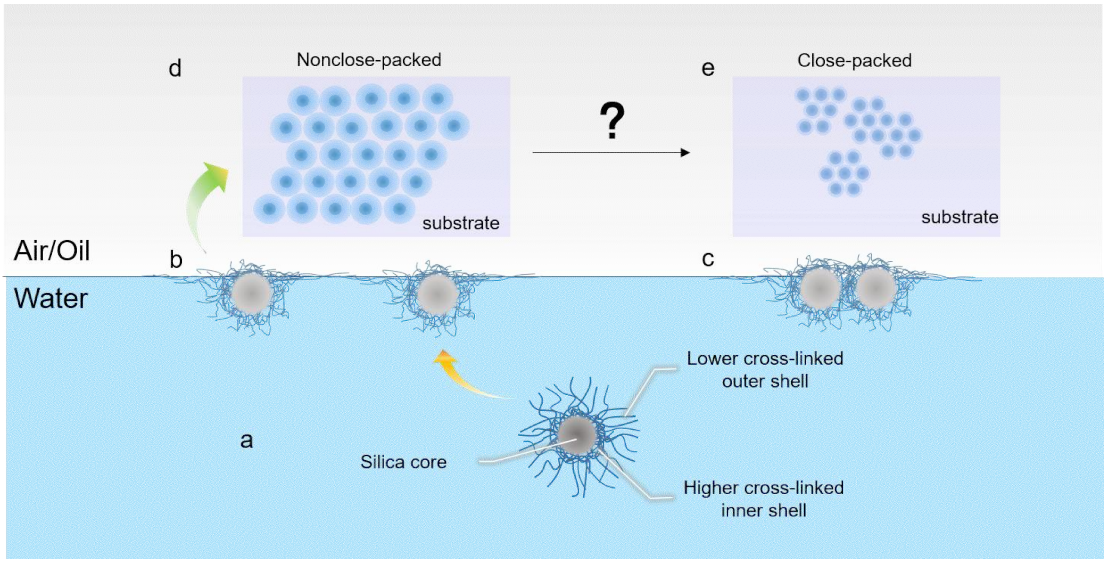

Figure 1. 1. Schematic description of SiO_2-PNIPAM microgels in the bulk phase and at fluid interfaces. Each microgel consists of a rigid silica core and a soft PNIPAM shell, which includes a highly cross-linked inner layer and a less cross-linked outer layer. (a). A swollen microgel dispersed in the bulk aqueous phase. (b, c). Microgels adsorbed at air/water or oil/water interfaces, forming hexagonal lattices with larger interparticle distances under low compression (b) and smaller interparticle distances under high compression (c). (d, e). Microgels at different compression states can be transferred to a solid substrate. The transferred monolayer shows a non-close-packed (shell-shell contact) arrangement (d) or close-packed (core-core contact) hexagonal clusters with voids in between (e).

The internal structure of microgels has already been studied by small-angle neutron scattering (SANS) and nuclear magnetic resonance (NMR) approaches, revealing that the microgels present a “core-shell” structure due to the density gradient from the centre to the periphery[41, 42]. These microgels consist of three structural regions (**Figure 1. 1a**): a dense, highly cross-linked “core” in the central region, a loosely cross-linked “shell” surrounding the core, and, at the outer edge, a corona made up of even more loosely cross-linked PNIPAM chains[43, 44]. The morphology of the microgel is governed by the reactivity differences between the monomer and cross-linker. During batch synthesis, cross-linkers react faster than monomers, leading to a gradient in cross-link density from the centre toward the periphery of the microgel[45]. By adjusting the relative concentrations of monomer and cross-linker or controlling the rate

of monomer addition, the thickness and density of the “core” and “shell” regions can be tuned[46, 47]. Correspondingly, a continuous monomer feeding approach can promote a more homogeneous cross-linker distribution[48, 49]. In this work, uranyl acetate staining combined with transmission electronic microscopy (TEM) imaging is employed as an effective method to visualize the “core” and “shell” regions, offering an intuitive way to compare the structural variations of microgels with different cross-linking densities.

Microgels’ soft, deformable nature enables them to adapt to interfacial forces, spreading and flattening at oil/water or air/water interfaces in response to surface tension and capillary forces[50, 51]. This adaptable structure typically results in a "fried-egg" morphology, where microgels exhibit a larger radius than in bulk solution (**Figure 1. 1b, c**), as observed using cryo-scanning electron microscopy (cryo-SEM)[7, 52-55]. The flattening of microgels is especially pronounced in those with lower cross-linking densities, i.e. large softness[56], and hollow microgels with an internal cavity[57, 58]. At interparticle contacts, this leads to significantly larger interparticle distances compared to the bulk diameter of the microgels measured in dispersion[59, 60]. These microgels assemble into hexagonal lattices with adjustable inter-particle distances at liquid interfaces, forming structured 2D monolayers[61-66]. One of the common methods to fabricate the 2D structured monolayer is fluid interface-assisted (self-)assembly, which offers low processing costs, fast speed, and repeatability while enabling the formation of macroscopic assemblies with wafer-scale or even larger dimensions[7, 67, 68]. The fluid interface allows further manipulation of the obtained assemblies by, for example, acoustic modulation[69, 70] or alterations in the accessible surface area as it is typically achieved in a classical Langmuir trough[71, 72]. Monolayers of soft and deformable microgels confined at fluid interfaces can be compressed to a certain

degree, depending on the softness and shell-to-core size ratio. Large shell-to-core ratios are achievable with precipitation and cross-linking of polymeric shells onto cores[10, 73-75]. The resulting properties of the core-shell microgels are characterised by the properties of both the cores and the shells[76].

The assembly at fluid interfaces is driven by a balance of attractive capillary forces, van der Waals interactions, and short-range electrostatic or steric repulsions[68, 77-79]. This behaviour can be used to prepare freely floating monolayers of hexagonally packed microgels[19, 80]. A direct assembly method can form ordered 2D arrays by floating microgels at interfaces, with surfactants like SDS acting as a soft barrier to stabilize the formation of hexagonal arrays, and the assembly can be controlled by varying SDS concentrations[81-86]. Interfacial tension imbalance at the available surface area will further influence the monolayer behaviour due to Marangoni flow[87]. Compared to rigid spheres in the close-packed state, microgels can be compressed over a broad range of surface pressures at fluid interfaces. Therefore, imbalances in interfacial tension and the resulting Marangoni flow are expected to have a significant impact on the monolayer evolution of soft microgels. Understanding the interplay between interfacial tension, microgel structure, and the self-assembly process will offer valuable insights into the intricate dynamics governing interfacial assemblies.

The microgel monolayer at a distinct compression state (surface pressure) can be transferred to a solid substrate for *ex-situ* microscopy analysis using techniques such as atomic force microscopy (**Figure 1. 1d, e**)[37, 88, 89]. After transfer and drying on solid substrates, the 2D structure of the monolayer can be imaged using AFM or scanning electron microscopy (SEM). At low surface pressure, the monolayers form non-close-packed hexagonal lattices, where the particles are in shell-shell contact

(**Figure 1.1d**). As the surface pressure increases, the monolayers transition to close-packed hexagonal lattices with voids in between, characterized by core–core contact between particles (**Figure 1.1e**). This discontinuous transition, known as the "isostructural phase transition", is ascribed to the combination of attractive capillary forces and local failures of the polymer shells of the microgel monolayer at the fluid interface [90, 91]. However, whether *ex-situ* AFM observations can adequately elucidate the assembly and structure of microgel monolayers at fluid interfaces remains a question. In 2021, Hoppe Lavarez *et al.* pointed out that the conformation of the microgels after the deposition strongly depended on the hydrophilicity of the surface, which controls the adsorption strength[92]. Their finding revealed that the shape and degree of spreading of soft microgels at interfaces are influenced not only by their intrinsic properties and the characteristics of the substrate but also by the deposition methodology. Moreover, Keumkyung Kuk *et al.* compared the structural order of the microgel monolayers *in-situ* at the interface during compression and *ex-situ* after transfer to solid substrates. They found that "isostructural phase transition" did not occur at the air/water interface[59]. The authors suggested that the deposition method and the substrate govern the colloidal monolayers' microstructural phase transitions. Despite these advancements, critical challenges persist. When and where the structure transition occurred is still an open question and needs further investigation. Furthermore, the impact of internal microgel structures, such as cross-linking density and core-shell morphology, on their interfacial behaviour remains inadequately understood. This work addresses these questions by systematically exploring the relationships between microgel structure, interfacial behaviour, and deposition outcomes through a combination of experimental and simulation approaches.

For this study, silica-core/PNIPAM-shell particles with varying cross-link densities were synthesized, and their assembly behaviour at interfaces was systematically investigated. The first part of the work explores the effect of external interfacial tension on the time-dependent evolution of freely floating monolayers of core-shell microgels. By varying interfacial tension with SDS and using microgels of different cross-linker densities, the role of softness in monolayer expansion driven by Marangoni flow was investigated. This study provides key insights into the phase behaviour of soft colloids at fluid interfaces, emphasizing the role of interfacial tension imbalance, and offers practical approaches for tuning monolayer structures and interparticle distances using accessible and cost-effective methods. In the second part of the work, the study focuses on the influence of substrate type and microgel softness on the results from *ex-situ* AFM analysis coupled with Langmuir compression experiments. DPD simulations provided *in-situ* insights into the structural evolution of microgel monolayers under compression. The findings suggest that discrepancies between *in-situ* and *ex-situ* observations, including the "isotropic phase transition", may stem from drying-induced structural rearrangements. This research offers valuable insights into the effects of substrate hydrophilicity and microgel shell architecture on the resulting structures.

2. Theoretical Background

This section provides an overview of the synthesis of silica-core/PNIPAM-shell microgels, including a discussion of the mechanism of seeded precipitation polymerization and the resulting cross-link distribution during shell synthesis. Moreover, we discuss the behaviour of these microgels in bulk and at the air/water interface, highlighting their volume phase transition in response to temperature, shell deformation, self-assembly at the air/water interface, and interactions with glass substrates. Lastly, it presents various characterization methods employed to study these microgels.

2.1 Thermoresponsive microgels

This section presents the synthesis process and structural characteristics of SiO_2-PNIPAM microgels. The seeded precipitation polymerization of SiO_2-PNIPAM microgels initiates with the silica core prepared through the Stöber method, followed by the encapsulation of these cores in PNIPAM shells. Due to the faster reactivity of the cross-linker compared to the monomer, an inhomogeneous cross-link density gradient is formed within the shell, as described by Stieger *et al.* in the SANS experiments[46]. This gradient in cross-link density impacts the microgel's swelling behaviour and mechanical properties. The thermoresponsive behaviour, including the volume phase transition and swelling capacity in response to temperature changes, can be analysed using dynamic light scattering (DLS).

2.1.1 Core-shell microgels

Seeded precipitation polymerization is a versatile method for synthesizing core-shell microgels, where a solid seed (e.g., silica particles) serves as the core, and a polymer shell is formed around it via free radical polymerization[76]. The resulting shells can

be tuned in thickness, ranging from tens to hundreds of nanometers. In the case of SiO_2-PNIPAM microgels, the silica core acts as a seed, while the PNIPAM shell forms through the polymerization of N-isopropylacrylamide (NIPAM) monomers in the presence of the cross-linker N,N'-methylenebisacrylamide (BIS). The silica cores are prepared using the Stöber method, which produces monodispersed silica particles through the hydrolysis and condensation of tetraethyl orthosilicate (TEOS) in an alcohol-water mixture, catalyzed by ammonia[93-95]. The reaction between the surface silanols and trimethoxysilane-based organics could modify the surface of the silica particle. Functional groups such as aminopropyl, octadecyl and mercaptopropyl groups could then be modified to the particle surface[96]. In this work, methacryloxypropyltrimethoxysilane (MPS)-modified silica particles with diameters around 100 nm were synthesized and subsequently used as cores for core-shell microgels.

The shell part of the core-shell microgel is constructed through the free radical polymerization of NIPAM monomers (see **Figure 2. 1**). The reaction temperature is set to be around 70 °C. On the one hand, the initiator potassium peroxodisulfate (PPS) decomposes into free radicals at this temperature[97]. The free radicals from the initiator attack the NIPAM and BIS monomers, forming oligomer radicals (short polymer chains). These oligomer radicals then grow into longer polymer chains, forming polymer radicals. On the other hand, due to PNIPAM's Lower Critical Solution Temperature (LCST) of around 32 °C, PNIPAM experiences poor solvent conditions at 70 °C, favouring the formation of microgels over macrogels[98]. As a result, the polymer shell continues to grow around the inorganic cores until all the monomers are consumed, which forms a core-shell structure with an inorganic core at the centre and a surrounding PNIPAM layer. The polymer shell stabilizes the nanoparticles by preventing aggregation through steric and electrical repulsions, in which the charges

come from the initiator. Additionally, it serves as a spacer in two-dimensional arrays, maintaining proper distance between particles. This process is adaptable and flexible, enabling precisely tuning of shell thickness through a semi-batch process and modification of properties by incorporating various comonomers into the polymer network, such as BIS as a cross-linker or acrylic acid to introduce functional groups[99-104]. During the one-batch seeded precipitation polymerization, the cross-linker's faster reactivity compared to the NIPAM monomer leads to a falling cross-link density gradient from the central to the periphery of the shell[43, 105]. Such inhomogeneity in cross-link density is a characteristic feature of the microgel's structure and plays a crucial role in determining its mechanical properties and swelling behaviour. The internal shell structure can be analyzed using techniques such as SANS and DLS.

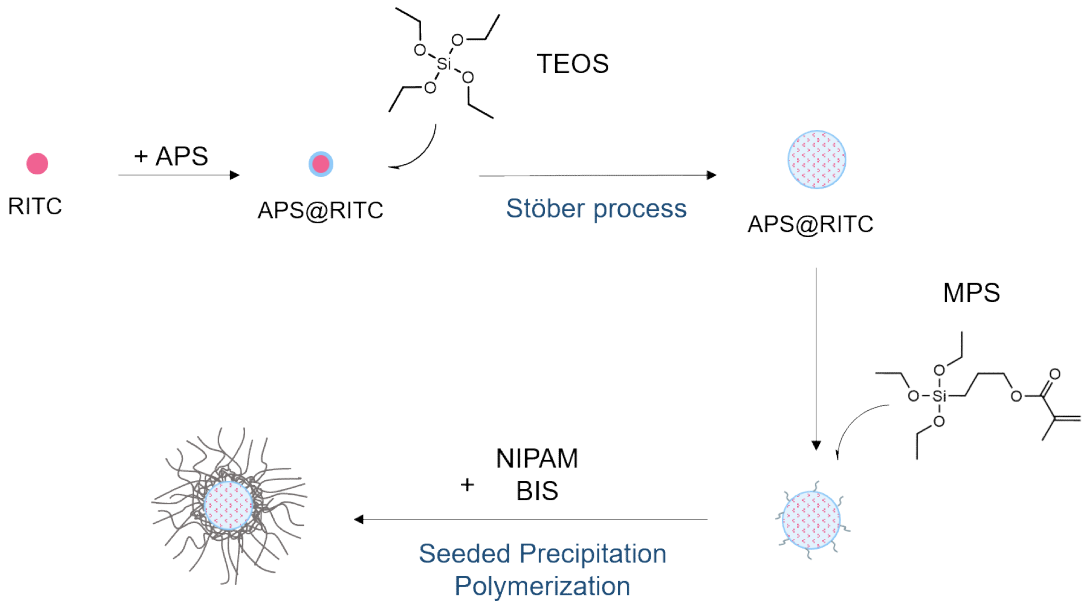

Figure 2. 1. Schematic illustration of the synthesis of core-shell microgels. The process begins with the preparation of an RITC-labeled silica core via the Stöber process. The silica core is then surface-modified with MPS to introduce reactive methacrylate groups. In the next step, seeded precipitation polymerization is carried out using NIPAM as the monomer and BIS as the cross-linker, forming a PNIPAM shell around the silica core. The resulting core-shell microgels consist of a rigid silica core and a soft PNIPAM hydrogel shell.

In 2010, Karg *et al.* prepared well-defined thermoresponsive SiO_2-PNIPAM microgels, starting with MPS-functionalized silica cores (70–170 nm) and resulting in core-shell microgels with diameters of 181–268 nm at 15 °C[38]. Here, MPS is thought to provide the silica surfaces with terminal double bonds, facilitating the association between the silica cores and the PNIPAM shells[106]. In 2016, Rauh *et al.* further investigated how nanoparticle surface functionalization and concentration affect core-shell microgel formation[107]. Using spherical gold nanoparticles as seeds in the radical polymerization of NIPAM, they successfully synthesized core-shell microgels with single gold cores, and the hydrogel shell thickness could be precisely controlled. They observed that encapsulation occurs through the precipitation of oligomers/polymers onto the seed surface, regardless of polymerizable groups.

Volume phase transition behaviour. PNIPAM is a thermoresponsive polymer that undergoes a coil-to-globule transition in water around 32 °C[108]. This reversible behaviour is particularly useful in applications such as drug delivery[109], nanoparticle assembly[35, 110] and microfluidics[111]. Below the volume phase transition temperature (VPTT), PNIPAM microgels are hydrated and swollen due to strong polymer-solvent interactions, where the amide groups form hydrogen bonds with water. Above the VPTT, polymer-polymer interactions are favoured, the hydrophobic interactions between the isopropyl groups of PNIPAM become stronger than the interactions with water, PNIPAM becomes hydrophobic. Therefore, microgels shrink into a compact, less hydrated structure[112]. The swelling and deswelling behaviour can be quantified using the swelling ratio (β) and the deswelling ratio (α), as described below:

$$\alpha = \frac{V_h(T)}{V_{h,swollen}} \quad (2.\ 1)$$

$$\beta = \frac{V_h(T)}{V_{h,collapsed}} \quad (2.\ 2)$$

Here, $V_h(T)$ corresponds to the hydrodynamic volume of the microgels at temperature T, $V_{h,swollen}$ and $V_{h,collapsed}$ correspond to the hydrodynamic volume of the microgels at the fully swollen and collapsed state. The VPT of PNIPAM microgels can be influenced by several factors, such as cross-linker density, the choice of comonomer[113], the type of cross-link agent, etc. The volumes of PNIPAM microgels are typically calculated based on the hydrodynamic radii obtained from DLS measurements, which we will explain in detail in this section.

Swelling-deswelling behaviours of microgels. The thermodynamics of the swelling-deswelling behaviour is commonly characterized using the Flory-Rehner theory[114, 115]. By applying the Flory-Rehner model to R_h vs. T data, the key parameters, including polymer-solvent interaction strength and the degree of cross-linking in the network, can be quantitatively determined[116-118]. This theory combines the Flory-Huggins solution theory, providing a comprehensive framework for understanding how polymer networks swell by balancing the osmotic pressure contributions from mixing (due to polymer-solvent interactions) and elastic forces (due to network deformation)[119]. Osmotic pressure promotes swelling by favouring polymer-solvent mixing, while elastic pressure opposes it due to the stretching of chains between cross-links. The elastic osmotic pressure Π_e is calculated as below:

$$\Pi_e = \frac{N_c k_B T}{v_0}\left[\frac{\phi}{2\phi_0} - \left(\frac{\phi}{\phi_0}\right)^{1/3}\right] \quad (2.\ 3)$$

Here N_c is the number of chains in the network, k_B is Boltzmann constant, ϕ is polymer volume fraction, which can be obtained from DLS measurements, v_0 and ϕ_0 are microgel volume and related volume fraction in the reference state. The mixing osmotic pressure Π_{mix} is given by[116]:

$$\Pi_{mix} = -\frac{N_A k_B T}{v_s}[\phi + \ln(1-\phi) + \chi\phi^2] \quad (2.\ 4)$$

Here, N_A is Avogadro's number, v_s is the molar volume of the solvent, χ is the Flory-Huggins solubility parameter. χ can be calculated as:

$$\chi = \frac{1}{2} - A\left(1 - \frac{\theta}{T}\right) + C\phi + D\phi^2 \quad (2.\ 5)$$

$$A = -\frac{\Delta S}{2k_B} + \frac{1}{2} \quad (2.\ 6)$$

$$\theta = \frac{2\Delta H}{2\Delta S + k_B} \quad (2.\ 7)$$

Here θ is the theta temperature, ΔS is the non-combinatorial entropy change, which refers to the entropy difference associated with transferring a polymer segment from a bulk polymer (where it interacts primarily with other polymer segments) to a solvent (where it interacts with solvent molecules). ΔH is the equivalent enthalpic contribution. C and D are empirical constants relating to volume fraction. The interplay of these pressures determines the polymer's equilibrium size in the swollen state[120]. The net osmotic pressure inside the microgel is zero at equilibrium. The Flory-Rehner theory provides the changes of the polymer network's volume or size in response to environmental factors such as temperature. For thermoresponsive microgels like PNIPAM, these size changes can be directly linked to the swelling ratio ($\beta = \frac{\phi}{\phi_0}$). DLS is an ideal experimental technique to measure these size changes, as it provides precise hydrodynamic radius measurements across varying conditions, such as temperature or solvent quality.

Understanding the internal structure of microgels is crucial for linking their swelling behaviours and interfacial properties to their performance in various applications. In 1986, Pelton *et al.* mentioned the gradually increasing polymer density from the outer edge to the central part in PNIPAM microgels[25]. Then, in 1994, Wu *et al.* first examined the kinetics of PNIPAM microgel formation, discovering that the cross-linker (BIS) is consumed faster than the monomer (NIPAM) during emulsion copolymerization[43]. By measuring conversion rates over time, they systematically analyzed how factors such as NIPAM, BIS, SDS, and temperature impact the synthesis process. This work was instrumental in identifying the inhomogeneous spatial distribution of cross-link density within PNIPAM microgels. Following this, in 2000, Guillermo *et al.* employed nuclear magnetic resonance (NMR) to investigate the structure further, distinguishing different structural regions by observing variations in proton mobility through magnetic relaxation rates[41]. Their work proposed a "core-shell" morphology for PNIPAM microgels, highlighting distinct core and shell regions with differing polymer density. Based on these studies, people recognized that a swollen PNIPAM microgel has a significantly different internal structure compared to a homogeneous sphere due to this density gradient. Such inhomogeneous structures were further characterized by scattering techniques such as SANS, Small-Angle X-ray Scattering (SAXS), and DLS, which will be discussed in the following sections [42, 44, 46, 121].

2.1.2 Small-angle scattering (SAS)

SANS and SAXS are a powerful techniques for probing the size, shape and internal structure of microgels on the nanoscale[122]. In this thesis, SAXS was used to characterize the silica cores, and previous SANS measurements of PNIPAM microgels provide information of density fluctuations within the polymer networks[123, 124].

SAS experiments are typically conducted at small scattering angles because the scattering is most sensitive to larger particles at low angles. In a SAXS experiment, the sample is irradiated with X-rays and the scattered intensity I is recorded as a function of the scattering vector q, which is related to the scattering angle and X-ray wavelength. The data is collected using a 2D detector and then azimuthally averaged to obtain the 1D $I(q)$ curve. The scattering intensity $I(q)$ is measured as a function of the momentum transfer q. The intensity of the radiation (X-rays or neutrons) is measured as a function of the scattering angle, θ.

$$q = |\vec{q}| = \frac{4\pi}{\lambda} sin\frac{\theta}{2} \quad (2.\ 8)$$

Where $\vec{q}$ is the scattering vector, a vector quantity that describes the difference between the wave vectors of the incident wave and the scattered wave. Its magnitude, q, is known as the momentum transfer. θ is the scattering angle, and λ is the wavelength of the radiation. The momentum transfer q is inversely proportional to the characteristic length scale d, given by the relationship $d \approx 2\pi/q$. This inverse relationship makes q a critical parameter for interpreting the spatial distribution and size of features in scattering experiments. The shape of $I(q)$ provides information about the size and internal structure of the microgel. The scattering intensity $I(q)$ of an individual nanoparticle is related to the form factor $P(q)$, which describes the internal structure of individual particles, and structure factor $S(q)$, which accounts for inter-particle interactions.

$$I(q) = n\rho^2 V^2 P(q) S(q) \quad (2.\ 9)$$

Here, n is the number density of the particles, ρ is the electron density of the particle, and V is the volume of the particle. For dilute solutions of microgels, $S(q) \approx 1$. For

SANS measurements, $I(q)$ depends on the contrast in scattering length density (SLD) between the microgel and the solvent. In 2004, Stieger *et al.* introduced a direct modelling approach to analyse the scattering intensity distribution of PNIPAM microgels. In this method, they define the scattering cross-section ($d\sigma(q)/d\Omega$), which is independent of the transmission and the form of the sample, to represent $I(q)$. For a monodisperse suspension of spherical particles, according to equation 2. 2, the differential scattering cross section is given as below:

$$I(q) = \frac{d\sigma(q)}{d\Omega} = n\Delta\rho_{SLD}^2 V_{ploy}^2 P(q)S(q) \quad (2.\ 10)$$

Where n is the number density of the particles, V_{poly} is the volume of polymer in a particle, $P(q)$ is the normalized form factor, and $S(q)$ is the interference of scattering from different particles. It is important to note that ρ in equation (2. 2) represents the electron density of the particle, while in SANS SLD is used to describe how strongly a material scatters neutrons, and it varies for different isotopes of the same element. $\Delta\rho_{\mathrm{SLD}}$ is the difference in SLD between the polymer and solvent, given by $\Delta\rho_{SLD} = \rho_{polymer} - \rho_{solvent}$. The SLD of the particle or the solvent is calculated as below:

$$\rho_{SLD} = \frac{\rho_{app}}{M_w} N_A \sum_{i=1}^{m} b_i \quad (2.\ 11)$$

Here, ρ_{app} is the apparent specific density, defined as the ratio of the material's mass to its apparent volume, which includes both the polymer network and the porous within. M_w is the molecular weight, N_A is Avogardo's number, and b_i is a nucleus's bound coherent scattering length.

In SANS, the form factor describes the scattering contribution of an individual particle. For monodispersed homogeneous spherical particles, the distribution of scattering length density within the particle is uniform. Therefore, $P_{\mathrm{hom}}(q)$ depends on the size and shape of the particle, which can be described by a radial box function:

$$P_{hom}(q) = \left[3 \cdot \frac{\sin(qR) - qR \cdot \cos(qR)}{(qR)^3}\right]^2 \quad (2.\ 12)$$

Where R is the radius of the particles. The box function models a sharp boundary between the particle and its surrounding medium. However, microgels typically have a fuzzy surface due to the polymer network structure and inhomogeneous cross-linking density distribution[42, 125]. To account for the fuzziness in the model, Stieger *et al.* convoluted the radial box profile with a Gaussian[126]. The form factor then can be expressed as:

$$P_{inho}(q) = \left[3 \cdot \frac{\sin(qR) - qR \cdot \cos(qR)}{(qR)^3} \times exp\left(-\frac{(\sigma_{surf} q)^2}{2}\right)\right]^2 \quad (2.\ 13)$$

Where σ_{surf} is the width of the smeared particle surface, the smeared surface describes the gradual transition from the compact core to the more expanded and less densely cross-linked surface. **Figure 2. 2** shows the SANS scattering profile of the PNIPAM microgel. In the central region of the microgel is a highly cross-linked "core" characterized by a radial box profile. Within this core region, the cross-linking density is relatively uniform and remains constant up to a specific radius, denoted as $R_{\mathrm{box}} = R - 2\sigma_{surf}$, where σ_{surf} represents the width of the smeared particle surface. Beyond the core region, the cross-linking density starts to decrease gradually. The decrease in cross-linking density is described by σ_{surf}, and the profile decreases to half the core density at R. The overall size of the microgel determined from the SANS data is ap-

proximately given by $R_{SANS} = R + 2\sigma_{surf}$. At this effective radius R_{SANS}, the scattering profile approaches zero, indicating the outer boundary of the microgel. The size obtained from SANS, R_{SANS}, is typically slightly smaller than the hydrodynamic radius measured by DLS. This discrepancy occurs because SANS measures the size of the dense core and the immediately surrounding structure, while DLS includes contributions from the entire hydrated shell, including any extended polymer chains. In the case of hybrid particles with silica cores and PNIPAM shells, TEM and AFM images show a single silica core centrally positioned within the microgels, which display swelling behaviours similar to pure PNIPAM microgels[34, 127].

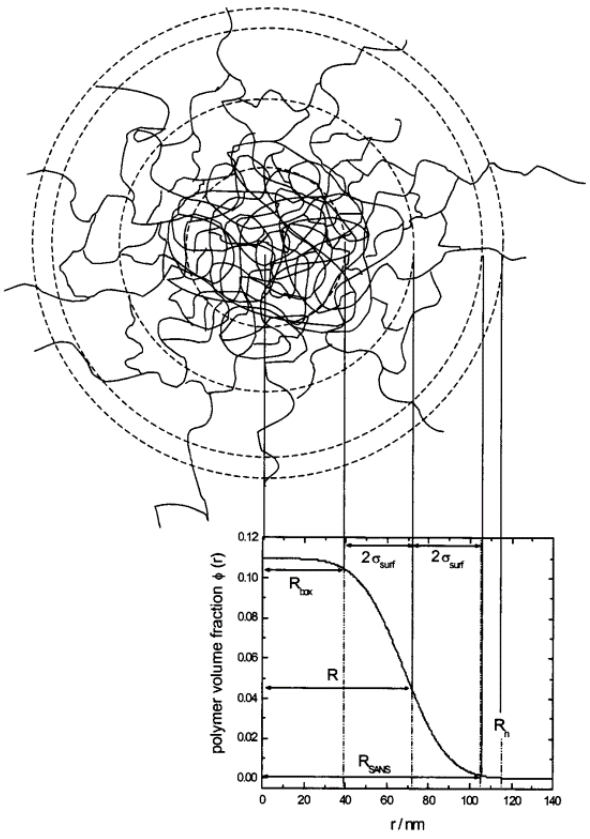

Figure 2. 2. Schematic illustration of a PNIPAM microgel. The central region of the microgel consists of a highly cross-linked "core", which is modelled using a radial box profile. The radius of the "core" is denoted as R_{box}. The cross-linking density gradually decreases from the centre towards the periphery. The outer, fuzzy region of the microgel is characterized by a surface thickness σ_{surf}. The overall size of the microgel is represented by R_{SANS}, which is slightly smaller than the hydrodynamic radius R_h obtained from DLS. Adapted from ref. [46].

2.1.3 Dynamic Light Scattering (DLS)

DLS is a widely used technique for measuring the hydrodynamic radius (R_h) and monodispersity of nanoparticle and macromolecule suspensions. It measures fluctuations in scattered light intensity caused by the Brownian motion of particles in a liquid[128]. These fluctuations reveal particle diffusion, which is linked to their hydrodynamic size via the Stokes-Einstein equation.

A DLS instrument's components are shown in **Figure 2. 3**. A monochromatic laser beam passes through a suspension contained in a cuvette, interacting with particles undergoing random motion, known as Brownian motion. The speed of this motion depends on particle size, temperature, and solvent viscosity. When photons interact with a suspension, they induce oscillations in the electron cloud of the particles, creating dipoles that radiate scattered light in all directions[129]. A detector captures this scattered light at a specific angle. If the particles were stationary, the scattering intensity would remain constant. However, due to Brownian motion, the intensity fluctuates over time[130]. These fluctuations are analyzed to calculate an autocorrelation function, which measures the similarity between the intensity at a given time and at a later time. The rate at which the autocorrelation function decays reflects the speed of Brownian motion: smaller particles cause a faster decay, while larger particles result in a slower decay. This relationship allows DLS to determine the particle size distribution in the suspension.

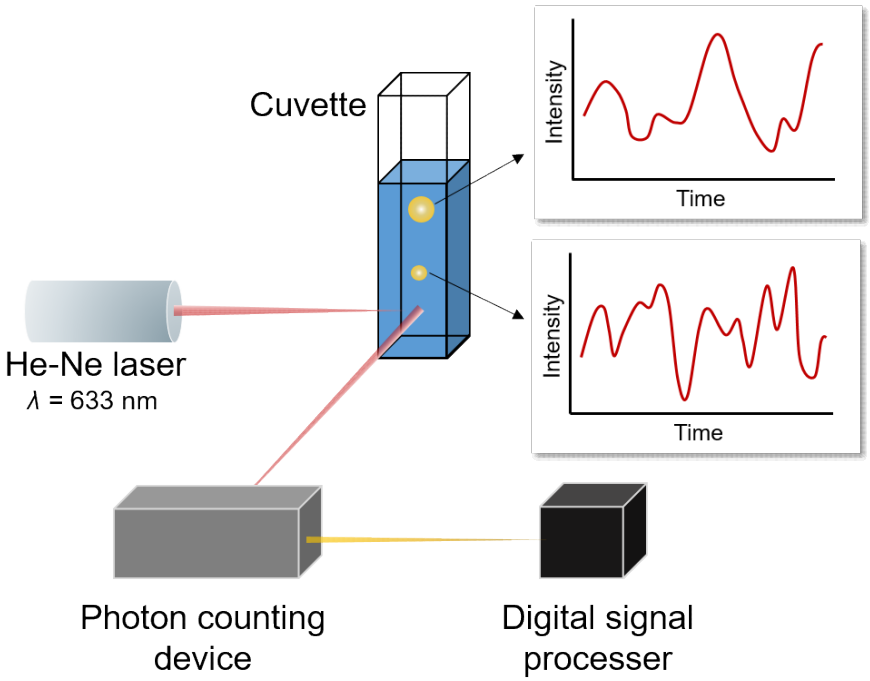

Figure 2. 3. Schematic diagram of the components of a dynamic light scattering instrument and the hypothetical dynamic light scattering of large and small particles. The laser beam used in this work is a He-Ne laser with a wavelength of 633 nm. The photon-counting device is to measure the intensity of the scattering light. The intensity vs. time plots show fluctuations for large and small particles. Larger particles exhibit slower intensity fluctuations due to slower Brownian motion, while smaller particles show faster fluctuations.

The speed of Brownian motion is characterized by the translational diffusion coefficient D. The Stokes-Einstein equation relates D to the hydrodynamic radius R_{h} of the particles:

$$D = \frac{k_B T}{6\theta\eta R_h} \qquad (2.\ 14)$$

Here, k_B is the Boltzmann constant, T is the absolute temperature, and η is the dynamic viscosity of the medium. The calculated R_h assumes that the particles behave as hard spheres diffusing at the same speed[131]. However, microgels often feature a fuzzy or diffuse surface layer, thus R_h includes contributions from this diffuse outer

region. Additionally, for charged microgels, the surface-associated electric double layer, formed by counterions, also contributes to the measured R_h.

The intensity autocorrelation function of scattered light $g^2(\tau)$ is used to get the translational diffusion coefficient D. $g^2(\tau)$ quantifies the degree of similarity between the scattered light intensity at a given time (t) and the intensity at a time lag (τ). $g^2(\tau)$ is generated from the scattering intensity ($I(q)$) as follows:

$$g^2(\tau) = \frac{\langle I(t)I(t+\tau)\rangle}{\langle I(t)\rangle^2} \quad (2.\ 15)$$

Here, $I(t+\tau)$ is the time-averaged product of scattered intensities at time t and $t+\tau$. At short delay times, particles move only slightly from their initial positions. As the delay time increases, they move farther, leading to a decrease in correlation. In monodispersed system, $g^2(\tau)$ is related to the field autocorrelation function $g^1(\tau)$ by the Siegert relation[132]:

$$g^2(\tau) = 1 + \beta|g^1(\tau)|^2 \quad (2.\ 16)$$

Where β is a coherence factor that depends on the particle's geometry and scattering properties. For a uniform (or monodisperse) system, the first-order autocorrelation function $g^1(t)$ can be regarded as a single exponential function[133]:

$$g^1(\tau) = \exp(-\Gamma\tau) \quad (2.\ 17)$$

$$\Gamma = Dq^2 \quad (2.\ 18)$$

Here, Γ is the decay rate, D is the diffusion coefficient, and q is the magnitude of the wave vector. Furthermore, for polydisperse particles, the autocorrelation function

$g^1(t)$ is the sum of a series of the exponential decays. They represent the contribution of each size population to the overall scattering intensity:

$$g^1(\tau) = \int_0^\infty G(\Gamma) \exp(-\Gamma\tau)\, d\Gamma \qquad (2.\ 19)$$

From the average decay rate Γ, the average diffusion coefficient D and hence the hydrodynamic size R_h can be calculated. Furthermore, the particles' mean size and polydispersity index (PDI) can be determined using Cumulant analysis[134].

DLS can be effectively employed to measure the swelling ratio of PNIPAM microgels[125, 135, 136]. The measurement is conducted at different temperatures or solvent compositions, capturing the hydrodynamic diameter of the PNIPAM microgels as a function of these variables[137, 138]. DLS measurements at various temperatures yield hydrodynamic diameter data corresponding to the microgel's different states. By comparing the hydrodynamic diameters before and after the VPTT, the swelling ratio (α), can be calculated by equation (2. 7).

2.2 Interfacial behaviour and assembly of microgels at fluid interfaces

Microgels exhibit unique interfacial behaviours due to their deformability and responsiveness to environmental conditions. Unlike traditional hard-sphere particles, microgels exhibit softness, deformability, and environmental responsiveness, which allow them to transition between different states depending on external stimuli. These unique properties make the interactions between particles more complex, influencing their phase behaviour, rheological properties, and ability to self-assemble. In this section, the hard-sphere model will first be discussed to understand basic colloidal inter-

actions, followed by exploring how microgels behave differently due to their deformability.

2.2.1 Forces acting on colloidal particles in suspensions

Before delving into the behaviour of microgels at fluid interfaces, it is essential to understand the fundamental forces acting on colloidal particles in bulk suspensions. The stability of colloidal particles is typically described by the DLVO theory (Derjaguin-Landau-Verwey-Overbeek theory), which combines van der Waals attractive forces and electrostatic repulsive forces[139, 140]. It considers two main components: (1) Repulsive forces between two or more particles, such as electric forces, come into play when particles carry surface charges, prevent the aggregation and flocculation of the colloidal dispersion; (2) Attractive forces, such as Van der Waals forces, arising from temporary fluctuations in electron distribution, can induce attractive interactions between particles and counteract the repulsive forces (**Figure 2. 4**). The electric double layer is formed when charged particles are dispersed in a medium, and it consists of a charged layer surrounding the particle, which can be described using the Gouy-Chapman-Stern model. The repulsive electrostatic force can be calculated using the Poisson-Boltzmann equation, which describes how the surface potential exponentially decays with distance from the surface. The Van der Waals forces and the electric repulsive forces together determine the dispersion stability and can be approximated as the sum of their contributions. The DLVO force for two spheres, F_{DLVO}, can be expressed as:

$$F_{\mathrm{DLVO}} \approx \frac{2\pi R\sigma^2 e^{-\kappa D}}{\kappa\varepsilon\varepsilon_0} - \frac{AR}{12\pi D^2} \qquad (2.\ 20)$$

$$\kappa = \sqrt{\frac{e^2}{\varepsilon\varepsilon_0 k_B T}} \qquad (2.\ 21)$$

Here, σ is the surface charge density, D is the separation distance, R is the radii of the particle, A is the Hamaker constant. κ is the inverse Debye length, e is the elementary charge, ε and ε_0 are the dielectric constant and permittivity of the suspending medium. It's important to note that the Poisson-Boltzmann equation and the electrostatic force calculation are based on several assumptions, such as the particles being small compared to the Debye length, the system being in thermal equilibrium, and the particles being uniformly charged. In more complex systems, additional factors such as surface roughness, surface heterogeneity, and ion-specific effects may need to be considered for a more accurate estimation of the electrostatic interactions.

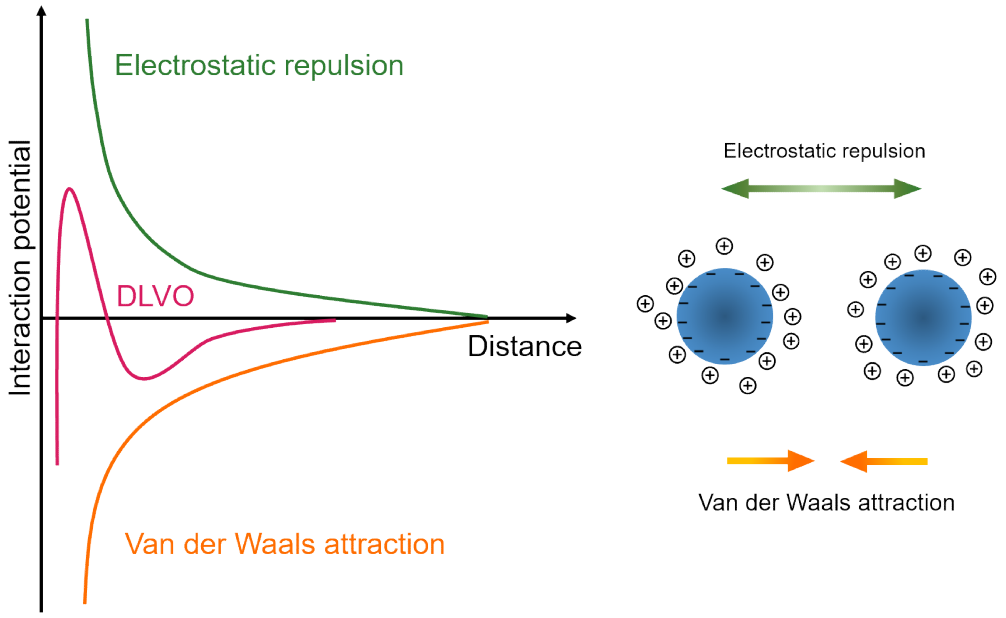

Figure 2. 4 Schematic representation of the DLVO interaction potential as a function of interparticle distance (left). The total interaction potential (magenta) results from the sum of electrostatic repulsion (green) and van der Waals attraction (orange). At short distances, van der Waals forces dominate, leading to strong attraction. At intermediate distances, an energy barrier appears due to electrostatic repulsion, which prevents particle aggregation. Beyond this barrier, the interaction potential asymptotically approaches zero. The right diagram illustrates the competition between electrostatic repulsion (green arrows) and van der Waals attraction (orange arrows) for two charged colloidal particles. Adapted from ref. [141].

While DLVO theory successfully explains the stability and aggregation of many colloidal systems, it has limitations when applied to microgels due to their soft and deformable nature. Unlike the rigid boundaries assumed in DLVO theory, microgels exhibit significant overlap and deformation, particularly at higher concentrations. Richtering *et al.* investigated PNIPAM microgels as an ideal model for exploring soft-sphere colloidal behaviour and rheological phenomena. Their findings indicate that microgels behave similarly to hard spheres at effective volume fractions below 0.494 because of the immobilized solvent within the polymer network[142]. However, microgels' inherent softness and compressibility become apparent at higher concentrations, resulting in deviations from hard-sphere behaviour[143, 144]. Consequently, the soft-sphere effective interparticle potential (u), which accounts for particle overlap, is more appropriate for modelling microgel behaviour[145]:

$$u(d_{c-c}) = \varepsilon \left(\frac{d_{nominal}}{d_{c-c}}\right)^n \quad (2.\ 22)$$

Where $d_{c\text{-}c}$ is the distance between particle centres, $d_{nominal}$ is the nominal particle diameter, n is the exponent that controls the stiffness of the potential (or the softness of the microgel particle), and ε is a scaling factor. Microgels resist compression due to their cross-linked polymer network, contributing to elastic repulsion at short distances. Core-shell microgels exhibit a combination of hard-sphere-like core interactions and soft, deformable shell interactions. The soft shell allows for overlap, while the rigid core prevents complete deformation.

The equilibrium behaviour of microgels in bulk suspensions provides a foundational understanding of their intrinsic softness and responsiveness. However, when confined to fluid interfaces, the symmetry of forces acting on microgels is fundamentally dis-

rupted. The transition from a homogeneous bulk environment to an asymmetric interfacial system introduces additional complexities, such as capillary forces and interfacial tension gradients, which dominate their assembly dynamics. This shift necessitates an examination of how microgels adapt to interfacial constraints and how their deformability mediates interactions in two-dimensional (2D) confinement.

2.2.2 Forces acting on colloidal particles at interfaces

When microgels transition from bulk suspensions to fluid interfaces, their force landscape changes dramatically. At fluid interfaces, microgels are subjected not only to van der Waals and electrostatic forces but also to interfacial tension and capillary forces. The asymmetry of these forces results in behaviours that is fundamentally different from that in bulk suspensions. The adsorption energy, interfacial deformation, and capillary-driven long-range ordering of microgels become key factors in understanding their interfacial behaviour.

The deformation of microgels at fluid interfaces is a critical aspect of their interfacial behaviour. Unlike rigid particles, microgels can deform to minimize interfacial free energy, often adopting a "fried-egg" morphology. These phenomena are not merely extensions of bulk behaviour but represent emergent properties unique to interfacial confinement. In the previous section, interactions between microgels in bulk systems were discussed. At fluid interfaces, however, the two-dimensional nature of the system and the deformable interface create unique phenomena. The stabilization efficiency of colloidal particles originates from the thermodynamics of their adsorption at a fluid interface. The energy gain upon adsorption is given by[146]:

$$E = \pi R^2 \gamma (1 \pm \cos\theta)^2 \qquad (2.\ 23)$$

Where R is the radius of the particle, γ is the interfacial tension, and θ is the contact angle at the interface. The sign of the $\cos\theta$ term depends on whether the particle is being desorbed into the oil/air phase (+) or into the water phase (−). For particles with sizes of a few tens of nanometers, this energy is on the order of $10^3 k_B T$. Due to this high energy barrier, the adsorption of colloidal particles at the interface is effectively irreversible.

When colloidal particles move from a bulk aqueous phase to a liquid-liquid interface (e.g., water-oil), their electronic interactions change due to the formation of an asymmetric double layer (**Figure 2. 5**). The portion in the polar phase (e.g., water) retains its charge due to stable surface ionization, while the part in the non-polar phase (e.g., oil) re-neutralizes its surface groups for energetic stability. This creates a charged region in the polar phase and little to no charge on the non-polar side.

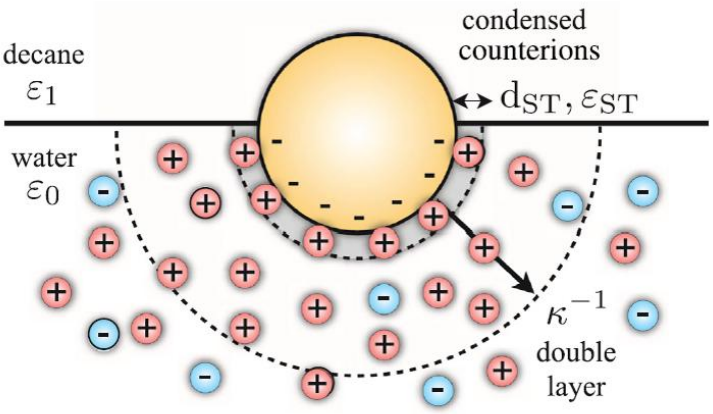

Figure 2. 5. Schematic representation of the charge distribution around a colloidal particle at the oil/water interface. The particle, adsorbed at the interface between decane (ε_1) and water (ε_0), carries a negative surface charge (black dashes). To compensate for this charge, positively charged counterions condense near the surface, forming a stern layer with thickness d_{ST} and dielectric constant ε_{ST}. Beyond this region, additional counterions and coions (negatively charged ions) are distributed in the aqueous phase, forming a diffuse electric double layer with characteristic thickness κ^{-1}. The dashed lines indicate the approximate extent of charge distribution in the water phase. Reprinted from Ref.[147].

Van der Waals interactions are more complicated to compute than in bulk phases because the particles are partially immersed in two different fluids. However, due to the complexity of calculating these interactions in such environments and the dominance of repulsive forces, their contribution is often negligible in practical systems. They become relevant only under specific conditions where particles can come into very close proximity, which is usually prevented by strong repulsions.

Capillary forces are the most significant interaction forces for particles at interfaces, driving their clustering and organization. Particles at an interface cause local deformations due to their weight, shape, or surface wettability (contact angle)[78, 148]. These deformations create gradients in the interfacial energy, leading to capillary interactions between particles. The extent and type of deformation depend on the particle's size, contact angle, and density relative to the surrounding fluids. The lateral capillary forces can be either attractive or repulsive[78, 79]. For large particles, the balance of gravitational and buoyancy forces together with the wetting properties of the particle causes deformations in the interface (**Figure 2. 6a**). This deformation results in particles attracting or repelling each other based on the curvature of the interface[149]. For smaller particles, gravitational forces are negligible, so interface deformation is not caused by particle weight. In this case, if the particle's surface is rough or chemically heterogeneous, the interface deformation arising from the contact line where the interface meets the particle becomes irregular[150]. Or from the anisotropy of the particles[151]. In the case of particles immersed in a liquid film supported by a solid substrate, the deformation of the surface is attributed to the wetting ability of the particles (**Figure 2. 6b**)[79].

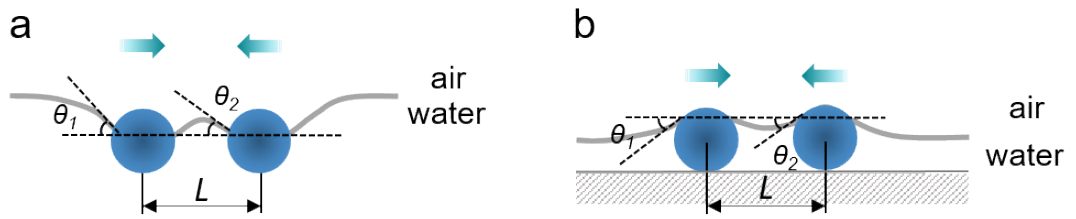

Figure 2. 6. Schematic illustration of lateral capillary forces acting on particles at a fluid interface. (a). Flotation forces: The interplay between particle weight and buoyancy induces interface deformation, leading to an attractive capillary interaction between adjacent particles. (b). Immersion forces: Due to particle wettability, the interface deforms around the particles, generating capillary interactions. The immersion depth *L* and the interparticle distance *L* influence the magnitude of the force. The arrows indicate the direction of the resulting attractive interactions.

It is worth noting that the interactions for microgels at fluid interfaces are fundamentally different from those of hard particles. Unlike hard particles, which create significant interfacial deformation due to their rigid structure and fixed wetting properties, microgels adapt to the interface by deforming and spreading. When positioned at an interface, microgels exhibit a typical "fried-egg" or "core-corona" morphology, as shown by Cryo-SEM images of microgels at water/oil interfaces (**Figure 2. 7a**). At water/oil interfaces, the loosely cross-linked outer part of the microgel is more deformable than the densely cross-linked "core", allowing the microgel to conform to the interface. The outer part spreads out on flat interfaces, forming a flat "corona", while the core remains mostly in the water phase[52]. This deformation at fluid interfaces is caused by the combined effects of interfacial tension and their elastic properties, enabling microgels to cover a much larger interfacial area than rigid particles. Microgels with a larger shell-to-core ratio demonstrate more substantial absolute stretching[152, 153]. The capillary attraction for microgels is stronger due to the larger wetting radius and their surfaces being much rougher and more heterogeneous than those of rigid particles[154, 155]. Furthermore, the ability of microgels to deform

enhances their interfacial coverage, which can increase their overall stability and clustering potential under certain conditions. In the case of hybrid microgels that contain rigid cores, such as SiO_2-PNIPAM microgels, also present very similar "fried-egg" morphology[7, 89]. The rigid silica core remains unchanged, while the soft PNIPAM shell undergoes stretching at the air/water or oil/water interface, as illustrated in **Figure 2. 7b**. Interestingly, researchers point out that the interfacial behaviour of core-shell microgel particles is primarily governed by the properties of the shell, regardless of the presence of the core[156, 157].

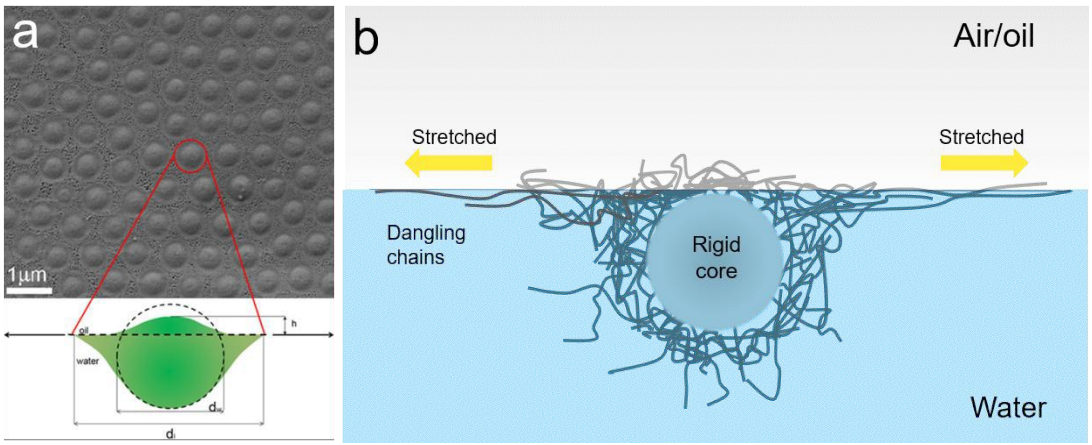

Figure 2. 7 The microgel deformations at interfaces. (a). FreSCa cryo-SEM images and related schematic representation of microgels at water/n-heptane interfaces imaged from the oil side. The microgel undergoes lateral spreading due to interfacial tension, forming a flattened conformation. Reprinted from ref. [158]. (b). Schematic diagram of a rigid-core/soft-shell microgels absorbed at the air/water interface. The microgel exhibits deformation at the interface with the soft outer part being stretched due to surface tension.

The lateral deformation of microgels reduces the system's free energy by minimizing interfacial tension more effectively than rigid particles. Consequently, the adsorption energy of soft particles can exceed that of rigid particles by several orders of magnitude[50]. Therefore, the adsorption process for soft particles cannot be fully captured by

$$E = \pi R^2 \gamma (1 \pm \cos\theta)^2 \quad (2.\ 24)$$

The total adsorption energy should include contributions from both interfacial tension reduction and the elastic energy of deformation. As a result, the deformability of microgels, which is significantly affected by the cross-link density, plays a crucial role in determining their adsorption efficiency, interfacial behaviour, and potential to form stable, close-packed assemblies at fluid interfaces[57].

The dynamic balance between interfacial energy minimization and elastic resistance defines the microgels' ability to form stable monolayers. Harnessing this balance enables precise control over interparticle spacing and lattice symmetry. The next step lies in translating these interfacial interactions into programmable strategies for constructing ordered 2D architectures, where external stimuli or geometric constraints can modulate assembly pathways.

2.2.3 Monolayer transfer onto solid substrates

Transferring the ordered microgel monolayers from flat interfaces to solid substrates and adjusting their arrays enables the creation of large-area nanopatterned monolayers. There are various methods for generating 2D ordered colloidal monolayers, including controlled evaporation[159-163], sedimentation[164], horizontal deposition[165, 166]. One common approach to generate 2D ordered microgel monolayer is by compressing or expanding a microgel monolayer in a Langmuir trough (**Figure 2. 8**) [68, 152]. The process begins with the formation of a microgel monolayer at the air-water interface, where the surface tension is measured using a Wilhelmy plate. As the barriers of the trough are moved inward, the interfacial area is systematically reduced, leading to a series of phase transitions that are theoretically predictable based on the microgels' softness, cross-linking density, and internal architecture[167, 168]. To transfer the

monolayer onto a solid substrate, the substrate is immersed into the liquid phase of the trough and lifted up during the compression process. This continuous transfer results in a well-defined monolayer on the solid substrate, ready for further characterization or analysis, such as AFM imaging[77]. This method allows for precise control of interparticle distances, regardless of charges or variations in microgel morphology, enabling the fabrication of tailored and highly ordered microgel arrays[88, 169, 170].

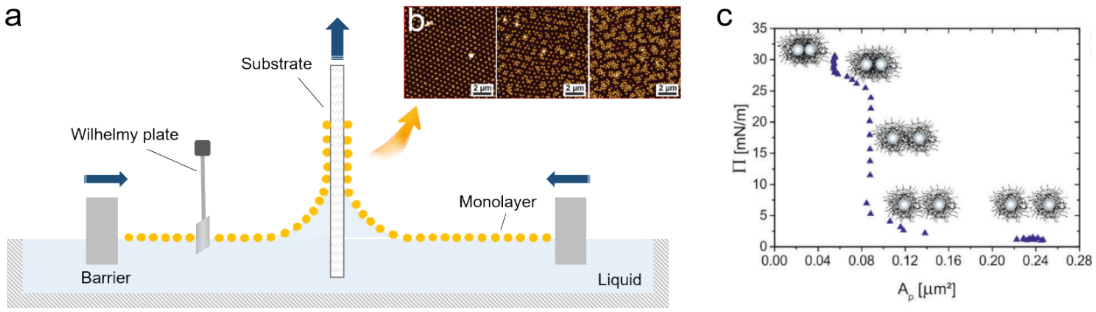

Figure 2. 8. Schematic representation of the Langmuir–Blodgett trough setup for controlling microgel monolayers at the water/oil interface. (a). Microgels are lifted by adjusting the surface tension with trough barriers. (b). AFM image of the resulting transferred monolayers at different compression states. (c). A compression isotherm demonstrates interparticle interactions from a non-contact state to a close-packed state during the compression process. Adapted from ref. [152].

Theoretical studies by Ciarella *et al.* have further elucidated the role of particle architecture in interfacial behavior. Using coarse-grained simulations, they demonstrated that microgels with inhomogeneous cross-linking densities or core-shell architectures exhibit distinct phase transitions during compression. These transitions are driven by the interplay between the microgels' compressibility and the many-body correlations that arise during compression. The theoretical framework developed in these studies provides a predictive understanding of how microgel architecture influences interfacial ordering and phase behavior.

Despite using a Langmuir trough, there is a simpler method for preparing microgel monolayers in simple vessels like a crystallization dish. This "freely floating" method , first introduced by Retsch *et al*. in 2009, eliminates the need for specialized equipment and instead leverages the intrinsic tendency of microgels to form ordered monolayers at fluid interfaces (**Figure 2. 9a**)[171]. Furthermore, the addition of surfactants, such as SDS, introduces a soft barrier that modulates the interfacial energy landscape, enabling the formation of hexagonally ordered monolayers with tunable interparticle spacing. Theoretical models predict that the spacing between microgels is inversely proportional to the surfactant concentration, providing a means to control the lattice parameters of the resulting arrays. This theoretical insight has been experimentally validated by Vogel and Ponomareva *et al.*, who demonstrated the formation of large-area, non-close-packed monolayers with tailored plasmonic properties (**Figure 2. 9b**)[19, 172]. Their work shows the potential of such method to create cm^2-scale samples with customized plasmonic properties.

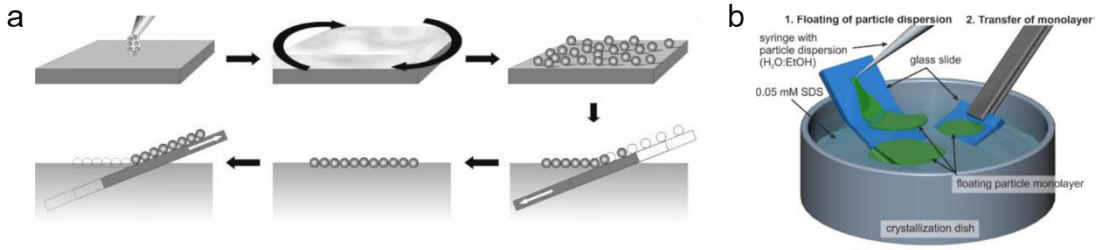

Figure 2. 9. Schematic illustration of the "free-floating" method for constructing a microgel 2D structure. (a). The microgels are first spin-coated onto a solid substrate to achieve a uniform distribution. The coated substrate is then inverted onto a liquid interface, allowing the microgels to transfer and assemble into an ordered monolayer at the interface. Once the structure is formed, the substrate is withdrawn at a certain tilt angle, transferring the monolayer onto the substrate. Adapted from ref. [171]. (b). The microgels are first dispersed in an ethanol/water mixture and then deposited onto the interface of an aqueous 0.05 mM SDS solution by flowing the dispersion along a glass substrate. The microgels self-assemble into a floating microgel monolayer at the interface. Finally, a glass substrate is used to lift the monolayer from the water surface, transferring it onto the substrate. Adapted from ref. [19].

2.3 Characterization techniques and image analysis

This chapter focuses on methods for studying microgels. In the bulk phase, microgels' dimensions and internal structural information are studied through SAXS and DLS. TEM is instrumental in visualizing the internal architecture of microgels. On the other hand, in the context of microgel monolayers transferred to solid substrates, AFM is employed to systematically investigate the interparticle spacing and lattice parameters under diverse experimental conditions.

2.3.1 Transmission electron microscopy (TEM)

TEM is an essential tool for analyzing nanomaterials due to its ability to achieve high-resolution images[173]. TEM operates by transmitting a beam of electrons through an ultra-thin specimen, producing detailed images of the material's internal structure, and even allowing the characterization of materials and dynamic processes such as nanoparticle growth, etching, and diffusion, at nanometric resolution in liquids[174, 175]. The short wavelength of electrons relative to visible light allows TEM to resolve features at the atomic level. This high resolving power enables TEM to distinguish between different components of complex structures, such as core-shell microgels with PNIPAM shell and different cores, by detecting variations in electron density (**Figure 2. 10a, b**). In these microgels, the cores are highly electron-dense compared to the surrounding PNIPAM shells, making it prominently visible in TEM images.

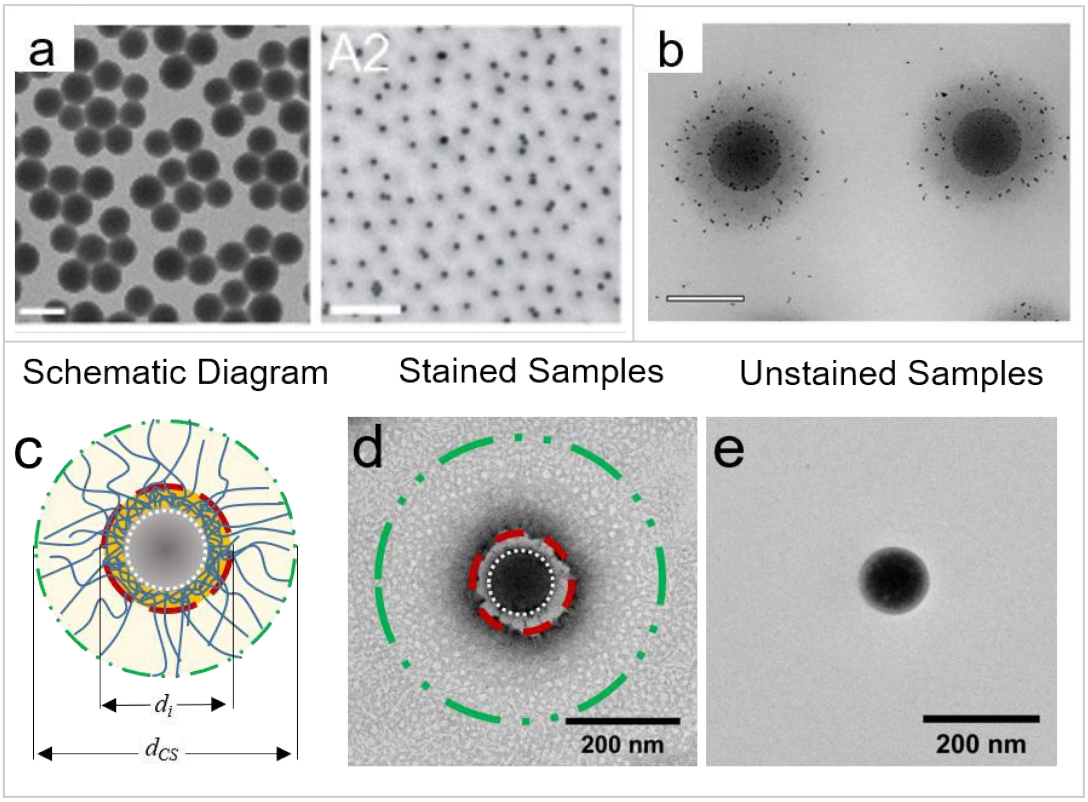

Figure 2. 10. TEM images of PNIPAM and SiO_2-PNIPAM microgels. (a). The left and right are TEM images of pure PNIPAM and SiO_2-PNIPAM particles. The scale bar is 100 nm. Reprinted from ref. [38]. (b). Cryo-TEM image of PS–core–PNIPAM–shell microgels stained with AuNPs. The scale bar is 200 nm. Reprinted from ref. [176]. (c). Schematic illustration of the internal structure of a SiO_2-PNIPAM particle. (d). TEM image of a SiO_2-PNIPAM particle stained with uranyl acetate. The inner shell structure is highlighted with red and green circles. (e). TEM image of an unstained SiO_2-PNIPAM particle, provided as a reference for comparison with the stained particle shown in (d).

Staining with heavy metal salts, such as uranyl acetate, significantly improves the contrast in TEM images by selectively binding to the polymer shell and increasing its electron density[177]. As depicted in **Figure 2. 10c**, **d** and **e**, the stained SiO_2-PNIPAM microgels exhibit a distinct contrast between the silica core and the polymer shell. The improved contrast achieved through staining is crucial for accurate structural characterization of the microgels. The red and green dashed lines indicate the boundaries of the inner and outer layers, respectively, enabling precise quantification of the shell's thickness and the core-shell interface.

2.3.2 Microstructure analysis by atomic force microscopy (AFM)

AFM is a high-resolution scanning probe technique that produces detailed topographical images even down to the atomic scale for various materials[178, 179]. A typical AFM setup consists of a cantilever with a sharp tip at its end, a laser source positioned above the cantilever, and a 2D photon detector that collects the reflected laser beam (**Figure 2. 11**). As the cantilever tip approaches and interacts with the sample surface, forces such as van der Waals, capillary, and electrostatic interactions cause the cantilever to bend. This bending alters the angle of the reflected laser, which is captured by the 2D photon detector, enabling precise measurement of the cantilever deflection. By scanning the probe across the sample surface, AFM records height variations and reconstructs them into a high-resolution grayscale digital image, where the brightness at each pixel corresponds to the local surface height. This technique provides a detailed visualization of the microgel monolayer arrangement on the substrate. Additionally, AFM phase imaging, which measures the phase shift between the oscillating probe and the sample surface, offers further insights into mechanical properties such as stiffness and adhesion.

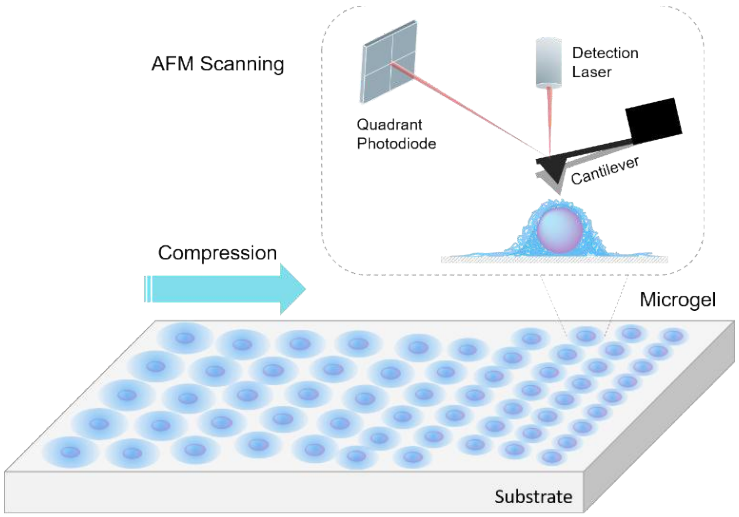

Figure 2. 11. Schematic diagram of the monolayer transferred to a solid substrate. The topography of the monolayer is imaged by AFM. A sharp cantilever tip scans the sample surface, while a laser beam is reflected onto a 2D photon detector to monitor cantilever deflection with high precision. This setup enables high-resolution topographical imaging of particle assemblies and surface morphology.

AFM is useful for analyzing microgel monolayer structures due to its capability to capture detailed spatial information at the nanoscale[68, 77, 180, 181]. Combining topographical and phase images enables a comprehensive understanding of the structural and mechanical characteristics of microgel monolayers. In this study, the AFM images were analyzed using Fast Fourier Transformation (FFT) and pair correlation function $g(r)$ to determine the positional information of the microgels in a transferred monolayer. These analyses offer valuable insights into the structural and spatial characteristics of the microgels.

The Fast Fourier Transform (FFT) is a powerful mathematical technique widely employed in image analysis, particularly within software tools like ImageJ. It is essential for image analysis and feature detection. It helps identify periodic interferences by transforming images from the spatial domain (real space) into power spectra in the reciprocal space (frequency domain)[182]. This transformation allows the topographical images obtained from AFM scanning to be decomposed into their spatial frequency components. Peaks in the FFT plot indicate orientation and periodicity information, enabling detailed surface morphology and defects analysis.

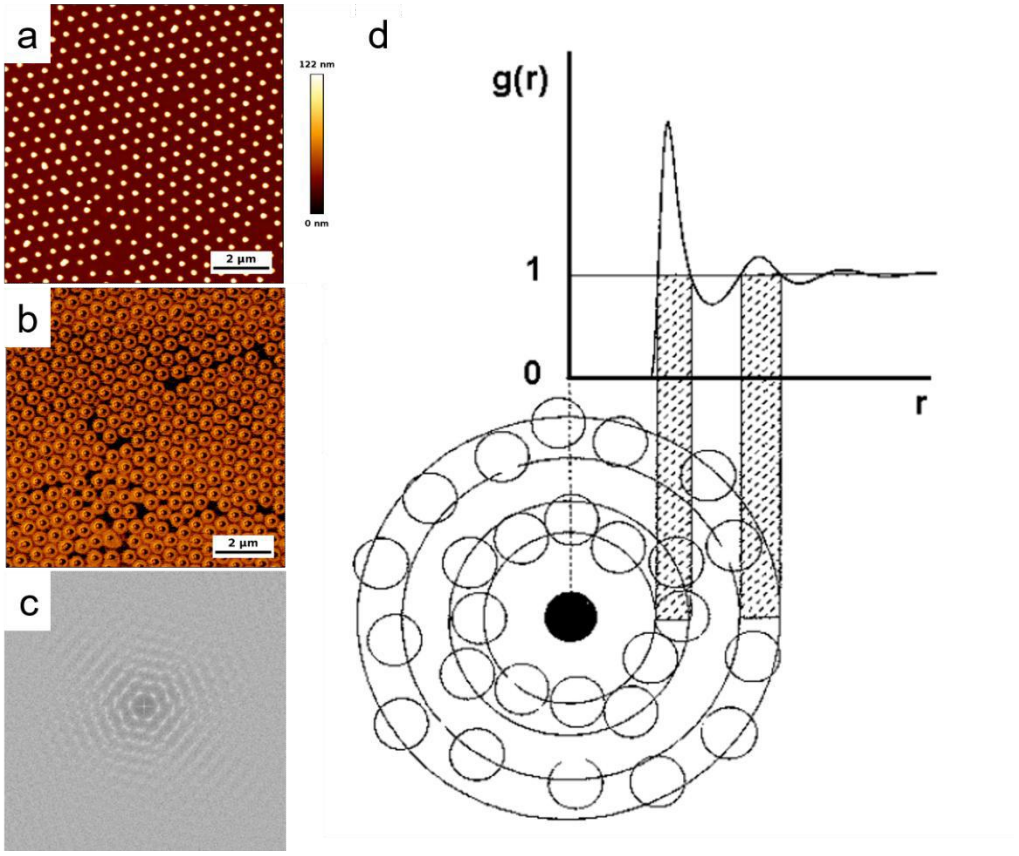

Figure 2. 12. AFM images and structural analysis of a SiO_2-PNIPAM microgel monolayer. (a). AFM height profile over a 10 × 10 µm² area, showing the topography of the microgel monolayer. (b). AFM phase image of the same region, highlighting variations in material properties and microgel interactions. (c). FFT analysis, presenting a zoomed-in cutout to reveal the periodicity and ordering of the microgel arrangement. (d). Schematic representation of the pair correlation function $g(r)$, illustrating the spatial distribution of microgels. Peaks in $g(r)$ correspond to preferred interparticle distances, indicating the degree of ordering within the monolayer. Reprinted from ref. [183].

The Continuous Fourier Transform (CFT) requires integrating over the entire continuous plane, which is not feasible for digital images. Therefore, for digital images like those produced by AFM, the Discrete Fourier Transform (DFT) is used to handle the discrete data. Once a height image is obtained from an AFM measurement, the FFT can be applied to transform this 2D schematic diagram into the frequency domain. The process begins by converting the height image into a grayscale format $f(r_1, r_2)$, where (r_1, r_2) is the positional coordinate in the real 2D space. The power spectrum of

this grayscale image in the frequency domain is denoted as $P(k_1, k_2)$. Here, (k_1, k_2) is the spatial frequency coordinate in the reciprocal space[184].

$$P(k_1, k_2) = |F(k_1, k_2)|^2 \quad (2.\ 25)$$

Where $F(k_1, k_2)$ is the Fourier Transform of $f(r_1, r_2)$, the resulting power spectrum reveals important characteristics of the surface being analyzed. Peaks in the power spectrum correspond to regular patterns or periodic structures on the surface, providing insight into the material's surface roughness, texture, and periodic features. The 2D FFT transform of an image with $N \times N$ pixels is defined as:

$$F(k_1, k_2) = \frac{1}{N} \sum_{r_1=0}^{N-1} \sum_{r_2=0}^{N-1} f(r_1, r_2) e^{-j\frac{2\pi}{N}(k_1 r_1 + k_2 r_2)} \quad (2.\ 26)$$

The DFT allows for the analysis of frequency components within a dataset. However, directly computing the DFT can be computationally intensive, especially for large datasets. To address this, the Fast Fourier Transform (FFT) is developed as an efficient algorithm to compute the DFT, significantly reducing the computational burden[185]. In this work, we use the FFT tool to analyze the frequency components of an image. By transforming the image data into the frequency domain, we can identify and study periodic structures, noise, and other significant features that are not easily discernible in the spatial domain.

In addition to the FFT, the Pair Correlation Function is another valuable tool for analyzing AFM images. It helps determine the spatial distribution and ordering of features in an image, making it particularly effective for assessing lattice structures and long-range order[186]. The pair correlation function $g(r)$ is defined as the ratio of the local particle density at a distance r from a reference particle to the average particle

density of the entire system (**Figure 2. 12d**)[187]. Mathematically, for particles in liquids, it is expressed as[188]:

$$g(r) = \frac{\rho(r)}{\rho_0} \quad (2.\ 27)$$

Here, ρ_0 is the bulk number density, representing the average number of molecules per unit volume in the system. $\rho(r)$ is the local number density, defined as the average number of molecules found at a distance *r* from a reference (central) molecule, normalized over all molecules and configurations. The radial distribution function $g(r)$ describes how the local density at a distance *r* compares to the bulk density. If $g(r) > 1$, it indicates that molecules are more likely to be found at that distance than in a completely uniform distribution, suggesting structural ordering. Conversely, if $g(r) < 1$, it suggests a lower probability of finding molecules at that distance compared to the bulk density, indicating a depletion zone.

The pair correlation function enables a quantitative analysis of the spatial distribution of microgels within the monolayer. For instance, in **Figure 2. 12**, in the AFM images, areas of regular or hexagonal ordering can be visually observed, while the $g(r)$ function quantifies this order through peaks at regular intervals, indicating typical distances between neighbouring microgels. The first peak in $g(r)$ represents the average nearest-neighbour spacing, with its height and sharpness reflecting the degree of short-range order; a high and sharp first peak suggests a well-ordered and closely packed arrangement, whereas a lower, broader peak indicates a more disordered structure. The FFT image further identifies periodicities and symmetries in the spatial distribution, corresponding directly to the $g(r)$ peaks, and helps to reveal the extent of periodicity, deviations, or defects within the lattice. This combined analysis offers

valuable insights into the structure and uniformity of the material, complementing each other effectively.

3. Contributions to joint publications

The following parts (**Chapter 4, 5 and 6**) of this thesis are adapted from the works that have been published previously or is in preparation for submission. The contributions of all involved authors are listed below.

Chapter 4: Experimental Section

The experimental parts are adapted from the joint publications presented in **Chapter 5** and **Chapter 6**.

Chapter 5: Tension-Driven Monolayer Evolution

The whole chapter is adapted from the published work: **Core–Shell Microgels at Air/Water Interfaces: Role of Interfacial Tension in Monolayer Evolution**

Author: Yichu Zhou, Jérôme J. Crassous, and Matthias Karg

Published in *Langmuir*, 2025, DOI: 10.1021/acs.langmuir.4c05050

Contribution: I performed the synthesis and characterization of the CS microgels, performed all experiments at liquid and solid interfaces, developed the methodology for time-dependent measurements, analyzed the data and wrote the initial manuscript draft. J. J. C. guided data analysis, provided physical explanations and interpretations, helped through fruitful discussions and edited the manuscript draft. M. K. conceptualized and supervised the project, was responsible for project administration and funding acquisition, guided data analysis and graphical representation and edited the manuscript draft.

Chapter 6: Monolayer Structural Discrepancies between *in-situ* and *ex-situ* Observations

The whole chapter is adapted from the manuscript in preparation for submission: **New insights into the assembly of core-shell microgels at air/water interfaces: Do we see what we are looking at?**

Author: Yichu Zhou, Andrey A. Rudov, Julia Fink, Igor I. Potemkin, and Matthias Karg

In preparation for submission.

Contribution: I performed the synthesis and characterization of the CS_5, CS_{10} and CS_{15} microgels, conducted all experiments at liquid and solid interfaces, analyzed the data, and drafted the initial manuscript. A.R. performed the computer simulations, analyzed the data, and co-wrote the initial manuscript. J.F. performed the synthesis and characterization of $CS_{2.5}$ and $CS_{7.5}$ microgels. I.P. supervised the project, oversaw data analysis and presentation, and provided project funding. M.K. conceptualized and led the project, managed administration and funding acquisition, supervised data analysis and presentation, and edited the manuscript draft.

4. Experimental Section

4.1 Materials

Tetraethylorthosilicate (TEOS; Sigma-Aldrich, 98%), ammonium hydroxide solution (NH3(aq.); Sigma-Aldrich, 30-33%), ethanol (EtOH; Chemsolute, ⩾99.9%), rhodamine B isothiocyanate (RITC; Sigma-Aldrich, mixed isomers), (3-aminopropyl) trimethoxysilane (APS; Sigma-Aldrich, 97%), 3-(trimethoxysilyl) propyl methacrylate (MPS; Sigma-Aldrich, 98%), sodium dodecyl sulfate (SDS; Merck; Ph. Eur.), N-isopropylacrylamide (NIPAM; Tokyo Chemical Industry, >98.0%), N,N′-methylenebisacrylamide (BIS; Sigma-Aldrich, 99%), potassium peroxodisulfate (PPS; Fluka, ⩾99%), hydrogen peroxide (Fisher Chemical, >30%), methanol (MeOH; Chemsolute, ⩾99.9%), and Hellmanex III (Hellma) were used as received. Water (H_2O) was purified using a Milli-Q system (Millipore), which resulted in a final resistivity of 18 MΩcm.

4.2 Synthesis

4.2.1 Synthesis of CS microgels

Synthesis and functionalization of silica cores. Dye-labeled silica (SiO_2) nanoparticles were synthesized on the basis of a protocol reported in the literature[30]. First, the functionalization of the RITC dye molecules was performed. Therefore, the respective amount of APS was added dropwise to an ethanolic solution containing RITC (10 mM) and stirred in the dark for at least two hours. The amount of APS was 10-fold excess to ensure covalent binding to the dye molecule. The functionalized dye

solution was diluted with ethanol in a ratio of 1:5. The silica particle synthesis was performed according to the Stöber method[31]. First, a solution of 125 mL of EtOH and 10 mL of NH_3(aq., 30–33%) was heated to 50 °C in a 250 mL three-neck round-bottom flask and then equilibrated for 20 min. The flask was equipped with a reflux condenser and a thermometer. Second, a mixture of 5 mL TEOS and 20 mL EtOH was equilibrated at 50 °C and then rapidly added to the solvent mixture in the flask. When the mixture became slightly turbid, indicating nucleation of silica, 2 mL of a dilute solution of functionalized RITC was added dropwise. After more than 12 h of stirring at 50 °C (overnight), the final dispersion was cooled to room temperature. The nanoparticles were purified by centrifugation at 2599 rcf for 90 min. The supernatant was removed, and redispersion was performed in EtOH. In the last step, the surface of the nanoparticles was modified with MPS to render the nanoparticles suitable for seeded precipitation polymerization and enable covalent binding between the shell and the cores. To do so the pH of the dispersion was adjusted to 9-10 by adding NH_3 (aq., 30–33%). Then 62 µL of MPS were added to the dispersion considering the resulting surface density of MPS of 1 molecule per 40 $Å^2$. To guarantee the covalent binding of the MPS molecules, the mixture was stirred for 24 h at room temperature and subsequently refluxed for 1 h. In the meantime, SDS dissolved in 1 mL EtOH was added dropwise to the mixture during cooling to stabilize the slightly hydrophobic, MPS-functionalized SiO_2 cores. The amount of SDS was adapted to obtain a final concentration of 0.2 mM. The stabilized silica particles were purified using centrifugation at 2599 rcf for 90 min and redispersion in ethanol. The purification step was repeated three times. 100 µL of the particle dispersion was transferred to a pre-weighed container and dried thoroughly. The mass of the remaining solvent was then measured, and the weight fraction of particles was calculated to be 0.155 g/mL. Ac-

cording to previous research conducted by *Masalov* et al., the density of silica, as observed in Stöber silica particles, is determined to be 2.2 g/cm^3[189]. The size of the silica cores was measured using SAXS, and the resulting diameter of the silica particles was found to be 105 ± 26 nm. The final number concentration of functionalized SiO_2 particles within the dispersion was calculated to be 0.193 μM.

Seeded precipitation polymerization. Free radical seeded precipitation polymerization was used to prepare SiO_2-PNIPAM CS microgels. The respective amounts of NIPAM, BIS, and SDS (1.4 mg) were dissolved in 20 mL of H_2O in a three-neck flask equipped with a reflux condenser. The reaction mixture was heated to 70 °C and degassed using nitrogen for 20 min. Next, the respective volume of the dispersion of functionalized SiO_2 particles was added. The reaction mixture was equilibrated for 15 min. Finally, 2 mg of PPS dissolved in 1 mL of H_2O was added to the mixture to start the polymerization. The reactions were allowed to proceed for 2 h and then cooled to room temperature.

Table 4. 1 lists the respective amounts of chemicals needed for the encapsulation of the SiO_2 particles in cross-linked PNIPAM shells. In the following, we will use CS_x as a label for all microgels, where CS stands for core-shell, and the index x corresponds to the nominal cross-linker content used in the synthesis. All synthesized CS microgels were purified by centrifugation ($CS_{2.5}$ – CS_{10} for 90 min at 2599 rcf; CS_{15} for 180 min at 2599 rcf) and redispersion of the residue with H_2O. Centrifugation and redispersion in H_2O after removal of the supernatant were repeated three times for each sample. Finally, the purified CS microgels were frozen in liquid nitrogen through rapid cooling and vacuum-dried for three days.

Table 4. 1. Masses of NIPAM monomer, BIS cross-linker, and volumes of the core stock dispersion employed in seeded precipitation polymerizations.

samples	*m* (PNIPAM) [mg]	*m* (BIS) [mg]	*V* (SiO_2) [μL]
$CS_{2.5}$	113	3.9	480
CS_5 [a]	800	54.6	5682
$CS_{7.5}$	113	11.5	333
CS_{10}	113	15.4	480
CS_{15}	113	23.1	333

[a] $CS_{2.5}$, $CS_{7.5}$, CS_{10}, and CS_{15} microgels were synthesized through a one-batch process. To produce a large quantity of CS_5 microgels, NIPAM and BIS monomers were fed twice to achieve the desired size, and were dissolved in 150 mL of H_2O. The two-batch synthesized CS_5 microgels present very similar shell morphology and swelling/de-swelling properties compared to one-batch synthesized CS_5 microgels (see **Appendix A.2**).

4.2.2 Synthesis of linear PNIPAM

Linear PNIPAM homopolymers were synthesized using free radical polymerization. Firstly, 9.41 mL DMF and 4.526 g NIPAM were added into a three-neck flask and heated in a silicon oil bath to 70 °C. The mixture was then degassed for 30 min with argon. Then, 0.005 g AIBN was solved in 0.5 mL DMF and added into the mixture. After 3 h of polymerization, the reaction was stopped by immersing the mixture in an ice bath and exposing it to air. The products were precipitated in diethyl ether and re-dissolved in acetone for three times. In the end, the final precipitated products were collected by centrifugation and dried under vacuum. According to the protocol, the nominal molecular weight of the synthesized linear PNIPAM is 82 kg/mol.

4.3 Sample preparation and characterization methods

4.3.1 Substrates for monolayer transfer

Hydrophilic substrates. The 76 × 26 × 1 mm glass slides (Epredia, The Netherlands) were first immersed into 2 vol% Hellmanex III in Milli-Q water and ultrasonically cleaned for 20 min. After rinsing with Milli-Q water seven to eight times to completely remove Hellmanex III, the glass slides were cleaned in an ultrasonic bath for 20 min in Milli-Q water and then for 20 min in ethanol. The glass slides were dried with nitrogen every time before using. The contact angle for water on the hydrophilic substrate is smaller than 5°.

Hydrophobic substrates. The glass slides were first cleaned according to the RCA cleaning process. The mixture of five parts H_2O and one part of NH_3 (aq., 30-33%) was heated to 80 °C. After adding one part of hydrogen peroxide (30%), the slides were immersed into the mixture for 15-20 mins, then rinsed with Milli-Q water and dried with nitrogen. The glass surface was then functionalized. The cleaned glass slides were immersed into MPS and then placed in a vacuum desiccator. The pressure was reduced to 20-30 mbar. After overnight reaction under vacuum, the glass slides were heated in the oven at 60 °C for 2 h. In the last step, the glass slides were sonicated in ethanol for 10 minutes and dried with nitrogen. The contact angle for water on the hydrophobic glass substrate is 85 -100°.

4.3.2 Monolayer preparation via freely floating methods

The spreading solution used for the monolayer preparation consisted of 1 wt% of microgels, 64 wt% of ethanol and 35 wt% of water. A crystallizing dish with an inner diameter of 70 mm and a PTFE ring with an inner diameter of 36.5 mm (40.5 mm outer diameter, 2.0 mm thickness) were used to prepare freely floating monolayers.

First, the crystallizing dish was filled with 85 mL of water. Then, the PTFE ring was positioned at the air/water interface and left there floating. A 3D-printed support frame is used to fix the ring in position (**Figure 4. 1**). Afterwards, 3 µL of the microgel dispersion was directly injected to the interface in the centre of the PTFE ring. The microgels self-assembled at the air/water interface, forming a homogeneous monolayer restricted by the ring.

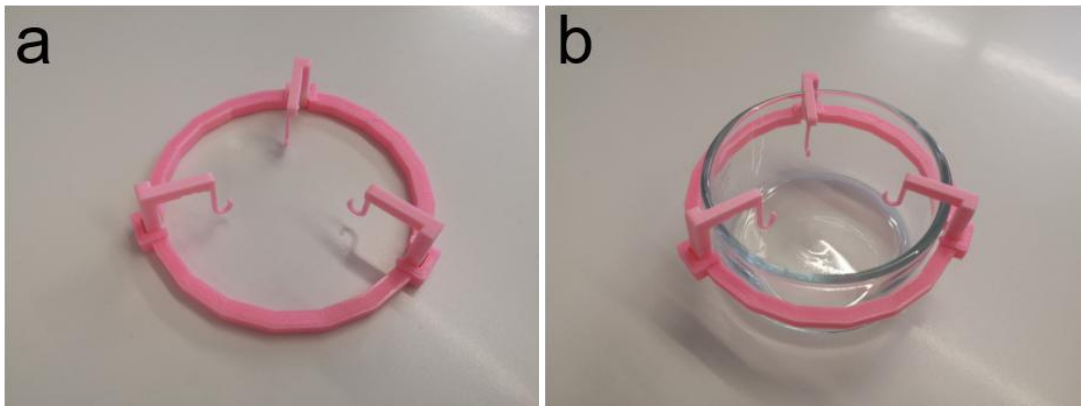

Figure 4. 1. A 3D-printed frame with multiple hooks designed for suspending the PTFE ring. The frame is placed on the table (a) and a crystallizing dish (b). The frame can be easily lifted by holding the circular part of the frame.

Monolayer manipulation by SDS. After forming a microgel monolayer in the ring, an SDS solution (16 mM) was carefully injected outside the PTFE ring with volumes adjusted to yield the final concentrations of 0.1 mM, 0.2 mM, 0.5 mM or 1.0 mM, respectively. The 16 mM stock concentration was chosen to enable uniform dropwise addition while minimizing premature SDS migration into the bulk phase, ensuring precise control of interfacial tension. Concentrations given throughout the manuscript refer to these final concentrations considering the total volume of the respective aqueous subphase. The PTFE ring was manually removed by vertically lifting the support frame with minimal lateral motion to avoid interface agitation. For systems with SDS

concentrations ⩾0.5 mM, where stronger adhesion between the hydrophobic PTFE and interface occurred, a clean fine needle was gently inserted at the ring-interface contact point to assist detachment. At this time ($t = t_0$), the monolayer was no longer confined and is considered a "freely floating monolayer" throughout this work. To transfer the monolayer, a hydrophilic glass slide (1×1 cm^2) was held at its edge with tweezers and gently submerged into the water from the edge of the dish. The slide then was carefully moved proximal to the centre of the monolayer to ensure that the monolayer's centre would align approximately with the centre of the slide upon transfer. The slide then was lifted vertically out of the water and kept upright while excess water was removed from its surface using a paper towel. Finally, the monolayer was rapidly dried with a heat gun by directing airflow onto the back of the slide[190]. The transfer was performed at different times after the removal of the PTFE ring. For each time point, the transfer procedure was repeated for at least three times, and every transfer was done using different, individually prepared monolayers.

Monolayer manipulation by PNIPAM homopolymer. After forming a microgel monolayer in the ring, 170 µL PNIPAM aqueous solution (0.001 wt%) was carefully injected outside the PTFE ring. After equilibrium for 10 min, the ring was carefully removed from the interface. From this time ($t = t_0$), the resulting "freely floating monolayer" was filmed, and later, the monolayer area was calculated based on the film. Then, for every stage of compression, 170 µL PNIPAM solution was added outside the monolayer and equilibrium for 10 min. After adding 510 µL PNIPAM solution (in total), the centre part of the monolayer was transferred to a clean glass substrate and dried with a heat gun.

4.3.3 SAXS

Transmission electron microscopy (TEM) was used to image the structure of the core-shell microgels. The measurements were performed on a JEOL JEM-2100Plus operating in bright-field mode at 200 kV acceleration voltage. Freeze-dried microgels were dispersed in 0.05 wt% ~ 0.06 wt % aqueous uranyl acetate solution. Then, the microgel solution was drop-casted on carbon-coated copper grids (200 mesh, Science Services) and dried for at least 1 h at room temperature before imaging.

4.3.4 DLS

A Zetasizer Nano S (Malvern) was used for measuring the hydrodynamic particle dimensions as a function of temperature. A 4 mW HeNe laser with 633 nm wavelength was used as the light source. The scattering angle of the device was 173º. The temperature range was set between 10 and 55 ºC in intervals of 1 ºC. The samples were measured for three times at each temperature. The data were analyzed using the cumulant method with the software provided by the instrument. Hydrodynamic diameters reported are z-averaged values.

4.3.5 TEM

Transmission electron microscopy (TEM) was used to image the structure of the core-shell microgels. The measurements were performed on a JEOL JEM-2100Plus operating in bright-field mode at 200 kV acceleration voltage. Freeze-dried microgels were dispersed in 0.05 wt% ~ 0.06 wt % aqueous uranyl acetate solution. Then, the microgel solution was drop-casted on carbon-coated copper grids (200 mesh, Science Services) and dried for at least 1 h at room temperature before imaging.

4.3.6 Pendant drop

A drop shape analyzer DSA25 (Krüss, Germany) was used to measure the interfacial tension of aqueous dispersions of the CS microgels. A drop of microgel solution was formed inside a rectangular, transparent cuvette (1 × 1 × 4 cm^3) to slow down the evaporation of the droplet. The volume of the droplet was set around 15 µL. The interfacial tension was measured until the microgels fully absorbed and reached a saturated state at the interface.

4.3.7 Interfacial tension measurements

The tensiometer mode of the Langmuir-Blodgett trough G2 (Kibron Inc., Finland) was used to measure the interfacial tension of the floating microgel monolayer and the microgel-free areas. A Wilhelmy plate (5 × 5 mm^2) was mounted in the centre of the monolayer or the microgel-free areas. The interfacial tension was measured every 0.2 s during the time-dependent monolayer experiments.

4.3.8 Determination of monolayer area

The time-dependent evolution of the freely floating monolayers was monitored by the camera of a mobile phone leading to videos with a resolution of 1080 pixels × 2240 pixels. The camera was fixed right above the monolayer. The pixel-to-real ratio was calibrated by the inner diameter of the crystallizing dish. The processing of the videos and the determination of the monolayer area at certain time points were performed using the program ImageJ.

4.3.9 LB trough

A Langmuir-Blodgett trough G2 (Kibron Inc., Finland) was used for the compression and deposition of the monolayers at room temperature. The area range of the trough is between 28000 mm2 to 4000 mm2. Before the experiment, the Langmuir trough and barriers were cleaned with EtOH and Milli-Q water. A 76 mm glass slide was

mounted vertically to the horizontal interface. After opening the barriers, the trough was filled with Milli-Q water until the water surface touched the barriers. The spreading solution consisted of 1 wt% of CS microgels, 64 wt% of ethanol and 35 wt% of water. The prepared spreading solution was injected directly to the air/water interface and equilibrated for 20 min before compression. Subsequently, the substrate was mounted on the dipper arm and the Wilhelmy plate (5 × 5 mm^2) was mounted in the centre of the trough. During compression, the moving speed of the barriers was kept constant at 0.77 mm/min. The monolayers were transferred to either the hydrophilic or the hydrophobic substrates by raising the slides for 55 mm at a rate of 0.14 mm/min. The transferred monolayers were dried at room temperature and then imaged ex-situ by AFM.

4.3.10 AFM

The dried, substrate-supported monolayers were analyzed by AFM NanoWizard 4 (JPK Instruments, Germany). The height profile of the central part of the monolayer was scanned in intermittent-contact mode with a scan rate of 0.5 Hz. 10 × 10 μm^2 images were recorded, acquiring 1024 × 1024 or 512 × 512 $pixels^2$. The measured height profiles were flattened (1st order) using the Dataprocess Analysis to exclude the tilt of the sample. We used ImageJ and WSxM 4.0 Beta 9.2 software to analyze the microstructure of the monolayers using the recorded height profiles.

5. Surface Tension-Driven Monolayer Evolution

Core-shell microgels can assemble at air/water interfaces, forming freely floating monolayers. However, the impact of interfacial tension imbalances between the microgel-covered and microgel-free areas remains underexplored. This chapter systematically examines monolayer evolution under tension gradients introduced by SDS or linear PNIPAM in surrounding areas. The study follows three key steps: (1) Synthesis and characterization of SiO_2-PNIPAM microgels with controlled cross-linker densities (CS_5, CS_{10}, CS_{15}), ensuring identical core sizes while varying shell softness; (2) Interfacial tension manipulation via SDS or linear PNIPAM homopolymer additions to create tension imbalances between microgel-covered and free regions; (3) Multiscale analysis: Real-time tracking of macroscopic monolayer area changes combined with microscopic AFM imaging to track monolayer structural (e.g., interparticle distance $d_{c\text{-}c}$) changes. By comparing expansion/compression kinetics across microgel types, this part of the work investigates the impact of interfacial tension on the behaviour of microgel monolayers at liquid interfaces and offers a robust alternative to Langmuir trough compression for tailoring 2D microstructures. The content of this chapter is adapted from ref. [191].

5.1 Swelling capacity of the CS microgels

Three different SiO_2-PNIPAM CS microgels were prepared by seeded precipitation polymerization using SiO_2 cores from the same batch. This means that all CS microgels have the same average core size and size distribution (105 ± 6 nm as determined by SAXS). To facilitate comparison, this work aims at CS microgels that fea-

ture similar shell thicknesses in the swollen state, i.e. at 25 °C (see **Table 5. 1**), but differ in cross-linker density, i.e. softness of the shell. The difference in cross-linking can be confirmed by studying the volume phase transition (VPT) of the CS microgels[192]. **Figure 5. 1a** shows swelling curves in terms of hydrodynamic diameters, d_h, as a function of temperature obtained from DLS. All three CS microgels show the typical VPT behaviour known from PNIPAM microgels in water. In the studied temperature window, there is a continuous decrease in d_h with increasing temperature with the strongest decrease at the VPT temperature that is approximately 34-35 °C for the three microgels. The difference in swelling capacity can be best expressed when comparing the relative change in hydrodynamic volume with respect to a reference state. **Figure 5. 1b** shows the temperature evolution of the swelling ratio β. To calculate β, the volume of the non-swellable SiO_2 cores was subtracted:

$$\beta = (V_{cs}(T) - V_{core}) \,/\big(V_{cs}(55\,°C) - V_{core}\big) \qquad (5.\ 1)$$

Here, $V_{cs}(T)$ corresponds to the hydrodynamic volume of the CS microgels at temperature T, V_{core} is the volume of the SiO_2 core based on the diameter from SAXS measurements, V_{cs} (55 ºC) is the volume of the CS microgel in its fully collapsed state at 55 ºC. The swelling ratios β show that, starting from the collapsed as the reference state, the CS_5 microgels increase in volume by a factor of approximately 14 when the temperature is reduced below the VPTT. In contrast, the highest cross-linked CS_{15} microgels show an increase in volume by a factor of only approximately 4. Now the results obtained from the CS_{10} microgels are set as representative microgels with intermediate cross-linking. The difference in swelling capacity will be relevant later on in the manuscript when directly comparing monolayers of the three CS microgels.

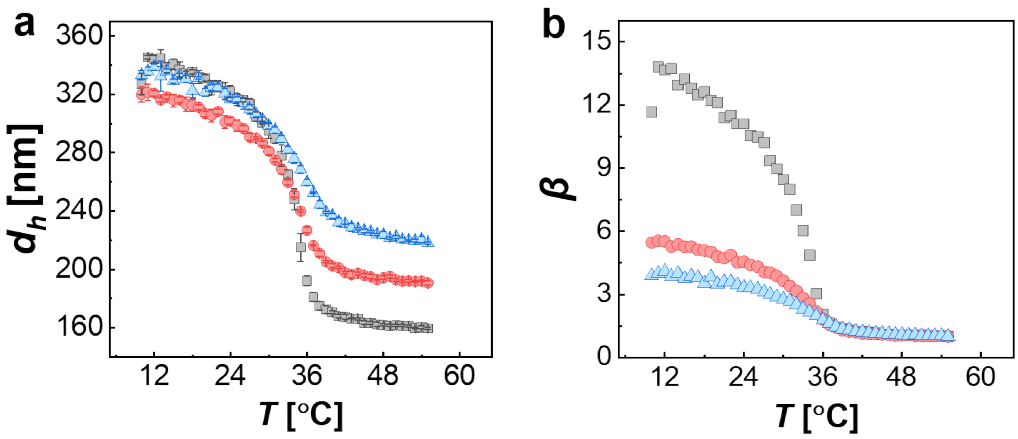

Figure 5. 1. Results from temperature-dependent DLS measurements for the different cross-linked microgels: CS_5 (grey), CS_{10} (red) and CS_{15} (blue). (a). Hydrodynamic diameters, d_h, as a function of temperature. The error bars correspond to the standard deviation from three measurements. (b). Corresponding swelling ratios β.

5.2 Freely floating monolayers at flat air/water interfaces

Freely floating monolayers of CS microgels can be prepared by simply injecting a spreading solution containing the microgels directly onto the air/water interface[19]. In the present case, our spreading solution consists of a mixture of 64 wt% of ethanol and 35 wt% of water and 1 wt% of microgels, which acts as a solvent for the microgels and facilitates their smooth spreading at the air/water interface due to Marangoni flow[193]. To study the time-dependent evolution of such monolayers, defining reference conditions at the start of the experiment ($t = t_0$). A simple protocol was developed to achieve this: (1) define the monolayer area in the reference state and (2) define $t = t_0$. This procedure is schematically depicted in **Figure 5. 2**.

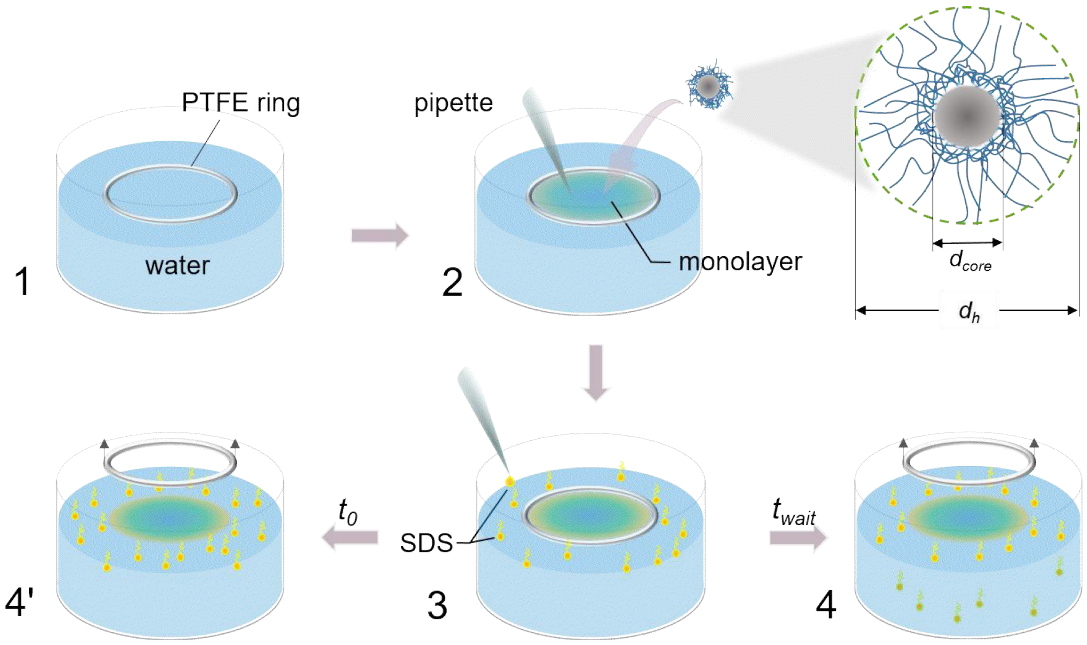

Figure 5. 2. Schematic diagram illustrating the preparation of a floating monolayer of CS microgels with core diameter, d_{core}, and overall hydrodynamic diameter, d_h, at air/water interfaces. A crystallizing dish was filled with water and a PTFE ring was positioned at the air/water interface (1). Upon injection of the microgel dispersion directly to the interface using a pipette, the forming monolayer was first restricted by the PTFE ring (2). Then SDS was injected to adjust the interfacial tension outside the PTFE ring (3). Finally, the PTFE ring was removed immediately (4') or after some equilibration time (4).

Upon filling a crystallizing dish with the desired volume of water (bulk subphase), a PTFE ring was placed at the air/water interface (1) with the help of a 3D-printed support frame (shown in **Figure 4. 1**). The spreading solution containing the CS microgels was then injected directly at the interface inside the PTFE ring (2). During the injection a monolayer of microgels is formed immediately filling up the available interfacial area. This strategy for confinement of a colloidal monolayer at fluid interfaces is similar to the one reported by Lotito *et al.*[194]. Depending on the volume of the injected solution, the area inside the ring could be completely filled with the monolayer. After the microgel deposition to the interface, 16 mM SDS stock solution was injected outside the ring dropwise. All SDS concentrations in this work (0.1–1.0 mM) are below the critical micelle concentration (CMC ≈ 8 mM), ensuring that inter-

facial tension reduction arises solely from monomer adsorption[195]. This avoids confounding effects from micelle formation, which could alter the dynamics of Marangoni flow. This way, the interfacial tension outside the PTFE ring could be adjusted by adjusting the amount of injected SDS solution. After removing the PTFE ring, a freely floating monolayer is obtained. The time of the removal of the ring defined the start of the experiment, i.e. $t = t_0$. The following part will discuss two different sets of experiments performed this way: (1) Equilibrium experiments, which I waited for long enough until a constant interfacial tension was measured outside the PTFE ring, and (2) Non-equilibrium experiments, where the ring was removed immediately after the SDS injection. First, the equilibrium experiments will be discussed. **Figure 5. 3** shows the time-dependent evolution of the interfacial tension, γ, measured within the microgel monolayer for different SDS concentrations, i.e. values of γ outside the monolayer.

For each of these individual experiments, the same volume of microgel dispersion was injected to the interface available inside the PTFE ring. Thereby, it is sure that experiments are comparable. Each of the individual experiments start with very similar numbers of microgels per area, N_p/A. The corresponding targeted initial interfacial tensions were approximately 49.0 mN/m. To guarantee that equilibrium was reached and stable values of γ were obtained outside the monolayer, let the dish stand and waited for 60 min (t_{wait} = 60 min) after injection of SDS to the outside of the PTFE ring prior to its removal. The stability of the monolayer within the ring is challenging to sustain beyond 60 min when the SDS concentration is higher than 0.5 mM. This suggests that at higher SDS concentrations, a small amount of SDS might migrate into the ring through the subphase, disrupting the integrity of the monolayer. **Figure 5. 3a** shows that, starting from t = - 5 min, i.e. prior to removal of the PTFE ring, initial

values of γ decrease with increasing SDS concentration. For 0 mM SDS, the interfacial tension remained at the constant value of 49 mN/m, which corresponds to the initially targeted value. For the highest SDS concentration of 1.0 mM, γ within the monolayer-covered area was measured as 43.2 mN/m. This decrease by almost 6 mN/m is related to SDS adsorption to the interface within the microgel monolayer-covered area during the equilibration time. Since this adsorption happened already before the removal of the ring, some mass transport must have occurred via the bulk subphase.

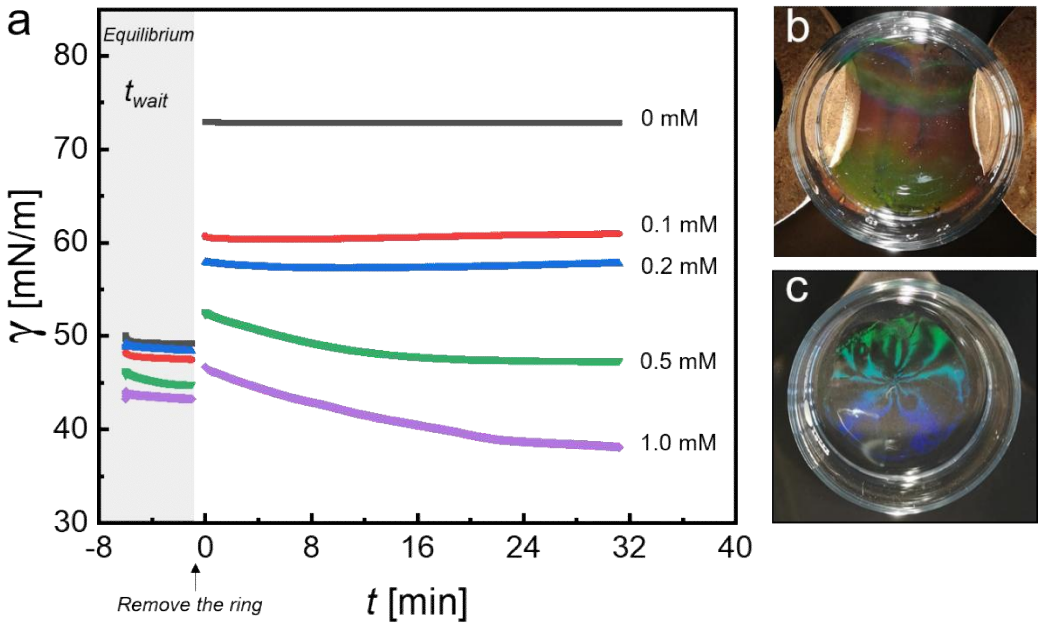

Figure 5. 3. Time-dependent evolution of the interfacial tension, γ, measured within the monolayer-covered (CS_{10} microgels) area for different SDS concentrations. (a) Interfacial tension as a function of time prior to (grey background) and after removal of the PTFE ring at $t = 0$ min. The SDS concentrations used to adjust γ outside the monolayer-covered areas were 0 mM, 0.1 mM, 0.2 mM, 0.5 mM and 1.0 mM, respectively. Photographs of the freely floating monolayer right after removal of the PTFE ring for 0 mM (b) and for 0.1 mM SDS (c).

Since the ring largely blocked mass transport to the monolayer, this procedure allows to adjust a difference of interfacial tension $\Delta\gamma$ inside and outside of the monolayer.

After removal of the ring, depending on the sign of $\Delta\gamma$ observed either expansion or shrinkage of the monolayer until $\Delta\gamma \approx 0$ mN/m. When the SDS concentration was 0 mM, 0.1 mM, or 0.2 mM, the interfacial tension values outside the monolayer were larger than 49.0 mN/m and monolayers expanded outward after removing the ring. These changes of the monolayer area happened instantaneously. In consequence of the expansion, the interfacial tension within the monolayer increased abruptly to 73.9 mN/m, 60.7 mN/m and 58.0 mN/m, respectively. These values remained nearly constant during the course of the experiments. In comparison, the expansion measured in a Langmuir-Blodgett trough occurs within an interfacial tension range of 43.0 mN/m to 70.5 mN/m (**Figure 5. 4**). When the SDS concentration was 0.5 mM, corresponding to a small $\Delta\gamma$, the value of γ abruptly increased to 52.6 mN/m after removal of the PTFE ring, and then slowly decreased to 47.4 mN/m. For 1.0 mM SDS, the initial equilibrium interfacial tension outside the monolayer is lower than within the monolayer. In this case, upon removal of the PTFE ring, γ first abruptly increased to 46.7 mN/m and then slowly decreased to a final equilibrium value of 38.0 mN/m. The first abrupt increase in interfacial tension for 0.5 and 1.0 mM SDS is attributed to the removal of the PTFE ring and the newly generated air/water interface with large interfacial tension in the area initially covered by the ring. In contrast to the monolayer expansion for lower SDS concentrations, the reported monolayer compression is time dependent involving slow relaxation processes probably related to local rearrangements.

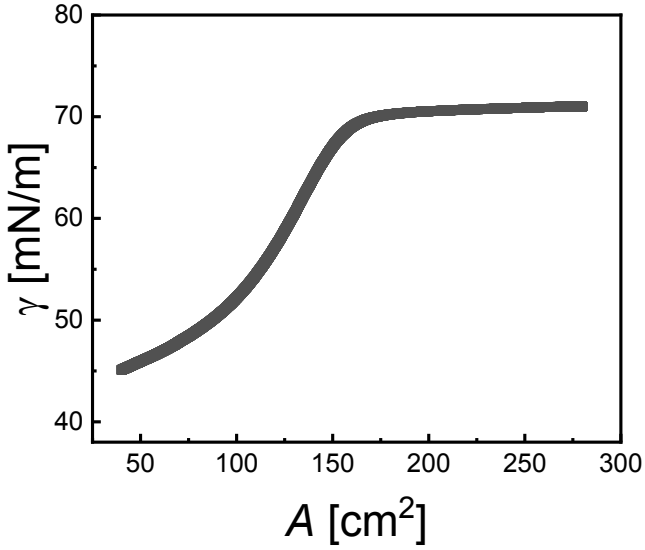

Figure 5. 4. Expansion isotherm of CS_{10} monolayer at the air/water interface in a Langmuir-Blodgett trough.

The freely floating monolayers were monitored with a digital camera placed above the experimental setup during these experiments. **Figure 5. 4b, c** shows photographs of the monolayer right after removal of the PTFE ring for 0 mM and 0.1 mM SDS, exemplarily. The monolayer is clearly visible due to the iridescence caused by the periodic arrangement of microgels with interparticle distances on the order of the visible wavelength. Comparing the two photographs, there is a difference in the iridescence colour with a reddish/green colouration for the experiment at 0 mM SDS and a greenish/blue colouration for 0.1 mM SDS. This difference in colouration is attributed to the different overall monolayer dimensions and, due to the very similar particle numbers in the monolayers, the difference in interparticle spacing. In the absence of SDS, the monolayer uniformly spreads across the entire available area in the crystallizing dish. However, when a concentration of 0.1 mM SDS is present, the monolayer covers a reduced area, resulting in shorter interparticle distances and consequently a more pronounced, blue-shifted iridescence. It can be concluded from the data of **Figure 5. 3**

that imbalances between the interfacial tension outside and inside the monolayer-covered area induce expansion or compression of the freely floating monolayer. **Table 5.1** summarizes the observations from these experiments and the relevant interfacial tension values.

Table 5. 1. Parameters and observations for CS_{10} monolayer experiments in dependence of SDS concentration, c(SDS). Initial interfacial tension at equilibrium measured outside the PTFE ring, $\gamma_{t=0}$ (SDS), initial interfacial tension of the monolayer at t = 0 min, $\gamma_{t=0}$(ML), and interfacial tension values of the monolayer, $\gamma_{t=32}$ (ML) measured after 32 min.

c(SDS) [mM]	**$\gamma_{t=0}$(SDS)[a] [mN/m]**	**$\gamma_{t=0}$(ML)[a] [mN/m]**	**Observation**	**$\gamma_{t=32}$(ML) [mN/m]**
0.0	72.9	50.0	Expansion	72.8
0.1	64.1	48.2	Expansion	61.0
0.2	60.4	48.8	Expansion	57.7
0.5	56.8	45.8	Stagnation	47.4
1.0	50.4	43.2	Compression	38

[a]Values were measured using a Wilhelmy plate after 60 min of equilibration time after the addition of SDS to the outside of the PTFE ring.

In the case of 0.5 mM SDS, $\Delta\gamma$ is small and it is possible to hypothesize that in this case the monolayer remains rather unchanged after removal of the PTFE ring. To confirm this hypothesis, the time-dependent evolution of the monolayer area for 0.5 mM SDS and direct AFM-based $d_{c\text{-}c}$ quantification were followed (**Figure 5. 5c-d**). **Figure 5. 5a** shows snapshots recorded at different times of the experiment. Again, the monolayer and its area can be distinguished due to its iridescence. Within the PTFE ring the confined CS microgel monolayer shows a purple-bluish colour that is more

difficult to see. In this starting scenario, the diffraction colour as captured by the camera is at the lower wavelength end of the visible spectrum, indicating relatively small interparticle distances at the initial stage of the experiments. At t = 0 min, i.e. immediately after removal of the PTFE ring, the monolayer could be easily identified with a green/blue structural colour. Critically, while the colour shift (e.g., purple to green) qualitatively reflects an increase in interparticle spacing over time, optical diffraction was not used to calculate $d_{c\text{-}c}$ values. Photographs taken at later times, i.e., at 5 and 15 min after removal of the PTFE ring, reveal freely floating monolayers of similar total dimensions and structural colours. To ensure measurement reliability, the experimental duration was limited to 15 minutes, as the central region remained stable within this timeframe, whereas peripheral instability—characterized by increased interparticle distances and reduced ordering, as reported by Volk *et al*. [19] —led to partial edge detachment beyond it (**Figure 5. 5**). **Figure 5. 5b** shows the detected total monolayer area, A, as a function of time starting right after removal of the PTFE ring. Over the course of the experiment, A was found to exhibit only a slight decrease that could relate to the slight decrease of the interfacial tension observed in **Figure 5. 3a.**

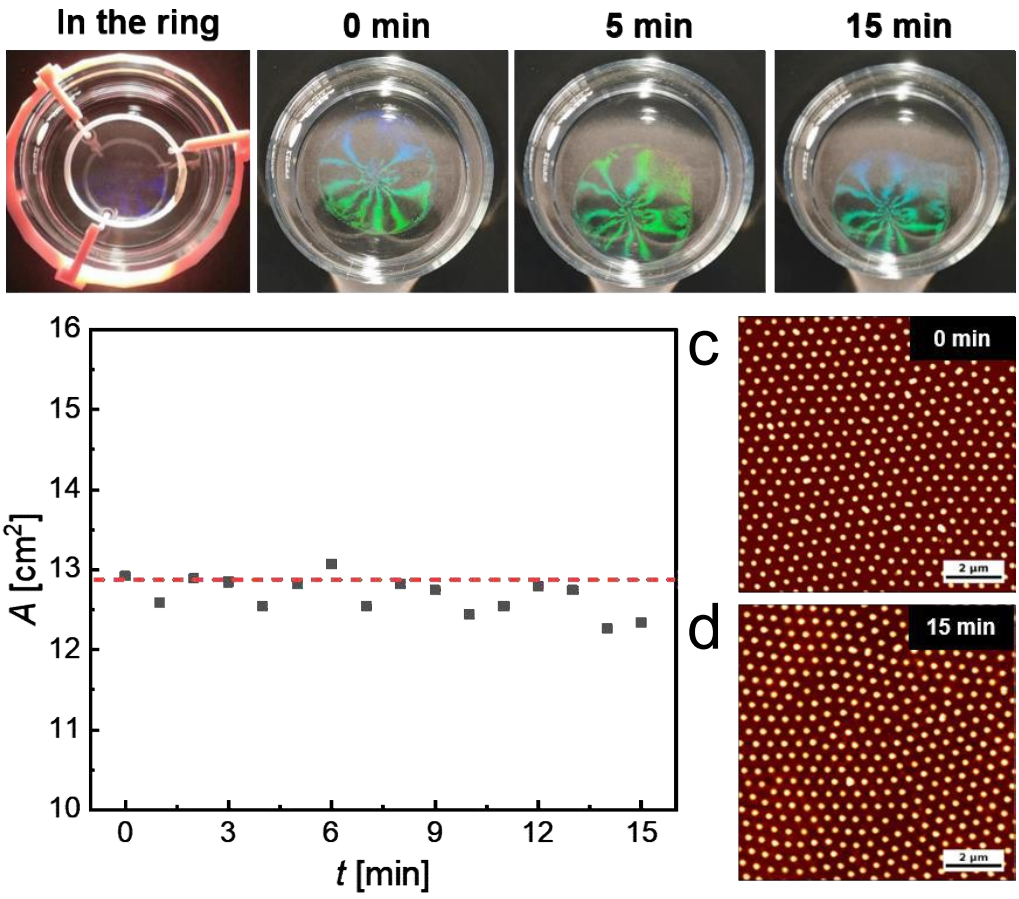

Figure 5. 5. Time-dependent evolution of the CS_{10} microgel monolayer for 0.5 mM SDS at equilibrium state (120 min equilibration time after SDS addition). (a). Photographs of the monolayer before and after different times of removal of the PTFE ring. (b). Time-dependent evolution of the monolayer area, *A*. The horizontal, red dotted line indicates the initial available area defined by the PTFE ring (based on outer radius). AFM height profile micrographs recorded from substrate-supported samples (*ex-situ*) withdrawn after 0 min (c) and 15 min (d).

Figure 5. 5c, d shows AFM height images recorded from monolayer samples that were collected at the beginning and end of the experiment. The microstructure in both images is very similar, and the nearest neighbour center-to-center distances, $d_{c\text{-}c}$, were determined at 469 ± 28 nm and 496 ± 31 nm for 0 min and 15 min, respectively. Note that these distances are largely greater than the hydrodynamic diameter of the CS microgels pointing to a "corona-corona" interaction throughout the whole expansion process. The initial $d_{c\text{-}c}$ of the monolayer (before removing the ring) was 438 ± 12 nm.

This slight increase in $d_{c\text{-}c}$ (approximately 10%) is in the order of the diameter that was initially occupied by the PTFE ring. i.e. the difference in the area of the ring was calculated using its inner and outer radius. That is to say, the microgels immediately filled the free interface formerly occupied by the ring. Worthwhile noting, the AFM micrographs capture only very small areas and thus small numbers of CS microgels representing the local microstructure. The differences in $d_{c\text{-}c}$ at the beginning and end of the experiment might point to local variations in microstructure (e.g. degree of order). Nevertheless, the combined data of **Figure 5. 5** reveal either stagnation or a very slight compression of the freely floating monolayer when interfacial tension imbalances are very small. In summary, the equilibrium procedure allows for the creation of a stable monolayer with a desired area by adjusting the SDS addition. However, when aiming to investigate the mechanism of monolayer expansion, an alternative procedure is necessary—one that is slow enough to facilitate the monitoring of the expansion process.

5.3 Equilibrium vs. non-equilibrium starting conditions

Figure 5. 6 shows photographs of freely floating CS_{10} monolayers after different times of the removal of the PTFE ring for 0.1 mM SDS, i.e., conditions where the monolayer is expected to expand. The photographs in the top row correspond to the case where the ring was removed 60 min after SDS addition. After removing the ring, the monolayer instantaneously expanded at the interface and then remained basically unchanged for a long period of time (**Figure 5. 6** top row). Under such conditions, the initial expansion of the freely floating monolayers caused by the significant interfacial tension imbalance occurred very fast – too fast to be monitored in our experiment.

The interfacial tension of the monolayer within the ring was measured to be 49 mN/m, with a corresponding monolayer area of 10.5 cm^2, as determined by the inner radius of the ring. Subsequently, upon removal of the ring, the monolayer area expanded to 17.8 cm^2, and this expanded area remained constant for a duration of 15 min (**Figure 5. 6**, top row). The area of the monolayer is not trackable after 15 min. The associated interfacial tension of the expanded monolayer was measured at 66 mN/m.

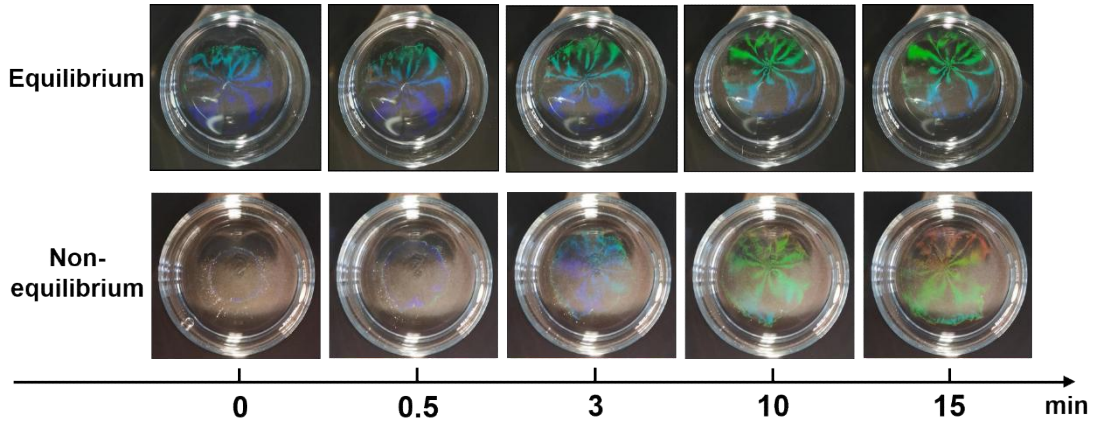

Figure 5. 6. Digital photographs of freely-floating CS_{10} monolayers taken at different times after removal of the PTFE ring. The concentration of SDS was 0.1 mM in these experiments. The images in the top row correspond to the equilibrium state after 60 min of equilibration, i.e. when the interfacial tension outside the monolayer had stabilized after addition of SDS. The images in the bottom row correspond to a non-equilibrium experiment, where the PTFE ring was removed right after the addition of the SDS. The photographs show the change of the monolayer area with SDS equilibrated for 60 min (top row) and immediately after SDS addition (non-equilibrium, bottom row).

In stark contrast, when the PTFE ring was removed right after the addition of SDS to the outside of the PTFE ring (non-equilibrium), the monolayer first rapidly compressed to a smaller size in the beginning (t = 0 min) and then expanded with increasing time (**Figure 5. 6**, bottom row). The corresponding quantitative evolution of the monolayer area over time is plotted in **Figure 5. 8a,** with images at each time point aligned to their respective data points. To track the evolution of the monolayer micro-

structure during expansion under non-equilibrium conditions, the monolayers were transferred onto solid substrates at various times after the ring was removed. The resulting substrate-supported monolayer samples were then investigated by AFM.

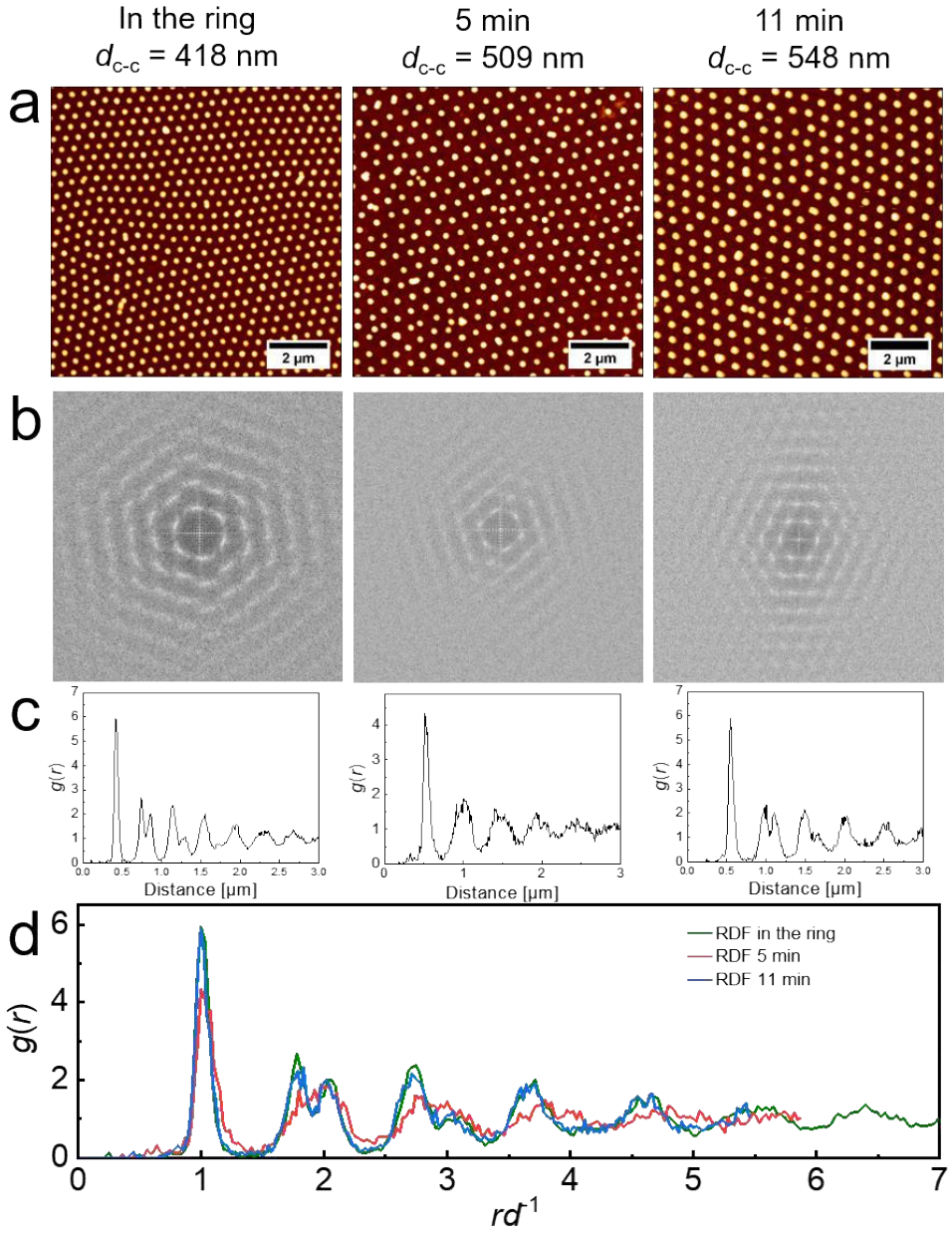

Figure 5. 7. Structural characterization of CS_{10} monolayers after transfer to glass substrates for an expansion experiment at 0.1 mM SDS. (a). AFM height profiles of the monolayers transferred from the air/water interface when confined inside the PTFE ring as well as 5 and 11 min after removal of the PTFE ring. (b). Fast Fourier transformations (FFT) computed from the corresponding AFM images shown in (a). (c). Radial distribution functions, $g(r)$, computed from the point maps of the AFM images. (d). Radial distribution functions normalized to the nearest neighbour center-to-center distance of the monolayers.

Figure 5. 7 shows AFM height profiles of monolayers transferred from inside the PTFE ring as well as 5 min and 11 min after the addition of 0.1 mM SDS and subsequent removal of the ring. The images reveal that the monolayer consists of microgels self-assembled into a homogeneous hexagonal lattice with a $d_{c\text{-}c}$ of 418 nm. With increasing time after removal of the PTFE ring, $d_{c\text{-}c}$ increased to 509 nm after 5 min and 548 nm after 11 min. At the same time the hexagonal order of the arranged microgels was maintained as shown by the large number of Bragg peaks in the fast Fourier transformations (FFTs) shown in **Figure 5. 7b**. The hexagonal order and the pronounced spatial correlation over several microgel diameters are further confirmed by the computed pair correlation functions ($g(r)$) in **Figure 5. 7c, d.** The $g(r)$s normalized in respect to their position of the first peak shown in **Figure 5. 7d** further indicate that the structural arrangement during the expansion is accompanied by a slight loss of structural ordering that is recovered after 11 min. In summary, the non-equilibrium procedure enables us to transfer the monolayer at different time points, allowing for the observation and investigation of the expansion process and the subsequent rearrangement of the monolayer microstructure.

5.4 Monolayer expansion at different external interfacial tensions

To further investigate the expansion behaviour of monolayers for different SDS concentrations under non-equilibrium conditions, the change of the monolayer area was monitored macroscopically by video recording from the top. **Figure 5. 8a-c** show the time evolution of the total monolayer areas obtained from image analysis. For all three SDS concentrations the monolayer areas at $t = 0$ min are on the order of 7-8 cm^2. This value is significantly lower than the initial monolayer area (10.5 cm^2) defined by

the area inside of the PTFE ring prior to the start of the time-dependent experiment. The immediate shrinkage observed in non-equilibrium experiments (e.g., 0.1 mM SDS, **Figure 5. 6**, bottom row) is attributed to a rapid imbalance in interfacial tension upon the removal of the PTFE ring. Before SDS reaches equilibrium, the surrounding interface exhibits a higher tension compared to the monolayer-covered region, inducing a transient compressive Marangoni flow. This compression, occurring on time scales too short to be directly monitored, leads to an initial decrease in monolayer area. Since the SDS stock solution was added onto the surface, and its subsequent diffusion throughout the bulk phase is a time-dependent process, there was a large surface excess concentration right at the beginning of the experiments. Desorption of the SDS excess takes place during the experiments leading to an increase of interfacial tension in the monolayer-free area and an increase in SDS concentration in the bulk subphase. This is accompanied by a continuous increase in monolayer area, $A(t)$, with time until approaching nearly constant values at the end of the experiments (15 min). The final value for 0.5 mM closely matches the values reported in **Figure 5. 3b**, indicating that a similar final equilibrium state is reached. The final values of $A(t)$ for 0.1 and 0.2 mM SDS are larger than the area initially defined by the PTFE ring. This means that both monolayers, at these low SDS concentrations, expanded with respect to the initial state. The solid lines in **Figure 5. 8a-c** correspond to fits according to:

$$A(t) = A_0 + \Delta A(1 - e^{-t/\tau}) \qquad (5.\ 2)$$

Here, A is the monolayer area, t is the expansion time, A_0 is A at t = 0 min, τ is the relaxation time, ΔA is the area difference between A_0 and A at t = 15 min. This model closely resembles the viscoelastic relaxation of a Kelvin-Voigt material subjected to a sudden stress. In particular, for the lowest and highest SDS concentration the agree-

ment between data and fit is very good**. Table 5. 2** lists the results from the fits to the data.

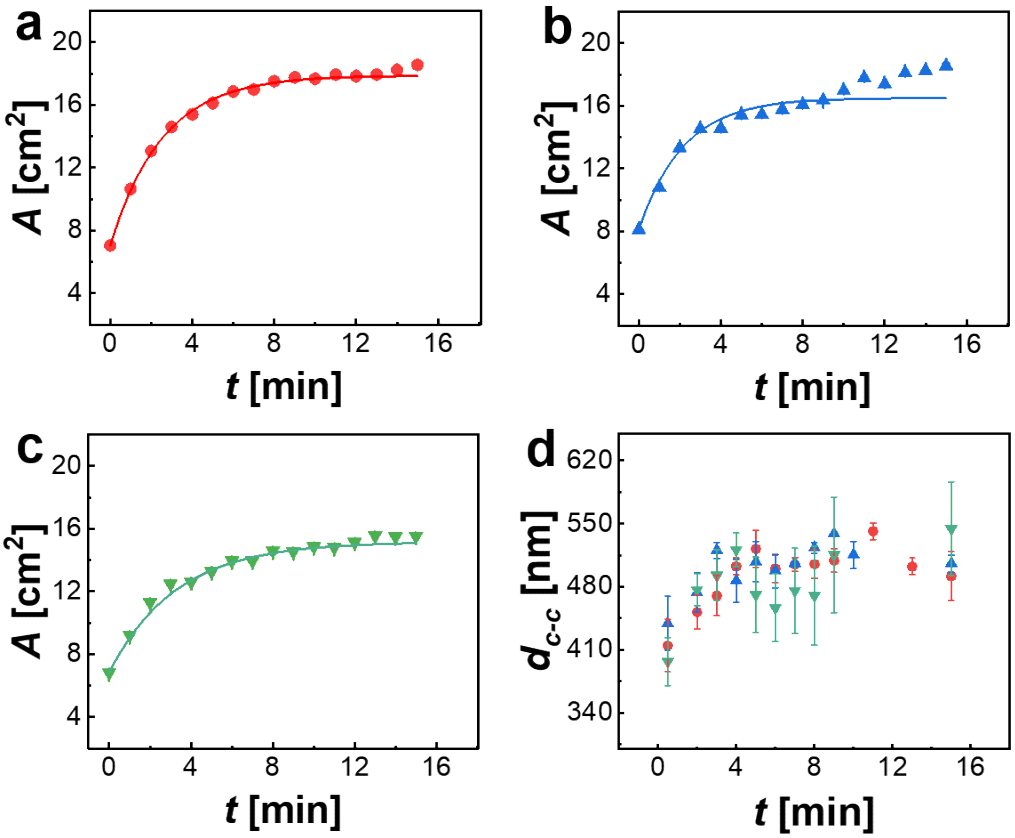

Figure 5. 8. Expansion kinetics of monolayers of CS_{10} microgels at the air/water interface for SDS concentrations of 0.1 mM (red), 0.2 mM (blue) and 0.5 mM (green). (a-c) The measured monolayer area *A* (symbol) and fits to the data according to equation (5.2) as solid lines. (d) Evolution of $d_{c\text{-}c}$ as a function of time obtained from *ex-situ* analysis by AFM of monolayers transferred to glass substrates.

Table 5. 2. Results from fits to time-dependent data (**Figure 7**) using equation (5.2).

c(SDS) [mM]	A_0 *[cm²]*	ΔA *[cm²]*	τ *[min]*
0.1	7.04	10.85 ± 0.04	2.54 ± 0.04
0.2	8.11	8.41 ± 0.08	2.18 ± 0.19
0.5	6.84	8.33 ± 0.16	3.28 ± 0.18

As expected, the total change in monolayer area, ΔA, is increasing with decreasing SDS concentration, i.e. increasing $\Delta\gamma$. The relaxation time, τ, is largest for 0.5 mM SDS and significantly decreased for the lower SDS concentrations indicating faster expansion of the monolayers for higher $\Delta\gamma$ that enhances the Marangoni flow. The trend in relaxation times, however, is not that clear, which might attribute to the less good fit to the data for 0.2 mM, which leads to the most unreliable value of τ (2.18 min).

To get a connection to local length scales, the central parts of the monolayers were transferred to glass substrates and imaged by AFM after drying. The time-dependent evolution of $d_{c\text{-}c}$ was extracted from image analysis. **Figure 5. 8d** shows a continuous increase in $d_{c\text{-}c}$ for all three SDS concentrations starting with values of approximately 410 nm. Due to the relatively large standard deviations in the values at each time point, extracting a clear correlation between local microstructural changes and SDS concentration is not possible. It is worth highlighting that rather small monolayer areas were probed by AFM leading to larger uncertainties. In addition, the transfer protocol to the solid substrates and the monolayer drying may have affected the microstructure in terms of degree of order and spatial arrangement – at least locally, as compared to much larger CS microgels where significant changes were observed depending on microgel softness and substrate wettability[196]. In addition, it is also possible that the kinetics of the monolayer expansion vary in the periphery of the monolayer as compared to its centre. To conclude, the expansion of the monolayer was observed from a macroscopic ($A(t)$) as well as local viewpoint ($d_{c\text{-}c}(t)$) for all three non-equilibrium experiments. To further support this correlation, the time-dependent evolution of $d_{c\text{-}c}$ was plotted in direct comparison to the theoretically calculated values based on the change in $A(t)$ in **Figure 5. 9**. The theoretical values were

calculated under the assumption that the monolayer with its area $A(t)$ contains a constant number of microgels during the expansion and maintains a perfect hexagonal arrangement with an area fraction of 0.91. The following equations were used to calculate the theoretical nearest neighbor distances:

$$d_e(t) = 2\sqrt{\frac{A(t)\cdot 0.91}{\pi N_p}} \quad (5.\ 3)$$

$$N_p = n_p \cdot A_{\text{ring}} \quad (5.\ 4)$$

Here, $d_e(t)$ is the theoretical $d_{c\text{-}c}(t)$, $A(t)$ is the monolayer area, N_p is the number of microgels in the monolayer, and 0.91 corresponds to the maximum area fraction for hexagonal packing of circles in 2D. Note that this calculation does not account for the possible microgel faceting at high monolayer compression. The number of microgels in the monolayer was calculated by equation (4. 4). Here, n_{p} is the number of microgels in a 10 × 10 μm^2 area of the monolayer in the ring, which was determined by AFM analysis, A_{ring} is the area of the PTFE ring calculated using the inner radius.

Figure 5. 9 shows that the experimental values closely follow the theoretical expectation and significant deviations are only observed for 0.1 and 0.2 mM SDS at longer times. In these two cases, the experimental values are smaller than the ones derived from the local microstructures. This might point to 1) lower degrees of order in the monolayer samples and/or 2) potential drying effects where immersion capillary forces reduce $d_{c\text{-}c}$. Specifically, drying effects during substrate transfer—such as capillary-driven isostructural phase transitions and localized shell deformations—can distort interfacial microstructures, as demonstrated in our prior study[196, 197].

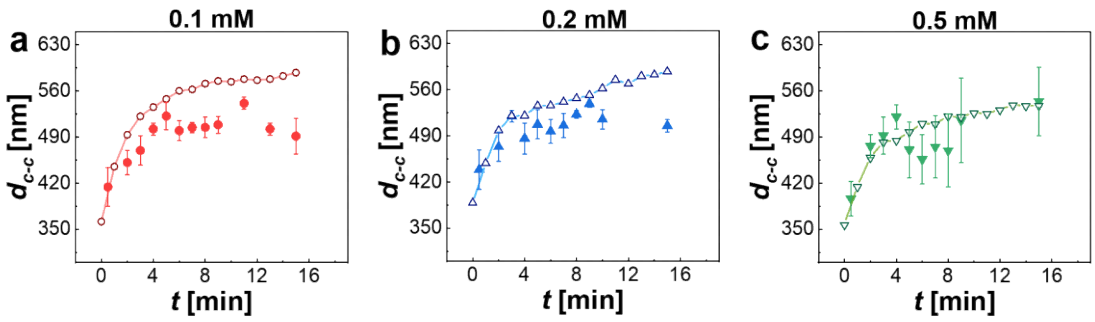

Figure 5. 9. Development of $d_{c\text{-}c}$ of CS_{10} monolayers over time for three different SDS concentrations of 0.1 mM (a), 0.2 mM (b) and 0.5 mM (c). The filled symbols correspond to experimentally measured values from microstructural analysis by AFM at given points in time. The open symbols and the corresponding guide-to-the-eye lines correspond to theoretically calculated values from measured total monolayer areas, $A(t)$, assuming hexagonal packing of the microgels in the monolayer.

Furthermore, since the expansion of the monolayer is driven from the outside of the monolayer, local changes in $d_{c\text{-}c}$ are expected to be larger in the outside region of the monolayer than in its central region. This would imply a radial gradient in $d_{c\text{-}c}$ values with smaller ones in the centre of the monolayer and larger ones at the periphery. In addition, the shape of the monolayer, the perturbation of the interface when removing the ring, and the drifting of the monolayer could also induce variations in the microstructure, which would result in different values of $d_{c\text{-}c}$ at different positions. Nevertheless, it can be clearly seen that the macroscopic expansion of the total monolayer is reflected by local changes in interparticle spacing. This means that it is possible to simply use interfacial tension to tailor the lattice parameter in crystalline microgel monolayers which is interesting e.g. for photonic and lasing applications.

5.5 Influence of cross-linker density on monolayer expansion

Next is to compare the time-dependent evolution of freely floating monolayer of CS microgels in dependence of the cross-linker density, i.e., the softness of the microgels[198]. To do so, monolayers of CS microgels with 5, 10 and 15 mol % cross-linker density (nominal) were prepared aiming at similar N_p/A by injecting the same volume of CS microgel stock dispersion with the same solid content. Initially, these monolayers were confined by the PTFE ring that also defines the monolayer area, A_0, at time $t = 0$ min. Upon injection of SDS (0.1 mM) outside of the PTFE ring, the PTFE ring was removed and the monolayer evolution was monitored (see **Figure 5. 2**).

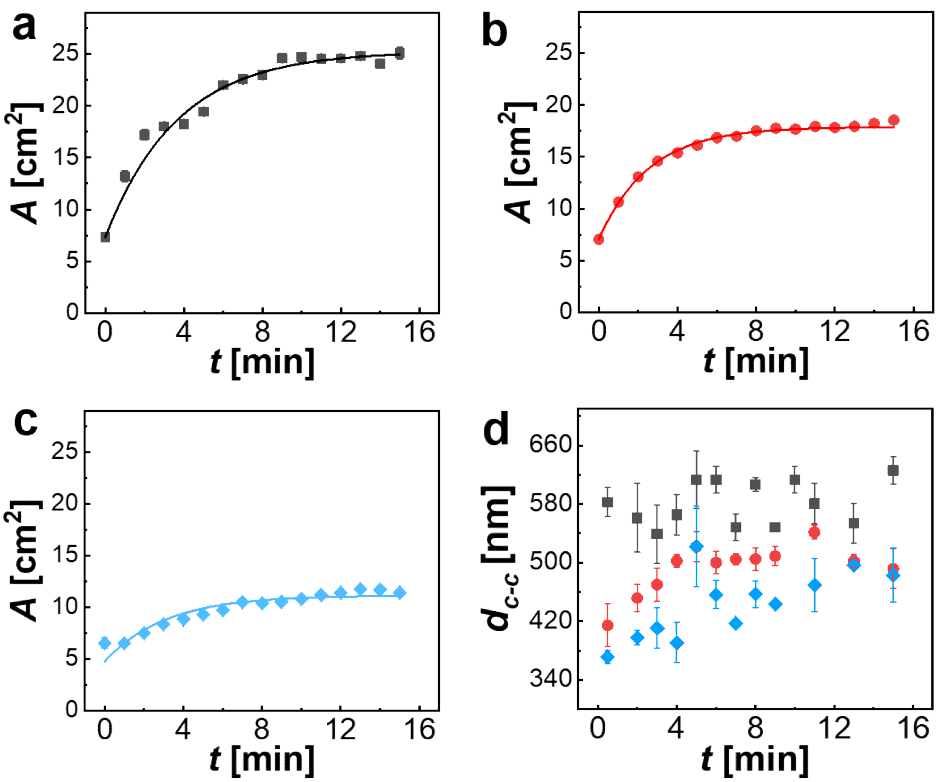

Figure 5. 10. Influence of cross-linker density on monolayer expansion for an SDS concentration of 0.1 mM. Black symbols correspond to 5 mol% (CS_5), red symbols to 10 mol% (CS_{10}) and blue symbols to 15 mol% (CS_{15}) cross-linking. (a). The measured monolayer area A (symbol) and fittings to the data according to equation (4.2) as solid lines. (b). Evolution of $d_{c\text{-}c}$ as a function of time.

Figure 5. 10 shows that for all cross-linker densities, the monolayer area, A, increased during approximately 10 min of the experiments and afterwards reached rather constant values. The extent of expansion, however, strongly depends on the cross-linking. With respect to the initial area (t = 0 min), the monolayers increased in area by 243% (CS_5), 164% (CS_{10}) and 76% (CS_{15}) within 15 min. The time-dependent evolution of the local microstructure was monitored by transferring samples from the central region of the monolayer to solid substrates and then imaging the dried monolayers by AFM. **Figure 5. 10d** shows the resulting time-dependent evolution of $d_{c\text{-}c}$ for the three CS microgels. A clear and significant increase is showed in $d_{c\text{-}c}$ with time for the medium and highest cross-linked microgels albeit the trend not being as clear as in **Figure 5. 10a, b** and **c**, and the standard deviations being large. For the lowest cross-linked CS_5 microgels the values of $d_{c\text{-}c}$ do not show a clear trend with time. This unexpected result might be related to the previously mentioned changes during monolayer drying, the rather poor statistics of the applied analysis of $d_{c\text{-}c}$ – at least in comparison to the large, macroscopic size of the total monolayer – and the potential distribution of interparticle spacings from the centre towards the outside of the monolayer. However, our findings point also to a difference between low and high cross-linked microgels. To further elaborate on this potential influence, further experiments and in particular support from theoretical simulations will be needed in a future study.

Once again, the data could be successfully fitted using the model depicted by equation (4.2). The fit results are summarized in **Table 5. 3**. Considering that all three experiments were done with the same amount of SDS and assuming that the desorption kinetics should be comparable, the differences in τ might attribute to be mostly related to the different moduli E of the microgels. And the largest value of τ for the lowest

cross-linked microgels points to the lowest value of E. However, it is noteworthy that the τ value for CS_{15} is unexpectedly larger than the value for CS_{10}. The total changes in monolayer area, ΔA, however confirm the expected differences in microgel softness, with the minimum change in area for the CS_{15} microgels, i.e. the microgels with the least deformable shell, i.e. the lowest swelling ratio β (see **Figure 5. 1b**).

Table 5. 3. Parameters obtained from fits (equation (4.2)) to the data shown in **Figure 5. 10** for the CS_5, CS_{10} and CS_{15} monolayers for 0.1 mM SDS.

Microgel	*[a] A_0 [cm^2]*	*ΔA [cm^2]*	*τ [min]*
CS_5	7.32	17.95 ± 0.15	3.68 ± 0.10
CS_{10}	7.04	10.85 ± 0.04	2.54 ± 0.04
CS_{15}	4.74 ± 0.55	6.41 ± 0.52	3.07 ± 0.24

[a]For the fits, A_0 values of CS_5 and CS_{10} monolayers were fixed using the experimental values measured at t = 0 min, while the A_0 of CS_{15} monolayer is the result obtained by fitting with A_0 as variable due to the lower visibility of this monolayer in the early stages and thus larger uncertainties in the experimentally measured monolayer areas at shortest times.

5.6 Manipulation of monolayers through linear PNIPAM homopolymer

The previous sections have shown how the interfacial tension imbalance influences the behaviour of microgel monolayers, i.e. expansion and compression depending on the sign of the interfacial tension difference. It can be controlled through addition of SDS that has a significantly different adsorption energy as compared to the used CS microgels. However, there was a strong desorption from the interface when an excess of SDS was purposely added to the surrounding interface. And there's indication that SDS can migrate into the microgel monolayer via diffusion from the bulk subphase. Thus it is necessary to address whether I can manipulate the monolayer extension and thus internal microstructure by adding linear PNIPAM homopolymer that is expected

to show similar adsorption energy at the air/water interface. Notably, while complete avoidance of contamination is challenging, the chemical identity between linear PNIPAM and the microgel shells ensures that any residual PNIPAM on substrates or in monolayers does not introduce extrinsic impurities.

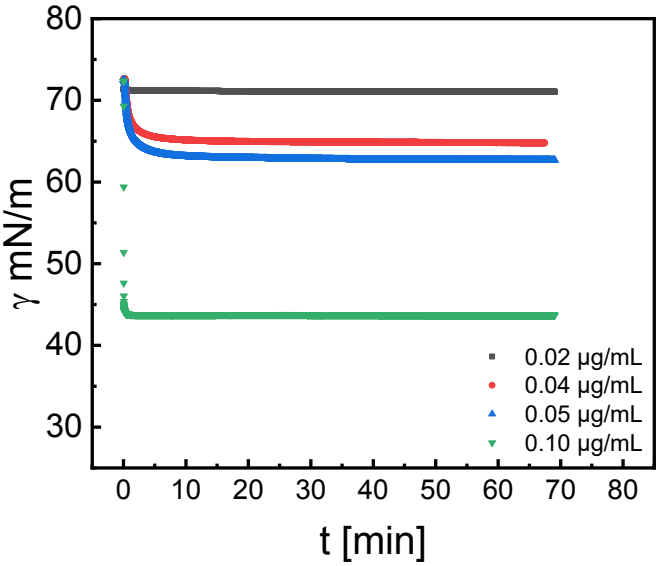

Figure 5. 11. Time-dependent evolution of interfacial tension γ of the air/water interface measured by a tensiometer after adding linear PNIPAM homopolymer. The concentrations of linear PNIPAM are 0.02 µg/mL, 0.04 µg/mL, 0.05 µg/mL, and 0.10 µg/mL, respectively.

Furthermore, due to the much larger steric hindrance of polymer chains as compared to the much smaller SDS molecules, it was expected that the migration of linear PNIPAM chains into the microgel monolayer will be hindered – if the PNIPAM chains leave the exterior interface at all. The results shown in **Figure 5. 11** reveal very stable and constant interfacial tension values for different amounts of linear PNIPAM upon a very short equilibration time of a few minutes. Critically, no spreading agent is required, as PNIPAM's intrinsic interfacial activity drives spontaneous adsorption and monolayer stabilization. These findings also confirm that desorption from the inter-

face is not occurring at these concentrations after a few minutes of equilibration time, eliminating bulk migration concerns.

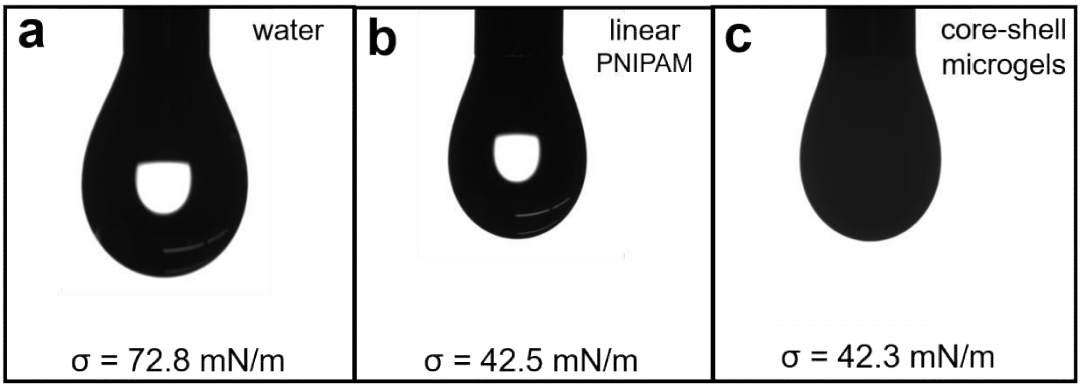

Figure 5. 12. Digital photographs of pendant droplets (aqueous) against air in the steady-state. (a). Droplet of pure water. (b). Droplet of a 0.001 wt% aqueous solution of linear PNIPAM homopolymer. (c). Droplet of a 2 wt% aqueous dispersion of CS_{10} microgels.

Firstly, pendant drop experiments were performed to compare the steady state interfacial tension upon self-adsorption to the air/water interface. **Figure 5. 12** shows snapshots of the pendant droplets with pure water in **(a)**, an aqueous dispersion of linear PNIPAM homopolymer (0.001 wt%) in **(b)** and the CS_{10} microgels in water (2 wt%) in **(c)**. Drop shape analysis revealed a interfacial tension for pure water of 72.8 mN/m in very good agreement to literature values for purified water[199]. In case of the dispersions containing either linear PNIPAM or CS microgels, constant values were achieved after approximately 10 min, indicating that equilibrium states were reached and that the interface was saturated. In both cases, similar final interfacial tensions of 42.5 mN/m (**Figure 5. 12** linear PNIPAM) and 42.3 mN/m (**Figure 5. 12c**, CS microgels) were measured. The similarity of these values shows that the reduction of interfacial tension by PNIPAM is independent of the exact morphology. This points to a similar volume fraction of PNIPAM in the interface volume at equilibrium. Simi-

larly, Zhang and Pelton reported values of approximately 43 mN/m for PNIPAM microgels independent of their cross-linker density[200]. Thus, it is also safe to assume that the adsorption energy is the same for linear PNIPAM and our CS microgels. Next is to study whether the linear PNIPAM homopolymer when added to the surrounding interface is suitable to compress a CS microgel monolayer when normalized to the respective total dimensions. Based on the results from the self-adsorption experiment (**Figure 5. 12**), the interfacial tension range suitable for manipulating the monolayer is determined to be 42.5 to 72.8 mN/m. This broad tunability, achieved by adjusting linear PNIPAM amounts (**Figure 5. 11**), validates its equivalence to SDS in tension modulation within overlapping regimes.

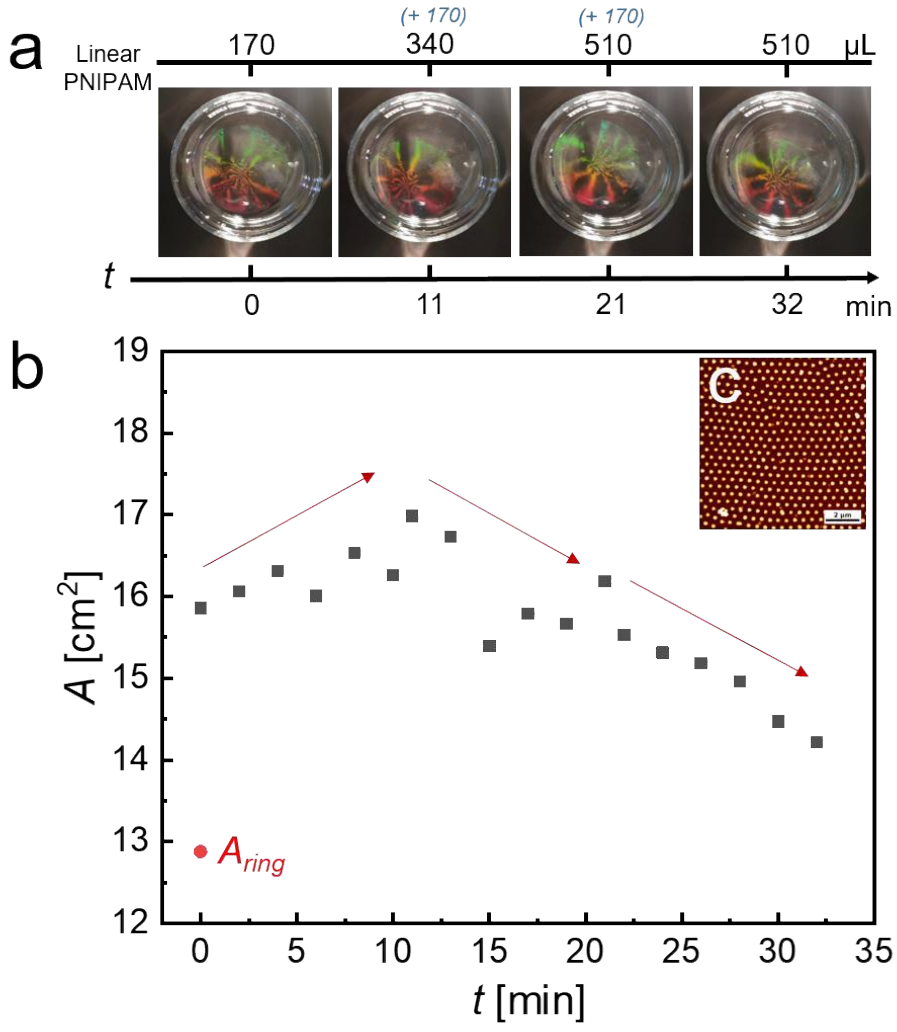

Figure 5. 13. Time-dependent evolution of the CS_{10} microgel monolayer area by adding linear PNIPAM solution outside the monolayer. (a). Stepwise compression of a CS_{10} microgel monolayer through sequential additions of linear PNIPAM (0.001 wt%, 170 µL per injection) to the surrounding interface. The amount of the linear PNIPAM solution added to the interface are showed above the captions; (b). Time-dependent evolution of the monolayer area, A. The red arrows aim to highlight the observed trends in changes of monolayer area. The red point (A_{ring}) indicates area defined by the PTFE ring (calculated by the outer radius of the ring). (c). The AFM height image of the monolayer transferred at the final time point (32 min).

Figure 5. 13 shows how to manipulate a CS microgel monolayer through the subsequent addition of linear PNIPAM to the surrounding interface. The area defined by the PTFE (A_{ring}) was 12.87 mm^2, which was calculated by the outer radius of the ring. 170 µL of a solution of linear PNIPAM (0.001 wt%) was added outside the PTFE ring and equilibrated for 10 min. Before removing the ring, the interfacial tension within the monolayer was 49 mN/m, and in the surrounding region containing the linear PNIPAM 61 mN/m. After removing the ring (t = 0 min), the monolayer area immediately expanded to 15.85 mm^2. In the next 10 min, the monolayer area slowly increased to 16.26 mm^2 driven by the higher interfacial tension outside the monolayer until the interfacial tension imbalance is vanished. Then at t = 11 min started a second addition of linear PNIPAM to the monolayer-free area by injection of another 170 µL of the 0.001 wt% solution. This initiated the compression of the monolayer from a total area of 16.98 mm^2 to 16.18 mm^2 within 10 min. In this case, it is needed to start with a lower interfacial tension in the surrounding leading to the compression of the monolayer. Lastly, a third addition of linear PNIPAM was performed, this time with another 170 µL injected at t = 21 min. This leads to another compression until reaching a final monolayer area of 14.21 mm^2 over the course of 10 min. The central part of the monolayer was transferred onto a solid substrate at the final state (t = 32 min) in order to study its microstructure by microscopy in the dried state (*ex-situ*). The monolayer exhibits a hexagonal order at the final state with $d_{c\text{-}c}$ = 469 nm (**Figure 5.**

13), which is very close to the value of the equilibrium starting condition (**Figure 5. 5**). These experiments confirm that the imbalance in interfacial tension is crucial for the behaviour of the monolayer of soft microgels and that the observed effects are rather independent on the architecture and size of the molecules influencing the interfacial tension outside the microgel monolayer.

6. Monolayer Structural Discrepancies between *in-situ* and *ex-situ* Observations

Understanding microgel assembly at air/water interfaces is crucial for designing 2D microstructures. Conventional methods rely on *ex-situ* AFM analysis of transferred monolayers, but whether these images accurately reflect true interfacial dynamics remains uncertain. This chapter integrates experiment results and DPD simulations to systematically investigate the interfacial assembly of SiO_2-PNIPAM microgels with varying crosslinker densities (2.5-15 mol%). Compression isotherms measured using a Langmuir-Blodgett trough reveal how shell architecture governs interfacial response. Monolayers at defined compression states were transferred for AFM imaging, enabling structural analysis. Experimental results are directly compared with DPD simulations, which model both compression and *in-situ* dynamics. Finally, by contrasting AFM data from hydrophilic and hydrophobic substrates, this work examines how substrate interactions induce *ex-situ* imaging artifacts. By integrating these approaches, it explores how cross-linker density influences microgel compressibility, interfacial ordering, and discrepancies between *in-situ* dynamics and *ex-situ* analysis.

6.1 CS microgels in the bulk phase

A series of CS microgels with same-sized, rigid silica nanoparticle cores and soft, deformable PNIPAM shells with nominal cross-linker densities between 2.5 - 15 mol % were used to investigate the role of the shell composition and softness on the behaviour of the microgels at the air/water interface. The diameter of the spherical silica cores is 105 ± 6 nm as determined by small angle X-ray scattering (SAXS) measurement and the form factor analysis **(Figure 6. 1**).

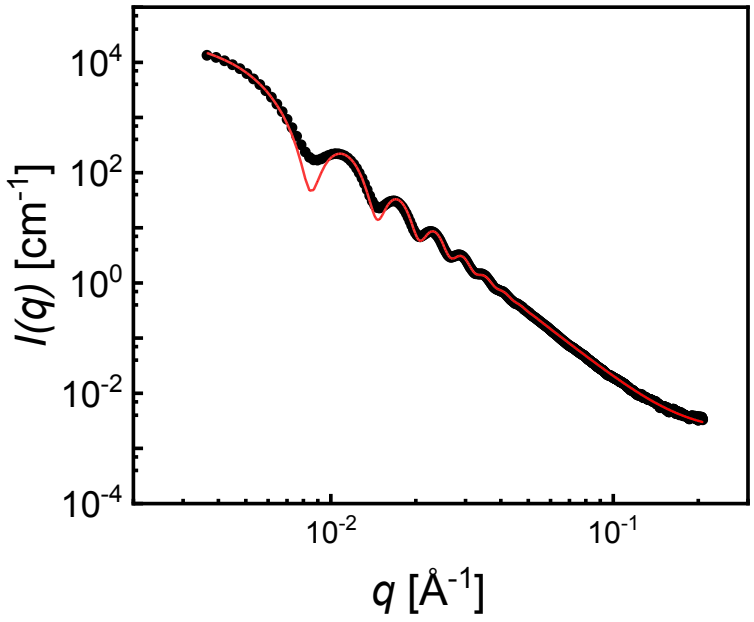

Figure 6. 1. Scattering curves obtained from SAXS measurements on SiO_2 particles. The black dots are the measured scattering profile, while the red curve is obtained from the model of a spherical silica particle. After fitting and adjusting various parameters, the obtained average radius is 105 ± 26 nm, with a polydispersity index (PDI) of 0.06.

The TEM images of the bare silica particles and uranyl acetate-stained microgels $CS_{2.5}$, CS_5, $CS_{7.5}$, CS_{10}, and CS_{15} are depicted in **Figure 6. 2a** and **b-f** respectively. The application of uranyl acetate staining enhances the visualization of the PNIPAM shell of the CS microgels. Unstained samples exhibit limited visibility of the shell (**Figure A. 3b, c**). TEM images reveal the structural features of CS microgels, with silica cores (depicted in yellow) positioned at the centre, surrounded by PNIPAM shells exhibiting visible inhomogeneity, evident through contrast colour variations. Interestingly, the inhomogeneity differs among the CS microgels. In the case of lower cross-linked microgels like $CS_{2.5}$ and CS_5, the silica core is surrounded by a fuzzy shell. Conversely, higher cross-linked microgels, $CS_{7.5}$, CS_{10}, and CS_{15}, present a significant inner layer, which is primarily shown in a lighter shade of purple, between the

silica core (yellow) and the outer fuzzy shell (darker purple colour). The boundary between the inner and outer layer appears as an orange halo, where the concentrated stain, having a higher electron density than the polymer, creates a contrast distinct from the PNIPAM shell. The double-layer structure is more prominent in higher cross-linked microgels.

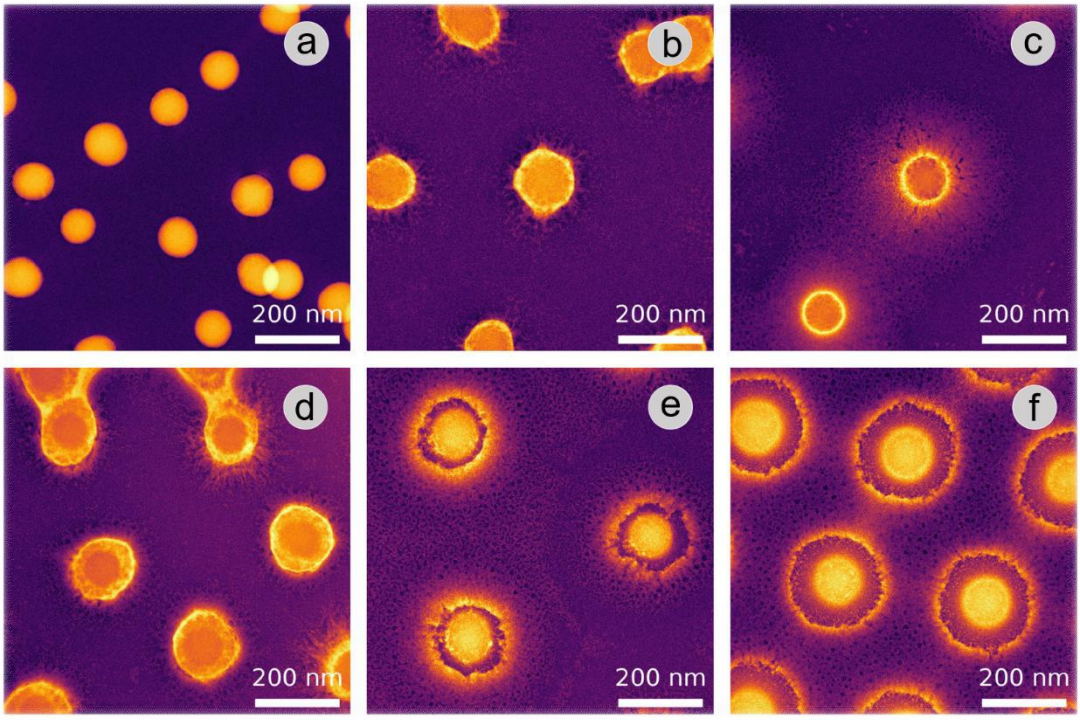

Figure 6. 2. TEM images of silica cores (a) and stained $CS_{2.5}$, CS_5, $CS_{7.5}$ and CS_{15} microgels with different cross-link densities (from b to f, the cross-linker densities are 2.5, 5, 7.5, 10 and 15 mol%, respectively). An inverted inferno-scale colour scheme was used.

The clear distinction between the silica core, inner shell, and outer fuzzy shell is demonstrated in **Figure 6. 2**. This phenomenon is related to the inhomogeneity of the cross-linker distribution within the polymeric shell. The fuzzy shell character is known for purely PNIPAM microgels and confirmed by the small angle neutron scattering (SANS) experiments[42]. For one-batch synthesized PNIPAM microgels via precipitation polymerisation, a higher degree of cross-linking density is expected in-

side the microgel than outside. Furthermore, Ponomareva *et al*. reported that the Au-PNIPAM microgels, which contain small gold nanoparticle cores with PNIPAM shells, also possess a fuzzy-sphere-like morphology with a higher cross-linked core and a loosely cross-linked fuzzy shell[10]. Such cross-linking gradient is explained by the higher reactivity of the BIS compared to the NIPAM monomer during one-batch synthesis, resulting in a cross-linker gradient from the centre to the periphery[43]. The average dimensions of the inner highly cross-linked microgel region can be determined from the images. The average dimensions of the inhomogeneities (diameters, including silica core and inner shell), d_i, are 146, 190, and 261 nm for the $CS_{7.5}$, CS_{10}, and CS_{15} microgels, respectively.

Temperature-dependent DLS measurements were used to analyze the dimensions and the swelling/deswelling abilities of the CS microgels. DLS measurements conducted at 25 °C show that the microgels exhibit an overall hydrodynamic diameter ranging from 300 to 320 nm (see **Figure 6. 3a**). Notably, all samples demonstrate a nearly uniform shell thickness in the swollen state, irrespective of the cross-linker density. The evolution of the R_h with temperature is shown in **Figure 6. 3a**. PNIPAM CS microgels show the typical VPT behaviour known from PNIPAM-based microgels, i.e., the radius decreases continuously starting from the swollen state at low temperatures until reaching the collapsed state dimensions at temperatures of approximately 40 °C and higher. The swelling curves were analyzed to assess the VPT temperatures (VPTT). The determined VPTTs, in the range of 33.3 °C and 34.6 °C, demonstrate a slight increase with increasing cross-linker content, as also reported in the literature for purely organic PNIPAM microgels[201] and also reported for CS microgels with gold nanoparticle cores and different cross-linker densities[202].

Table 6. 1. The table includes data on the size of the silica core (d_{core}) obtained from TEM, hydrodynamic diameter in the swollen state (d_h), polydispersity (PDI) from DLS, volume-phase transition temperature (VPTT), and deswelling ratio (α) at 55 °C for various CS microgels.

Sample	***Nominal cross-linker density* [mol%]**	**d_{core} [nm]**	**d_h [nm][a]**	***PDI***	***VPTT* [°C]**	**α (55 °C)**
CS$_{2.5}$	2.5	105 ± 3	308 ± 3	0.048	33.3 ± 0.1	0.081
CS$_5$	5	105 ± 3	305 ± 4	0.021	34.4 ± 0.1	0.085
CS$_{7.5}$	7.5	105 ± 3	306 ± 4	0.009	33.8 ± 0.2	0.155
CS$_{10}$	10	105 ± 3	316 ± 5	0.016	34.4 ± 0.2	0.183
CS$_{15}$	15	105 ± 3	305 ± 7	0.004	34.4 ± 0.5	0.257

[a] ***d_h*** was recorded at 25 °C

As the cross-linker content increases, the hydrodynamic diameter of the microgels in the collapsed state also increases, which suggests a decrease in swelling capacity with the increasing cross-linker content. To demonstrate the difference in the swelling capacity, the de-swelling ratio α can be calculated:

$$\alpha(T) = \frac{V_{cs}(T) - V_{core}}{V_{cs}(15\ ℃) - V_{core}} \qquad (6.\ 1)$$

Where $V_{CS}(T)$ and V_{CS}(15 °C) are the hydrodynamic volumes of the microgel at a respective temperature T and in the swollen state (15 °C), respectively. V_{core} corresponds to tbhe volume of the rigid core.

As the cross-linker content rises from 2.5 % to 7.5 %, α increases from 0.081 to 0.257, indicating that the microgels become more rigid[40]. Interestingly, the swelling and de-swelling curves of $CS_{2.5}$ and CS_5 almost overlap, indicating similarities between the internal shell structures, which agrees with the observation from the TEM images where the lower cross-linked ($CS_{2.5}$ and CS_5) microgels do not possess the inner shell structure present in highly cross-linked ones ($CS_{7.5}$, CS_{10} and CS_{15}). This observation suggests that the formation of the highly cross-linked inner part might occur only when the concentration of the cross-linkers reaches a critical value.

Based on the experimental observation, to simulate the shell with similar composition swelling/de-swelling behaviour and interfacial behaviour, a series of CS microgels (CS_5, CS_{10} and CS_{15}) were designed and created, detailed information can be found in the **Appendix A.6** and **A.7**. All samples contain identical solid cores represented by a spherical nanoparticle of radius, $R_{core} = 6.5 \pm 0.2r_c$. Here, r_c is the effective size of a simulation bead corresponding to a cluster of four water molecules. The microgels' internal structures were systematically adjusted, including the size of inner and outer shell regions and cross-linker distribution. This optimization process enabled the replication of the experimental swelling curves accurately.

Figure 6. 3d-e illustrates the equilibrium structure of final microgels used in the present work in a swollen state in bulk water, showcasing their morphology. The colour of the shell beads indicates the distribution of polymer density. The inferno colour scheme is employed, where the transition from orange (representing the area with the highest polymer density) to red and purple (indicating areas with lower polymer densities) signifies the decrease in polymer densities. CS_5 exhibits an almost homogeneous internal structure with a slight increase in cross-linkers near the solid core, as con-

firmed by the radial density profile in **Figure A. 7a.** CS_{10} and CS_{15} showcase pronounced double-shell structures, featuring a highly cross-linked inner part and a gradually decreasing cross-linking density towards the outer periphery (**Figure A. 7b, c**).

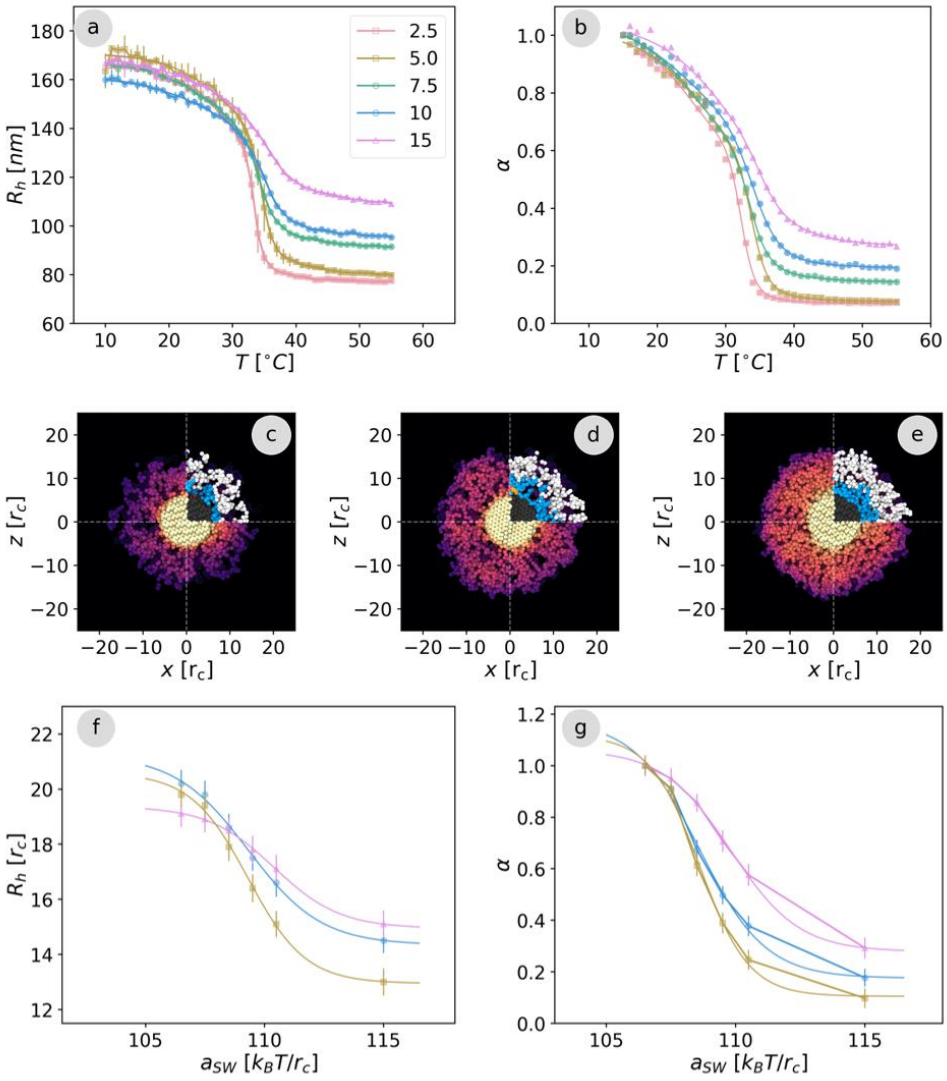

Figure 6. 3. Results from both temperature-dependent DLS measurements and corresponding simulations. (a). The hydrodynamic radius (R_h) is plotted as a function of T in the range between 10 °C to 55 °C. Error bars represent standard deviations from three independent measurements. (b). The de-swelling ratio, α, as a function of T. (c), (d) and (e) are snapshots of the simulated CS_5, CS_{10}, and CS_{15} microgels based on the DLS results, respectively, shown in the swollen state in bulk phase (side view, crosssections of the thickness of $4r_c$. Polymeric density is colour-coded using an inferno scheme, with orange signifying higher density and purple indicating lower density. The yellow sphere at the centre represents the hard silica core. Insets provide additional detail, recolouring the core, inner shell, and outer shell beads in black, blue, and white, respectively. (f) and (g) show computer simulation results of R_h and α presented as functions of the interaction parameter, α_{sw}.

To evaluate the swelling behaviour of the microgels in the simulation, temperature variations were introduced by modifying the interaction parameter (α_{sw}) between the shell (S) and water (W) beads. When the difference between the interaction parameter for the polymer-water (SW) and the polymer-polymer interaction (SS), $\Delta\alpha_{sw} = \alpha_{sw} - \alpha_{ss}$ is almost zero, the polymeric shell swells. In that case, polymer-water interactions are favoured. As the parameter $\Delta\alpha_{sw}$ increases, the repulsion between S and W beads becomes stronger, provoking the release of water from the microgel and the collapse of the shell. Hydrodynamic radii, R_h, and de-swelling ratios α of the simulated CS microgels as a function of α_{sw} are shown in **Figure 6. 3c-d.**

In the swollen state, the microgels have approximately the same hydrodynamic radius of approximately $R_{h,swollen} = 20r_c$ (**Figure 6. 3c)**. The ratio $R_{h,swollen}/R_{core}$ is 3.0 ± 0.1, 3.1 ± 0.1 and 2.9 ± 0.1 for CS_5, CS_{10} and $CS_{15,}$ respectively. These ratios coincide with the mean ratio found for the experimental samples (2.9 ± 0.1). Analyzing the swelling curves using a sigmoidal fit, the following interaction parameters at which the volume phase transition occurs were obtained: α_{sw}(VPT) = 109.3 ± 0.2 k_BT/r_c, 109.4 ± 0.1 k_BT/r_c, and 110.4 ± 0.1 k_BT/r_c for CS_5, CS_{10}, and $CS_{15,}$ respectively. Samples with a low cross-linking density reveal minimum swelling capacity (**Figure 6. 3d**). Microgels with 5, 10 and 15 % of cross-linker content achieve average values of maximum de-swelling ratios α around 0.097 ± 0.02, 0.177 ± 0.03, and 0.29258 ± 0.03, respectively. Not only is a similar tendency observed: $\alpha(CS_5) < \alpha(CS_{10}) < \alpha(CS_{15})$, but there is also a close correlation with the experimental values of 0.085, 0.183, and 0.257.

6.2 Compression isotherms of CS microgel monolayers

In order to study the phase behaviour of the CS microgels at air/water interfaces as a function of packing density, compression experiments were performed in a Langmuir–Blodgett trough. The experimentally determined surface pressure isotherms for the different CS microgels are shown in **Figure 6. 4**. The surface pressure is plotted against the number of microgels per unit area, ($N_p/Area$). N_p was estimated by counting microgels per area from AFM images obtained through *ex-situ* analysis, the calculation process is shown in the **Appendix** (Figure A. 4). It is worth noting that, at high compression states, the estimated N_p is higher than the value obtained directly from AFM images, which might attribute to the migration of microgels from interface to the bulk phase at the high compression state, so the higher compression regions (IV and V) of the isotherm undergo stretching along the x-axis. The raw data of the compression isotherms are shown in **Figure A. 5**. This also involved transferring microgel monolayers onto glass substrates at specified surface pressures, followed by drying at room temperature and subsequent imaging using AFM, i.e., *ex-situ* analysis. These analyses are based on the assumption that transferred monolayers exhibit similar characteristics to those at the air/water interface, a topic will later be discussed for its validity. Since it is very hard to know the exact number of microgels on the interface and their changes, the value of $N_p/Area$ here is only used as a reference. For the raw data of the compression isotherm, please refer to **Appendix A.5**. TEM and DLS results classify CS microgels into two groups: lower cross-linked $CS_{2.5}$ and CS_5 microgels lacking the inner shell structure and higher cross-linked $CS_{7.5}$, CS_{10}, and CS_{15} microgels with the inner shell. Notably, these differences also appear in their compression isotherms. The isotherms of monolayers of $CS_{2.5}$ and CS_5, go through a one-stage surface pressure increase and then reach a plateau at approximately 30 mN/m

and higher, see **Figure 6. 4a**. In contrast, the higher cross-linked microgels, $CS_{7.5}$-CS_{15} follow a two-step increase, see **Figure 6. 4b**.

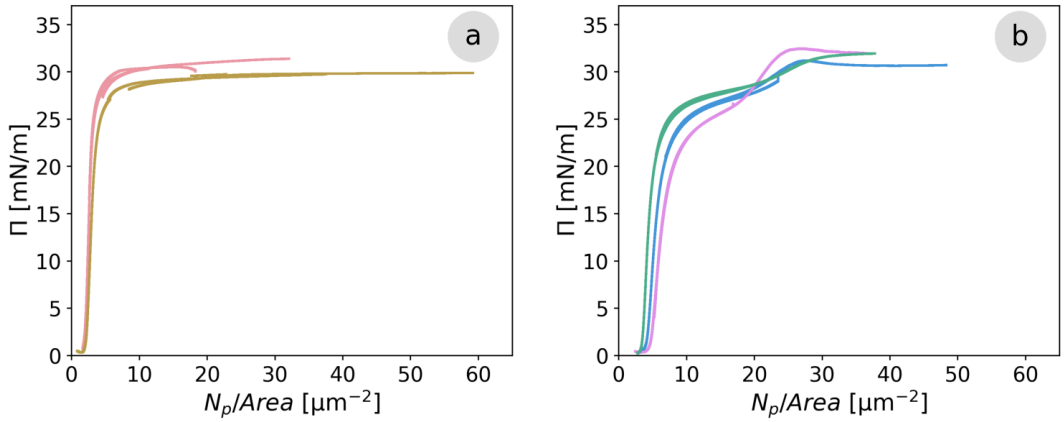

Figure 6. 4. Compression isotherms of loosely (a) and highly (b) cross-linked microgels at air/water interfaces. The surface pressure is plotted as a function of the number of microgels per unit area ($N_p/Area$).

According to the trend of isotherm variation, it can be roughly divided into states I-V, with the approximate ranges of surface pressures for each part provided in **Table 6. 2**. Compression state I begins with a low $N_p/Area$ and nearly 0 mN/m surface pressure, while compression state II shows a rapid increase in Π despite a slight increase in $N_p/Area$. A comparison between the samples shows that the surface pressure increases at higher $N_p/Area$ in the case of microgels with higher cross-linker content[203]. Then, the flattening of the surface pressure is referred to as compression state III. For $CS_{7.5}$, CS_{10}, and CS_{15} samples, it is reached at Π around 25 mN/m, 24 mN/m, and 23 mN/m, respectively. This is followed by the second increase in surface pressure, compression state IV, until reaching a final plateau, compression state V. The transition region between the first and second rises (compression state III) narrows with higher cross-linking density. Microgels with more cross-links start the second stage with a lower Π.

In compression state V, Π reaches maximum values of 31.9 mN/m, 31.2 mN/m, and 32.4 mN/m for $CS_{7.5}$, CS_{10}, and CS_{15}, respectively. In the case of $CS_{2.5}$ and $CS_{5,}$ compression states (III-V) become one. Π reaches a plateau at approximately 31 mN/m and 30 mN/m. The values are close to the maximum surface pressure measured for the linear PNIPAM using a pendant drop tensiometer (See **Figure 5. 12**).

Table 6. 2. The nearest $d_{c\text{-}c}$ distribution and related surface tension for each compression state (I-V).

	Π [mN/m]				**Nearest $d_{c\text{-}c}$ distribution [nm]**			
	I	II	III - IV	V	I	II	III - IV	V
$CS_{2.5}$	0.7 - 1.4	1.4 - 29.2		29.2 - 31.4	≥626	208 ~ 626		104
CS_5	0.4 - 0.7	0.7 - 28.3		28.3 - 29.8	≥652	261 ~ 652		104
$CS_{7.5}$	0.4 - 0.9	0.9 - 21.1	21.1 - 28.0	28.0 - 31.9	574 ~ 600	365 ~ 600	143 ~ 235	235
CS_{10}	0.6 – 1.0	1.0 - 20.8	20.8 - 27.6	27.6 - 31.2	548	391 ~ 496	157 ~ 235	209
CS_{15}	0.4 – 1.0	1.0 - 18.7	18.7 - 26.5	26.5 - 32.4	470	444 ~ 470	209 ~ 235	209

6.3 Microstructure of transferred CS microgel monolayers

The surface pressure isotherms are correlated to the internal microgel structure and the microstructure of the resulting monolayers. Hence, an *ex-situ* morphological analysis of the monolayers was conducted after transfer from the air/water interface to glass substrates. AFM imaging of dried monolayers was used to examine the arrangement and symmetry of the microgel monolayer at different compression states.

The AFM height images of the monolayers transferred to hydrophilic glass substrates at different compression states are shown in **Figure 6. 5**. The focus was on studying

morphological changes during compression in low cross-linked CS_5 microgels and higher cross-linked CS_{10} and CS_{15} microgels.

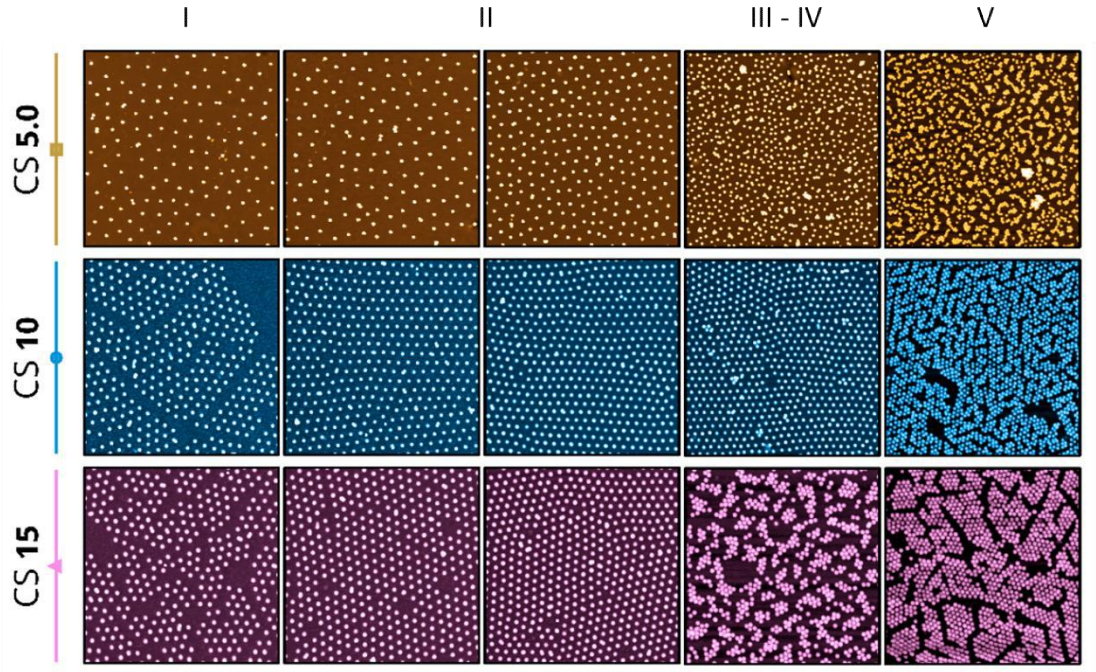

Figure 6. 5. AFM height images of CS_5, CS_{10} and CS_{15} monolayers deposited to hydrophilic glass substrates at varying surface pressures reveal distinct compression states. The colour scheme corresponds to the colours of the curves in the compression isotherms: ochre, blue, and pink. The scales of the images are 10 ×10 μm^2.

In compression state I, where Π is nearly 0 mN/m, there are pronounced differences between the samples in **Figure 6. 5** (first column). The distribution of the CS_5 microgels is more or less random, referred to as an isotropic liquid-like phase, with the transferred microgels non-contact with each other. In contrast, the higher cross-linked CS_{10} and CS_{15} microgels formed local non-close packed hexagonal aggregates separated by the voids. This behaviour might be attributed to attractive capillary forces at the interface, driving the CS microgels together into clusters at a defined inter-particle distance[52]. As the surface pressure increases, the voids between the clusters vanish at the beginning of compression state II. Meanwhile the microgels formed a loosely-

packed hexagonal lattice (see the second column of **Figure 6. 5**). During state II compression, the nearest $d_{c\text{-}c}$ gradually and uniformly decreased. In compression states III - IV, some of the CS_{10} and CS_{15} microgels underwent a sudden transition to a close-packed hexagonal lattice with dramatically smaller $d_{c\text{-}c}$ values, while others in the monolayer maintained the loosely-packed hexagonal lattice configuration. This phenomenon is typically described in the literature as a solid-solid isostructural phase transition[90]. Notably, the low-cross-linked CS_5 microgels started “aggregation” at the end of State II. Compared to the "close-packed hexagonal lattice" observed in CS_{10} and CS_{15}, the “aggregation” of the CS_5 monolayer is less ordered. Finally, at higher surface pressures (state V), all the microgels transitioned to the close-packed hexagonal lattice or “aggregations”. Remarkably, the monolayer is not uniform and shows voids between the clusters.

Figure 6. 6 depicts AFM images of transferred CS microgels monolayers obtained at Π = 25.8 ± 0.2 mN/m. The compression isotherms show a rightward shift with increasing cross-linker density in CS microgels, signifying a larger $N_p/Area$ to attain equivalent surface pressure. This fact can be attributed to changes in the nearest $d_{c\text{-}c}$ and the morphological transitions. Indeed, $CS_{2.5}$ microgels form a monolayer with an average nearest $d_{c\text{-}c}$ of 521 nm, lacking long-range order. In contrast, CS_5 microgel monolayers exhibit a loosely-packed hexagonal lattice with an average nearest $d_{c\text{-}c}$ of 483 nm. $CS_{7.5}$ microgels are beginning the solid-solid isostructure transition from a loosely-packed hexagonal lattice to a close-packed hexagonal lattice (average nearest $d_{c\text{-}c}$ of 365 nm). At the same time, the CS_{10} monolayer is in an intermediate state, with part of the microgels forming close-packed clusters, while CS_{15} microgels completed the transition and assembled into a close-packed hexagonal lattice with the nearest $d_{c\text{-}c}$ = 234 nm.

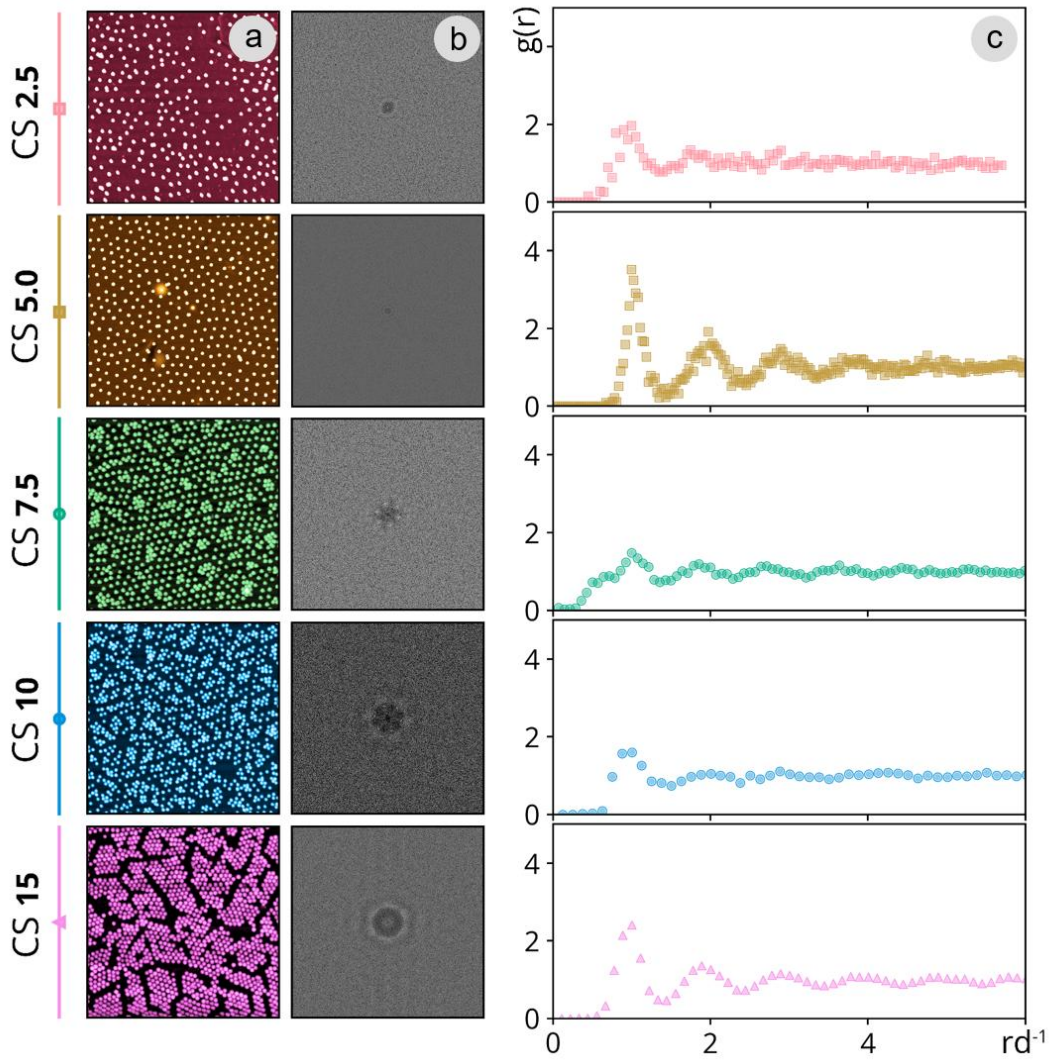

Figure 6. 6. AFM images (a), corresponding Fast Fourier Transformations (b) and corresponding representative average 2D radial distribution functions *g(r)*, normalized by the position of the first maximum (c) for the monolayer of $CS_{2.5}$, CS_5, $CS_{7.5}$, CS_{10} and CS_{15} microgels deposited to glass substrates at 25.8 ± 0.2 mN/m.

To explore the relationships between the compression behaviour and monolayer morphology, the change of the nearest $d_{c\text{-}c}$ was plotted over $N_p/Area$ (**Figure 6. 7a**). It is worth noting that the $N_p/Area$ obtained here, which is derived from the first peak of the $g(r)$ functions computed from AFM images, is lower in high compression states compared to the estimated $N_p/Area$ used to plot the compression isotherms. The variation of the nearest $d_{c\text{-}c}$ over $N_p/Area$ was also superimposed on the distribution of the

inner shell diameter of (d_i) those measured from TEM images. In the case of the $CS_{2.5}$ and CS_5 microgels, d_i represents the inside diameter of the fuzzy shell. The distribution of $d_{c\text{-}c}$ splits into two distinguishable groups of points. Points on the right-hand side refer to the loosely packed hexagonal structure in the monolayer at compression states I and II, while those on the left relate to the close-packed hexagonal structure observed in compression states III-V. The gaps between these groups widen with increasing cross-linker density of the microgels. For the points on the right-hand side, all the samples demonstrate a continuous decrease of $d_{c\text{-}c}$ as $N_p/Area$ increased. It indicates the reduction of microgel-free voids in the monolayer and the gradual shrinkage of the microgels induced by the deformation of their outer fuzzy shells. For points on the left-hand side, $N_p/Area$ increases while the $d_{c\text{-}c}$ undergoes minimal change. The $d_{c\text{-}c}$ values closely match the diameter of the inner shell, d_i (**Figure 6. 7b**). In the case of the $CS_{2.5}$ and CS_5 microgels, values of $d_{c\text{-}c}$ in the left segments approach 104 nm, closely matching the average diameter of the silica cores (105 ± 3 nm). This result highlights three important observations: firstly, the microgels started the "solid-solid isostructural transition" or "aggregation" before the complete collapsing of the outer fuzzy shell, resulting in the voids between the clusters and the gaps in the $d_{c\text{-}c}$ distributions; secondly, after this transition, the outer fuzzy shell is likely to be entirely collapsed, as indicated by $d_{c\text{-}c}$ values closely approaching the values of d_i or d_{core}; thirdly, the narrow distributions of $d_{c\text{-}c}$ indicate limited compressibility of the microgels, confirming the high cross-linker density of the inner shell.

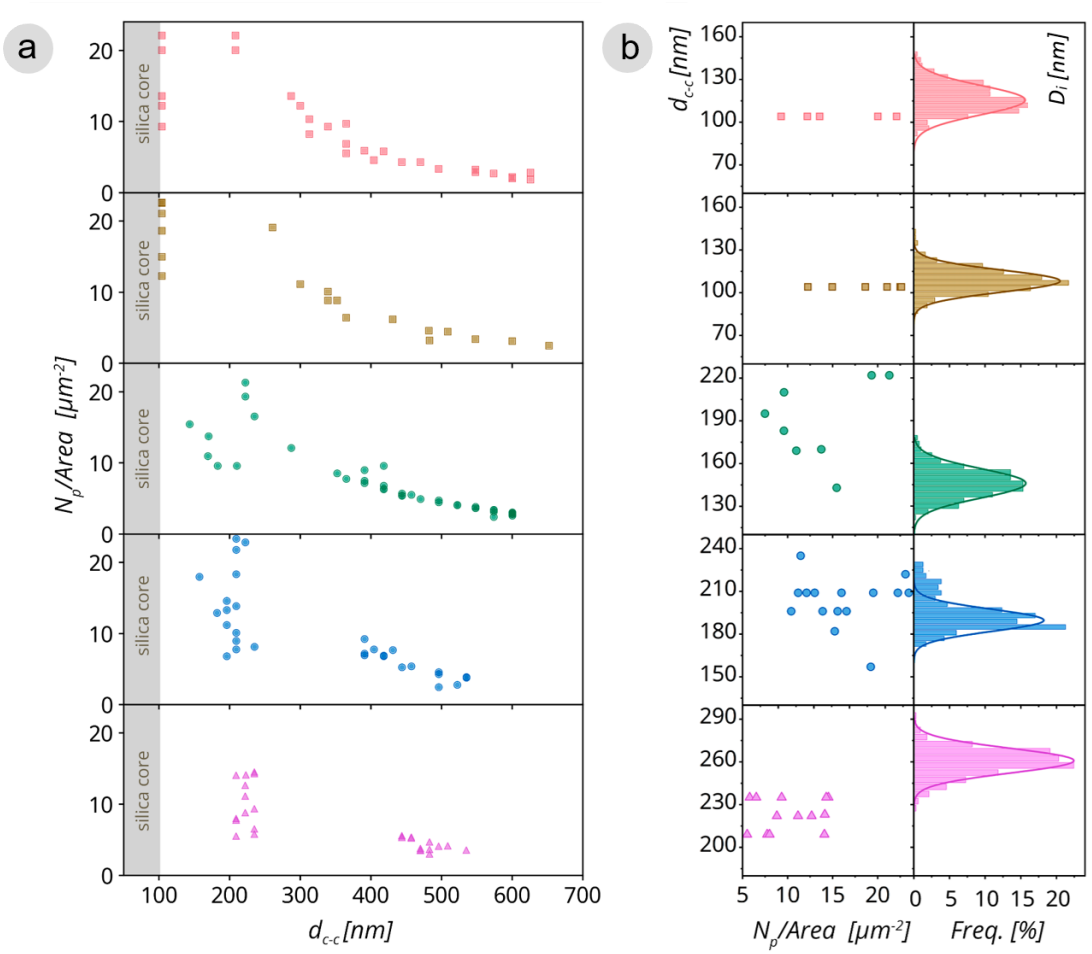

Figure 6. 7. (a). Evolution of inter-particle distance $d_{c\text{-}c}$ for increasing microgel packing densities (N_p/Area). Values of $d_{c\text{-}c}$ were obtained from the first peak of the *g(r)* functions computed from AFM images. The grey-shaded area on the left corresponds to the size of the silica core. (b). The evolution of $d_{c\text{-}c}$ in a selected range of packing densities and the distribution of the inner diameter that calculated from TEM images. The inner shell size histogram (diagrams on the very right) was fitted with Gaussian distribution. Red, ochre, green, blue, and pink colours correspond to the $CS_{2.5}$, CS_5, $CS_{7.5}$, CS_{10} and CS_{15} microgels.

6.4 Simulated CS microgel monolayers at air/water interfaces

Snapshots of individual CS_5, CS_{10} and CS_{15} microgels in uncompressed state adsorbed from the bulk to the air/water interface at $N_p/Area = 1.5\ r_c^{-2}$ after equilibration are shown in **Figure 6. 8.** Microgel networks undergo lateral deformation during adsorption, expanding to minimize interfacial free energy until internal elasticity offsets the energetic gain. Compared to the more cross-linked central part, the flexibility of

peripheral dangling chains results in a kind of "fried egg" morphology, as observed in techniques like cryo-scanning electron microscopy (cryo-SEM)[52, 204].

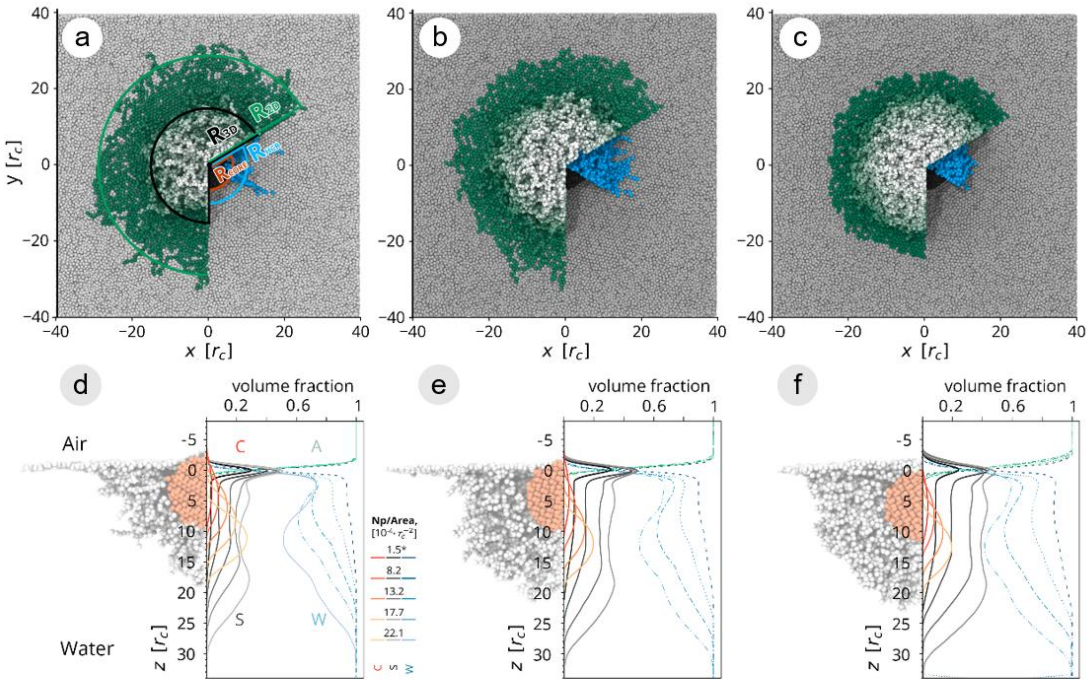

Figure 6. 8. Snapshots of CS_5, CS_{10}, and CS_{15} microgels at the air/water interface. (a-c). Snapshots of the top view. The height profile is colour-coded using a green-white gradient, with green denoting beads near the interface; (d-e). Side-view cross-sections with a thickness of $4r_c$ through the microgel's center of mass, along with volume fraction profiles along the z-axis (normal to the air/water interface) for microgel monolayers. Grey, orange, blue, and green curves represent fractions of S (shell), C(core), W(water) and A(air) beads, respectively. Gradient colour scheme and line styles (dashed to dotted) indicate the cases low, $N_p/Area$ 1.5*, 8.2, medium, 13.2 and high, 17.7 [$\cdot 10^{-4} r_c^{-2}$], compressions, respectively. * indicate the case of the single microgel at the interface. R_{2D}, R_{3D}, R_{HCR} denote the radii of the contact areas of various parts of the microgels at the interface when z=0.

Three distinct parts within the microgels are recognized: (1) The region where the microgel extends into the air, defined by the protrusion height, h_{air}; (2) A thin 2D polymeric layer adsorbed at the interface, referred to as the corona, with a characteristic size R_{2D}; (3) The 3D bulky swollen part of the microgel extends into the aqueous phase, characterized by the protrusion height h_{water} and size R_{3D}. Specifically, R_{2D}, R_{3D}, R_{HCR} represent the radii of contact areas of different parts of microgels at the interface

(Z = 0). R_{2D} is the radius of the peripheral adsorbed part of the microgel, R_{3D} is the radius of the swollen part of the microgels extending into the aqueous phase, while R_{HCR} represents the radius of the contact spot for the inner shell of the microgels. The dimensions of the samples are summarized in **Table 6. 3**.

Table 6. 3. Dimensions of single microgels at the air/water interface in an uncompressed state.

	h_{air} [r_c]	h_{water} [r_c]	R_{2D} [r_c]	R_{HCR} [r_c]	R_{3D} [r_c]
CS_5	1.5 ± 0.2	14.9 ± 0.1	32.7 ± 0.3	14.2 ± 0.1	16.2 ± 0.3
CS_{10}	1.7 ± 0.2	17.6 ± 0.1	31.7 ± 0.3	16.6 ± 0.1	21.2 ± 0.1
CS_{15}	2.0 ± 0.1	19.6 ± 0.1	27.6 ± 0.2	12.4 ± 0.1	20.4 ± 0.1

* R_{2D}, R_{3D}, R_{HCR} have been determined by the analysis of the radial density distribution functions within a lateral slice of the microgels with a thickness of $h = 4r_c$.

** h_{water} and h_{air} were determined by the analysis of the density distribution functions of the polymer in the normal direction to the interface, see **Figure 6. 8d-f**.

CS_5 has the smallest 3D part and the largest 2D part. The low average cross-link density in the microgel shell encourages extensive lateral deformation, maximizing interface coverage. Despite significant lateral deformation, the presence of the solid core may also limit the subchain deformation. It is also possible that covalent bonds between the core and shell induce an effective force, which could push the solid core into the air phase and deform the interface. The area of microgel protrusion into the air phase is relatively small. The higher cross-linked microgels CS_{10} and CS_{15} exhibit a decreased adsorbed polymeric layer size while displaying an enlarged swollen part in water. The highly cross-linked inner part surrounding the solid core restricts the lateral stretching of the outer periphery of the microgels. At the same time, the relative position of the solid core shifts towards the water phase. The protrusion and de-

formation of the interface increase, leading to attractive capillary inter-particle interactions observed in experiments with low surface coverage.

The significant difference between the structure of the 3D part and the 2D part of the microgel is worth noting. The 3D part resembles the microgel structure away from the interface, featuring a fuzzy double-shell polymeric network with subchains in a swollen state. In contrast, the 2D part exhibits condensed chains forming a dense, almost monomolecular film. The polymer volume fraction of the system (the dimensionless concentration) is plotted as a function of distance from the interface, z, measured in r_c units, see **Figure 6. 8** ($N_p/Area$ = 1.5*)**.** It displays a sharp peak of shell beads near the interfacial boundary, gradually decreasing with distance far away. In the contact region beneath the 3D part, a portion of the 2D layer is formed by subchains from both the outer and inner shells. Beyond the 3D part, the 2D layer consists of outer shell subchains only, see **Figure 6. 8 (a-c)**. The divergence in the compression response of 2D and 3D parts would affect the monolayer behaviour.

Next, ensembles of CS microgels at the air/water interface were compressed (see **Appendix A.7** and **A.8**). The surface pressures of the microgel monolayers as a function of $N_p/Area$ are plotted in **Figure 6. 9a**. Similar to the experiment, the isotherms of monolayers of loosely cross-linked microgels, $CS_{5,}$ go through a one-stage surface pressure increase. In contrast, highly cross-linked microgels, CS_{10} and CS_{15} follow a two-step increase.

Let us follow the terminology of compression states I to V discussed in the experimental section. **Figure 6. 9d** provides an overview of the interfacial microstructures formed in $CS_{5,}$ CS_{10} and CS_{15} microgel monolayers at different compression states. The monolayer morphology was analyzed by measuring the evolution of the nearest

$d_{c\text{-}c}$ (**Figure 6. 9a**) and the hexagonal order parameter Ψ_6 (**Figure 6. 9c**) based on the central positions of the solid cores of the CS microgels (**Figure 6. 9d** first row, **Figure A. 11**, **Figure A. 13)**.

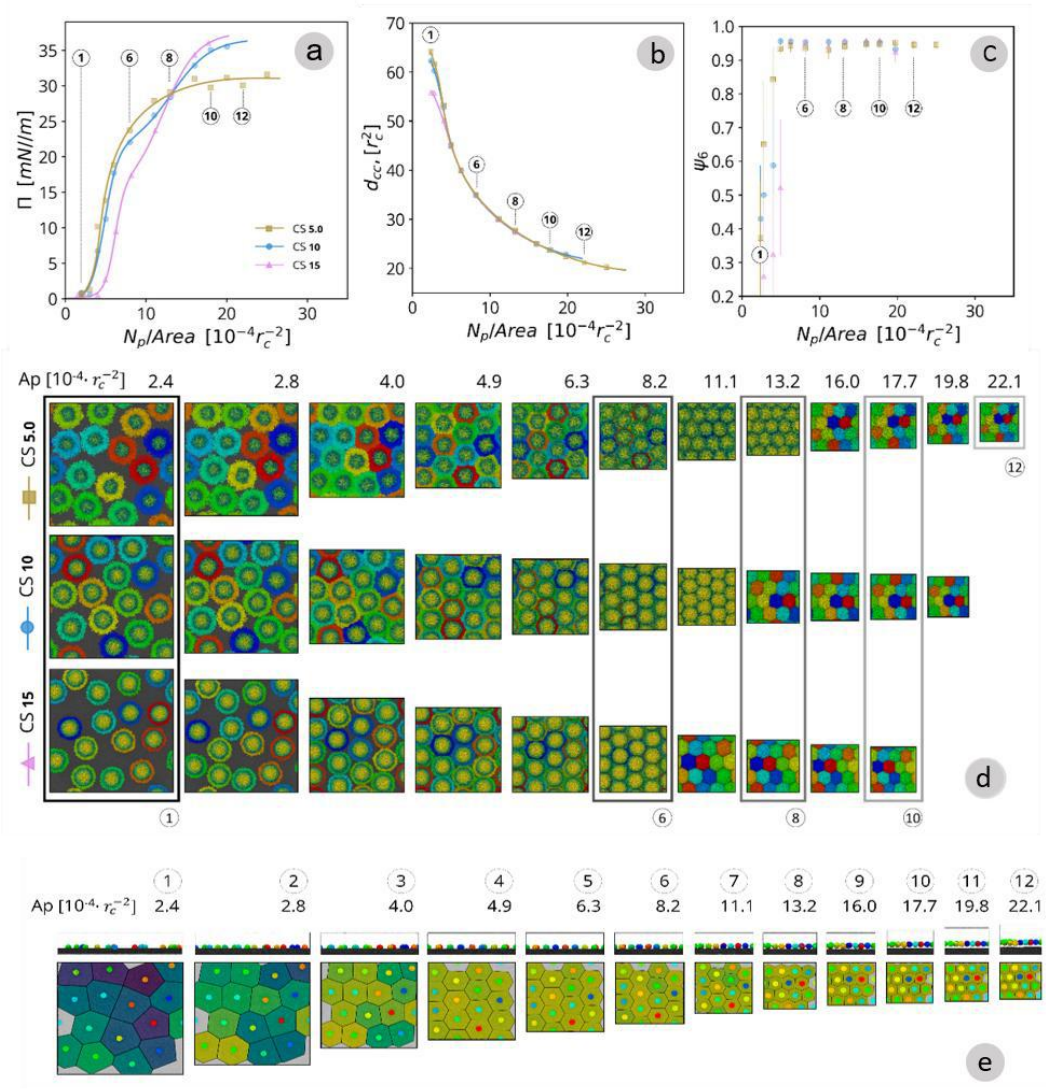

Figure 6. 9. Simulated microgel interfacial behaviours. (a). Simulated compression isotherms of microgels; (b) and (c) are nearest $d_{c\text{-}c}$ and the hexagonal bond-order parameter $\Psi 6$ (equation A. 6) plotted as functions of $N_p/Area$. Values of minimum $d_{c\text{-}c}$ were obtained by Gaussian fits of the first peak of the computed $g(r)$ functions; (d). The first row is the side and top view (from the water phase) of the position of the cores of the CS_5 monolayers. Water and polymeric beads are not shown. For clarity, the cores of different microgels are marked by rainbow colours. Snapshots are combined with the Voronoi diagram, where each Voronoi cell is coloured by the value of the local orientational order parameter corresponding to the relevant cell, $|\psi_6^k(r_k)|$, see **Appendix** equation (A.6). The darker the colour the closer the $|\psi_6^k(r_k)|$ to 0. The second and third rows are the snapshots of CS_{10} and CS_{15} microgel monolayers at different compression degrees. Waterside view, with the 2D "corona" area marked by rainbow colours and the water-swollen 3D part shown in a green-to-yellow gradient. After full compression of the "corona," all microgels are marked by rainbow colours.

In compression state I (regime of low Π at $N_p/Area < 2.4$ [$10^{-4} r_c^{-2}$]), the CS_5 microgels are randomly distributed through the interface (**Figure 6. 9**), similar to the experimental observations. An increase in number density is accompanied by a decrease of $d_{c\text{-}c}$ (**Figure 6. 9b)**. In the case of CS_{15} microgels with a highly cross-linked shell, the formation of small aggregates at the interface is observed. In support of this, the nearest $d_{c\text{-}c}$ remains nearly constant at $N_p/Area < 2.8$ [$10^{-4} r_c^{-2}$]. Computed $g(r)$ functions reveal a wide distribution of distances between microgels, indicating cluster formation likely induced by the protrusion of microgels into the air phase, reducing interface curvature. AFM images show non-close-packed hexagonal lattices interspersed with microgel-free voids on a glass substrate. Nevertheless, simulations do not directly indicate the presence of strong, attractive forces at the air/water interface. This discrepancy may stem from finite-size constraints in microgel modelling or underscore the impact of substrate and drying procedures on monolayer ordering in experiments.

In the compression state II (the first Π rise), where $N_p/Area$ (CS_5) ~ (2.8-4) [$10^{-4} r_c^{-2}$] and $N_p/Area$ (CS_{10}, CS_{15}) ~ (3.0-4.5) [$10^{-4} r_c^{-2}$] the microgels tend to form a regular, space-filling hexagonal lattice. The hexagonal bond-order parameter Ψ_6 (equation A.5) rises (**Figure 6. 9b**). A continuous reduction of void space is observed with an increasing number of "corona-corona" contacts. Consistent with experimental observations, CS_{10} and CS_{15} exhibit an increase in surface pressure at a higher $N_p/Area$ (**Figure 6. 4a**), which is related to the different lateral dimensions of the microgels at the interface. Microgels with higher cross-linker content exhibit less deformation at the interface, resulting in a smaller area per microgel compared to lower cross-linked CS microgels. The voids between the microgels gradually disappear and the CS microgels fully occupy the interface. In the range between $N_p/Area$ ~ (4.9-8.2) [$10^{-4} r_c^{-2}$], the

morphology of the monolayers of CS_5 to CS_{15} becomes a close-packed hexagonal lattice where Ψ_6 reaches a maximum value.

Upon further compression, the surface pressure of the CS_5 sample reaches a plateau, remaining unchanged until the buckling and breaking of the interface. In contrast, the surface pressures of the CS_{10} and CS_{15} monolayers proceed to the second increase. Despite similar shapes of the isotherms depicted in **Figure 6. 4** and **Figure 6. 9**, the behaviour and the morphology of the monolayer at the water/air interface at compression states III-V reveal notable disparities from experimental findings observed in AFM. Firstly, the simulation brings out the complete surface coverage of the microgels at each compression stage (**Figure 6. 9d)**. Secondly, the microstructure of the monolayers is the close-packed hexagonal lattice, where the mutual distance between the individual microgels constantly decreases as a function of the total available surface area (**Figure 6. 9c)**. Furthermore, the solid-solid isostructural transition and nearest $d_{c\text{-}c}$ is monotonically decreasing were not observed (**Figure 6. 9b)**. So, what is the origin of the second surface pressure increase out of the simulations observed for higher cross-linked CS microgels? What is the physics behind the evolution of the monolayer of CS microgels?

To address this, structural changes and deformations within individual microgels are tracked and correlated with the monolayer's compression isotherms and morphological transformations at different surface pressures. The concentration profiles in normal (**Figure 6. 8**) and lateral (**Figure 6. 10a, d**) directions to the interface allow us to monitor the microgels' size and shape transformation, including the microgels' protrusion into the air phase as a function of $N_p/Area$. In addition, the forces acting on the selected microgels from their nearest neighbours were calculated to characterize the

interaction between microgels at different degrees of compression precisely (**Figure 6. 10b, c, e, f**).

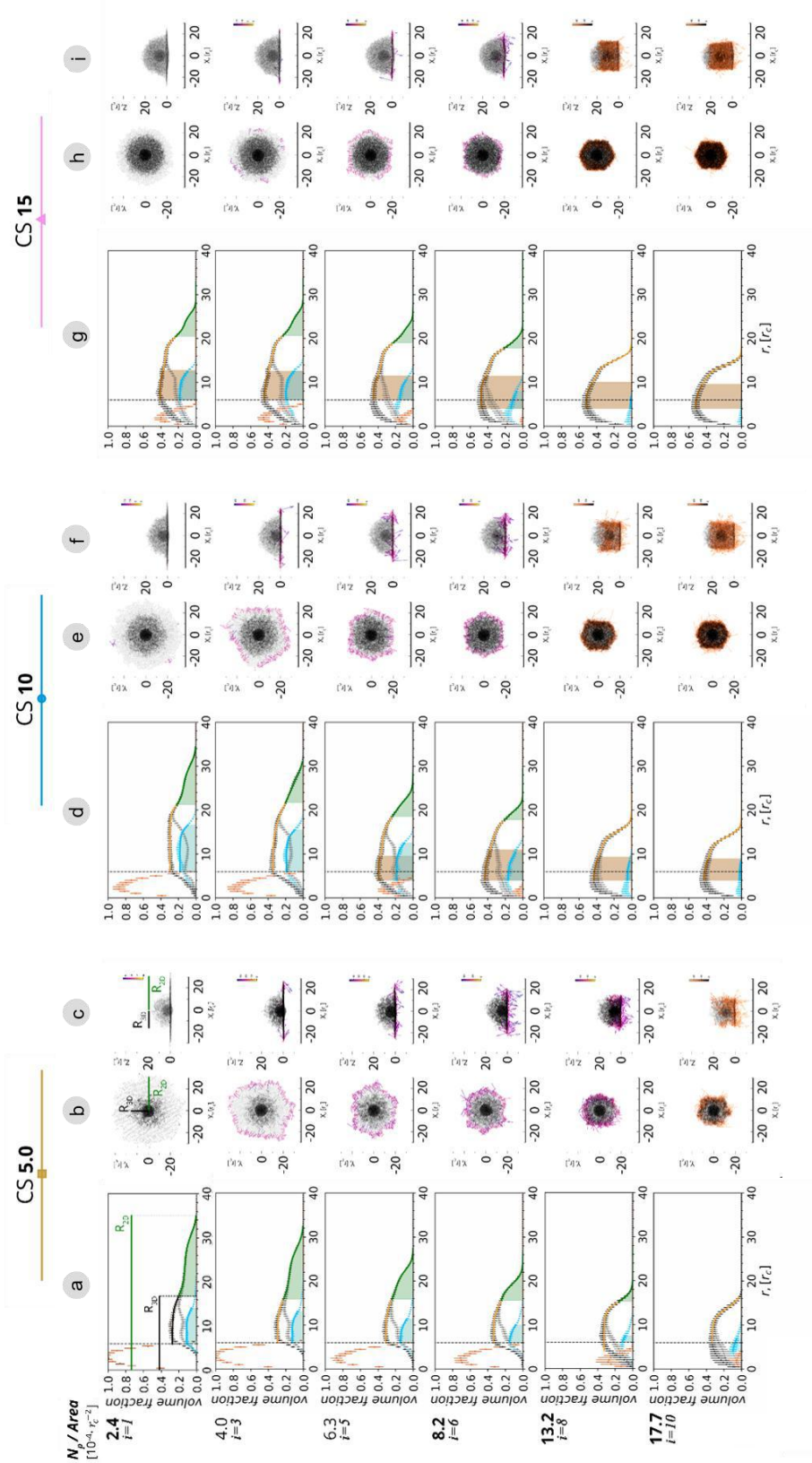

Figure 6. 10. Relative monomer density profiles in lateral slices of the CS_5 (a), CS_{10} (d) and CS_{15}(g) microgels at the air/water interface at different $N_p/Area$ values. The slices were made in the lateral direction of the interface. The thickness of the slices is equal to $4r_c$. The vertical dotted line indicates the size of the solid core. (b, c), (e, f) and (h, i) show the averaged forces that act on single CS_5, CS_{10} and CS_{15} microgels from the surrounding microgels at the interface for different $N_p/Area$, respectively. Black dots correspond to the polymeric and solid core beads. Pink (plasma colour scheme) arrows are the forces coming from the corona-corona interactions, while brown (copper colour scheme) arrows are the forces coming from the kernel-kernel interactions. View in XY (b, e, h) and XZ (c, f, i) directions are shown, where Z is the direction perpendicular to the air/water interface.

At low $N_p/Area$ all microgels maintain their size at the interface and remain unaltered. Interactions are limited to isolated contacts between 2D corona parts of neighbouring microgels in small aggregates (**Figure 6. 9, Figure 6. 10,** $N_p/Area$ = 2.4 [$10^{-4}r_c^{-2}$]**)**. This area is classified as state I. Further increase of $N_p/Area$ up to ~ 6.3 [$10^{-4}r_c^{-2}$] is accompanied by the formation of multiple spatial corona-corona contacts, namely state II. The 3D part of the microgels undergoes minimal changes, while the $d_{c\text{-}c}$ decreases due to filling gaps between coronas and gradually reducing the corona size, causing an increase in surface pressure. Compression of the monolayers increases the polymeric volume fraction at the interface, as indicated by the rising peak (**Figure 6. 8d-f**). At $N_p/Area$ = 6.3 [$10^{-4}r_c^{-2}$], near the first plateau in the compression isotherm, the formation of a close-packed hexagonal lattice is observed. Upon further compression $N_p/Area$ (CS_5) ~ (8.2-13.2) [$10^{-4}r_c^{-2}$] and $N_p/Area$ (CS_{15}) ~ (6.3-8.2) [$10^{-4}r_c^{-2}$], state III, the polymer corona is tended to be compelled beneath the core, leading to notable changes. Firstly, the Z position of the solid core shifts deeper into the aqueous phase (see **Figure A. 9, Figure A. 10, Figure A. 11, Figure A. 13**). Additionally, increased compression diminishes the microgel's protrusion into the air phase while enlarging its normal size toward the aqueous phase. The plateau observed in state III is ascribed to self-similar deformation and significant compression of the microgel corona. State III is minimal for CS_{15} and maximal for CS_5 due to varying 2D corona widths. The isotherm shape of loosely cross-linked microgels closely resembles that

of linear PNIPAM, yet it is distinctly shifted to a large $N_p/Area$ values (**Figure 6. 4** and **Figure A. 8**). The same observation was discussed in Ref. [205], where the behaviour of PNIPAM linear chains, stars, and microgels was compared.

Stage IV occurs when the 3D parts of the microgels begin to come into direct contact with each other, $N_p/Area$ (CS_5) = 17.7 [$10^{-4}r_c^{-2}$], $N_p/Area$ (CS_{15}) = 13.2 [$10^{-4}r_c^{-2}$]. From now the 2D interaction of microgels due to corona-corona contacts evolves into the 3D interaction of the entire microgels (**Figure 6. 10**). The fuzzy outer shells of the microgels undergo interpenetration and deformation, leading to a slight reduction in the degree of monolayer order (**Figure 6. 10c).** Remarkably, the peak of the polymer density near the interface, as depicted in concentration profiles along the z-axis (**Figure 6. 8d-f**) reaches and maintains its maximum value. Notably, the maximum peak value remains relatively consistent across different CS microgel types, thus determined by the chemistry of the subchains rather than the peculiarities of the shell structure.

The second rise of the CS_{10} and CS_{15} compression curves directly relates to the shell's prominent highly cross-linked double-layer structure. The polymeric density of the low cross-linked microgels does not significantly impact the rise in pressure. At that stage, the density of the entire kernel rises (**Figure 6. 9b-c**). The solid cores continue to shift into the aqueous phase, coupled with enlarging the normal size of the microgel in the Z direction. As the solid core moves away from the interface, redistribution of polymer density occurs. R_{HCR} decreases, indicating that the inner shell with a high degree of cross-linking spreading near the interface is gradually replaced by a fuzzy outer shell, see **Figure 6. 10** blue lines. At the same time, the overall polymeric density of the inner region in the lateral slices near the interface rises. Upon further com-

pression, the order degree of the monolayer is restored**.** A second close-packed hexagonal phase emerges, characterized by a shorter inter-particle distance due to kernel interactions.

In state V, the monolayer experiences collapse. Notably, failure is observed for CS_{10} and CS_{15} microgels, occurring at interparticle distances akin to the hydrodynamic size in their collapsed state in bulk (**Figure A. 9**, **Figure A. 10**). Shortly before, an order disturbance arises, leading to the displacement of specific microgels among each other (**Figure A. 11**, **Figure A. 13**).

This finding can be elucidated further by plotting the *Π* and longitudinal dimensions as a function of $N_p/Area$ (**Figure 6. 11**). Initially, as the surface pressure increases, there is a gradual decrease in the corona size of the microgel, R_{2D}, with slight deformation of the 3D part, R_{3D}. The convergence of these curves indicates the disappearance of the corona and corresponds to the pseudo plateau region of the isotherm. Subsequent increases in the isotherm coincide with a reduction in the R_{3D} due to the successive collapse of the outer and inner shells.

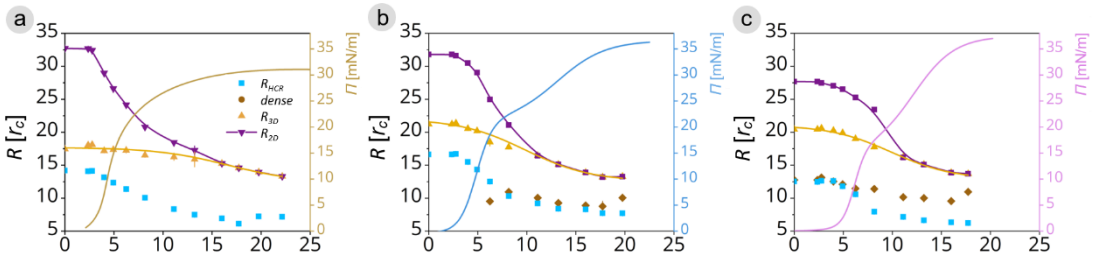

Figure 6. 11. Radii of the highly cross-linked inner part (blue), R_{HCR}, the 3D part (yellow), R_{3D}, and the 2D part (purple), R_{2D} of (a) CS_5, (b) CS_{10} and (c) CS_{15} microgels adsorbed at the air/water interface at different states of compression. The ochre (a), blue (b) and pink (c) curves are the compression isotherms.

6.5 Influence of hydrophobicity of the substrates

Although there was a strong correlation between the experimentally measured and simulated compression isotherms for various CS systems, several fundamental discrepancies between the experimental and modelling results were identified. In particular, the solid-solid isostructural phase transition was exclusively observed in *ex-situ* analysis post-transfer of CS_{10} and CS_{15} microgel monolayers onto hydrophilic substrates, providing the abrupt change in $d_{c\text{-}c}$. Simulations, however, demonstrate a continuous decrease in $d_{c\text{-}c}$ with increasing compression, lacking evidence for a phase transition. So, who is right? What is the origin of the solid-solid isostructural phase transition observed in *ex-situ* analysis? Is the equilibrium structure of monolayers at the interface identical to the ones transferred to the substrates?

Recently, Kuk *et al.* compared the microstructure of CS microgels at the air/water interface (*in-situ*) with the structure obtained after transfer to solid substrates and *ex-situ* microstructural analysis[59]. This work combined monolayer compression in a Langmuir trough with *in-situ* analysis using small-angle light scattering (LT-SALS), which revealed a continuous decrease in $d_{c\text{-}c}$ during compression, contrasting with *ex-situ* observations of discontinuous $d_{c\text{-}c}$ decrease and a solid-solid isostructural phase transition of microgels on hydrophilic substrates. This finding highlights the complex interplay between microgel adhesion to the solid substrates, influenced by surface energy and capillary interactions during drying of the monolayer of microgels that emerges during transfer from the air/water interface to the solid substrates. Surface modifications on glass substrates further showed varying microgel interactions[92, 206]. When microgels were deposited on PEG-ylated hydrophilic surface (hydrophilic, contact angle of 27°), they appeared in their native, spherical shape, revealing low surface-μG interactions. Both the substrate and the microgel are solvent-like systems.

On the other hand, ODS-modified surfaces (hydrophobic, contact angle 102°) allowed microgels to spread extensively due to strong substrate adsorption, minimizing surface-water interactions. The cross-linking density of the microgels (elasticity of the network) also plays a role in the degree of spreading on the substrate.

So, is the hydrophobicity of the substrates the reason for the difference between the simulation and experimental results? Then hydrophilic glass substrates (contact angle smaller than 5°) and hydrophobic MPS-modified glass substrates (contact angle between 85-100° were prepared to make a comparison. Monolayers were transferred at the states before, during and after the "isostructural phase transition" or "aggregation" observed on the hydrophilic glass substrates.

The raw AFM images from different compression states combined with the cluster analysis are presented in **Figure 6. 12**. 2D Voronoi tessellations were generated, and the average hexagonal bond orientation order parameter of the monolayers was counted **(Figure 6. 12**, **CS_{10})**. If a neighboring microgel is found within radii r_c = 150, 220 and 300 nm (for CS_5, CS_{10}, and CS_{15} monolayers, respectively), then two microgels are considered to belong to the same cluster. Microgels from the same cluster and the clusters with the same N_p were coloured the same way. The distribution of $N_{cluster}$ versus N_p/cluster is shown in **Figure A. 8**.

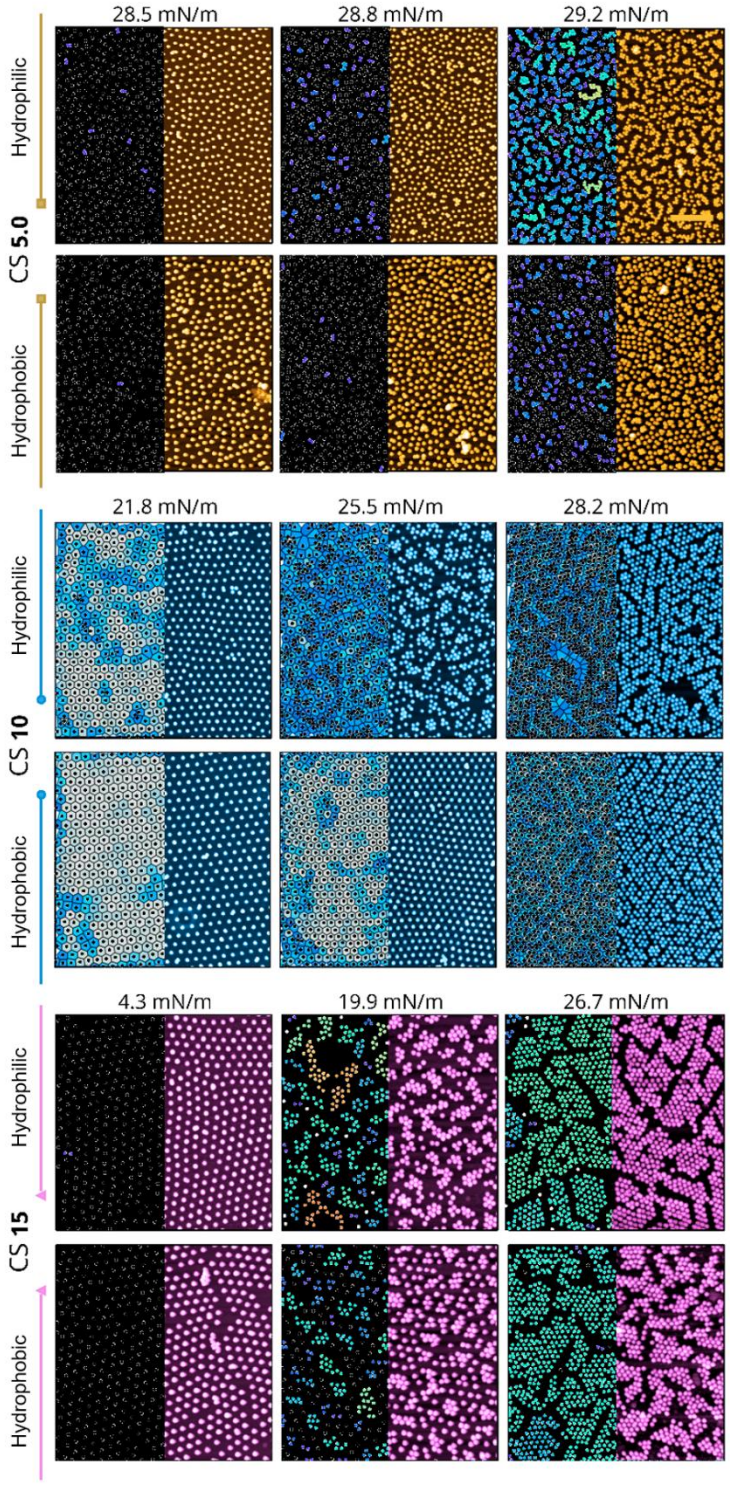

Figure 6. 12. AFM height images and related cluster analysis of CS_5, CS_{10}, and CS_{15} monolayers deposited onto hydrophilic and hydrophobic glass substrates. The left parts of the raw AFM images are treated by the cluster analysis of the microstructures (CS_5 and CS_{15} samples) and with the Voronoi diagram (CS_{10} samples), where each Voronoi cell is coloured by the value of the local orientational order parameter corresponding to the relevant cell, $|\psi_6^k(r_k)|$, see equation A.6. The darker the colour, the closer the $|\psi_6^k(r_k)|$ to 0. The size of the AFM images is 10 µm × 10 µm.

Before the isostructure phase transition, generally there's no large cluster observed in both hydrophilic and hydrophobic substrates (**Figure 6. 12**, Π = 28.5, 21.8 and 4.3 mN/m). The monolayers transferred to hydrophobic substrates present more homogeneous morphologies and show higher degrees of hexagonal order, especially in the case of the CS_{10} microgels **(Figure A. 17**). For the monolayers transferred during the isostructure phase transition (Π = 28.8, 25.5 and 19.9 mN/m), the microgels clustered on hydrophilic substrates with Ψ_6 parameters decrease to ~0.45. In contrast, microgels on hydrophobic substrates formed monolayers with higher Ψ_6 parameters and smaller clusters. Especially for CS_{10} microgels, a uniform hexagonal lattice with Ψ_6 parameter of 0.8 was observed. The nearest $d_{c\text{-}c}$ was approximately 365 nm, significantly larger than the value measured on hydrophilic glass substrates (~209 nm). This means the microgels are more likely to retain in a homogeneous distribution than to transfer into clusters.

When the isostructural phase transition is complete, CS_5, CS_{10} and CS_{15} microgels form close-packed clusters on both kind of substrates, with smaller clusters on hydrophobic substrates. For CS_{10} monolayers, $d_{c\text{-}c}$ values increased to 248 nm, compared to 209 nm on the hydrophilic glass. However, the homogeneity improvement of the CS_{15} monolayers was less significant, likely due to their rigidity hindering effective contacts with the substrates during transfer and drying of the thin liquid film, reducing the adhesion to the substrate, as observed in our previous work[59].

The simulation results are more consistent with the monolayers transferred to hydrophobic glass substrates, both showing a more homogeneous distribution of the microgels. This could be due to the hydrophobic substrate having a stronger affinity for the microgels than water, facilitating their adhesion to the substrate. Thus, during

transfer and drying, microgels may exhibit reduced lateral mobility on hydrophobic substrates, hindering their assembly or reassembly upon drying. Potential driving forces include capillary forces at the substrate, inhomogeneities in polymer density, and other interfacial effects[7]. Furthermore, the deformability of the shell plays another important role. For example, for the CS_{15} microgels, the rigidity not only decreases the effective contact with substrates but also results in a larger distortion of the interface, which induces a larger capillary attraction[59]. Our results shine a light on the "solid–solid isostructural phase transition". Our findings, from both this and previous work, suggest that the transition originates from the complex interplay between adhesion and capillary interactions occurring during the drying of thin films after their transfer onto solid substrates.

7. Conclusion & Future Perspectives

This study dealt with the assembly behaviours of the core-shell microgels at the air/water interfaces, focusing on the surface tension-driven monolayer evolution and monolayer structural discrepancies between *in-situ* and *ex-situ* observations. The following key achievements were accomplished:

1. Synthesis of core-shell mcirogels featuring a rigid silica core and a polymer shell with cross-linking densities, and the characterization of their internal structure and swelling/deswelling capacities.

2. Investigation of surface tension-driven monolayer evolution of core-shell microgels at air/water interfaces, and the characterization of their expansion, compression, and relaxation behavior under controlled interfacial tension gradients

3. Examination of structural discrepancies in microgel monolayers between *ex-situ* AFM observations and *in-situ* simulations, and the identification of substrate-induced artifacts affecting microgel organization during monolayer transfer.

This work firstly synthesized and characterized core-shell microgels consisting a rigid silica core and a soft PNIPAM shell via seeded precipitation polymerization. The silica core, with an average diameter of 105 ± 6 nm as determined by SAXS. The cross-linker density of the PNIPAM shell varied by adjusting the mass of BIS during synthesis, yielding microgels with nominal cross-linker densities ranging from 2.5 to 15 mol%. Successful encapsulation of the silica cores was confirmed by TEM imaging, which revealed distinct core-shell morphologies. The hydrodynamic diameter of the microgels, as measured by DLS, was approximately 300 nm at 25 °C, with temperature-dependent swelling behaviour observed between 10 and 55 °C. Microgels with

lower cross-linker densities (e.g., $CS_{2.5}$) presented higher swelling capacity compared to those with higher cross-linking. These microgels were further applied onto the air/water interfaces for investigating how interfacial tension gradients influence monolayer evolution and their interfacial assembly behaviours.

The first part of the study (**Chapter 5**) demonstrates that the evolution of freely floating microgel monolayers at air/water interfaces is governed by interfacial tension imbalances, with distinct behaviours observed under equilibrium and non-equilibrium starting conditions. By adjusting the external interfacial tension through the addition of SDS or linear PNIPAM homopolymer, monolayer expansion and compression could be precisely controlled.

Under equilibrium conditions, sufficient time was allowed for interfacial tension equilibration between the microgel-covered monolayer and the surrounding region before removing the PTFE ring. Upon ring removal, the monolayer exhibited an instantaneous expansion or compression, dictated by the pre-established interfacial tension gradient. When the external interfacial tension exceeded the tension within the microgel-covered region, rapid monolayer expansion occurred, driven by Marangoni flow. At a bulk SDS concentration of 0.5 mM, the interfacial tension imbalance was minimal, leading to stable monolayer area and nearest-neighbour distances over time. However, prolonged equilibration resulted in SDS migration into the monolayer, leading to a decrease in interfacial tension, which became more pronounced at higher SDS concentrations.

Under non-equilibrium conditions, immediate removal of the PTFE ring without prior equilibration led to rapid monolayer compression due to transient interfacial tension imbalances, followed by a gradual expansion as SDS diffused and redistributed across

the interface. This expansion was accompanied by an increase in interparticle distance while maintaining hexagonal packing of the microgels. The time-dependent evolution of the monolayer area followed a Kelvin-Voigt viscoelastic model, with the relaxation time correlated to microgel softness.

The study further demonstrates that SDS and linear PNIPAM modulate interfacial tension gradients in distinct ways. While SDS effectively reduced interfacial tension and enabled controlled compression, its migration into the microgel monolayer introduced inconsistencies in tension regulation. In contrast, linear PNIPAM provided more stable and precise tension control, preventing surfactant migration and ensuring uniform monolayer evolution. These findings establish interfacial tension gradients as a versatile tool for manipulating 2D microgel assemblies beyond conventional Langmuir trough compression, offering alternative strategies for soft material design.

The second part of the study (**Chapter 6**) explores monolayer structural discrepancies between *ex-situ* and *in-situ* observations by investigating the architecture and assembly behaviour of microgels at the air/water interfaces. By systematically varying the cross-linker density from 2.5 to 15 mol%, this study also reveals how microgel structure governs interfacial compression behaviour and the formation of distinct monolayer morphologies.

Microgels with low cross-linker densities ($CS_{2.5}$, CS_5) possess a homogeneous, single-layered fuzzy shell, as revealed by TEM imaging. These microgels underwent one-stage compression isotherms, and at high compression, they formed disordered aggregates with the nearest-neighbour distance collapsing to approximating the rigid silica core size. In contrast, highly cross-linked microgels ($CS_{7.5} \sim CS_{15}$) featured a double-layered shell architecture, consisting a dense inner layer and a fuzzy outer layer. This

structural difference leads to two-stage compression isotherms, reflecting the sequential compression of the outer and inner layers.

AFM imaging of transferred monolayers reveals a striking difference between low and highly cross-linked microgels under high compression. Highly cross-linked microgels exhibit cluster formation with voids in between, along with discontinuous reductions in the nearest-neighbour distance, which is typically interpreted as a "solid-solid isostructural phase transition" in previous studies. However, this study attributes such observations to an artefact introduced during monolayer transfer and drying rather than an intrinsic phase transition at the air/water interface.

This hypothesis is further supported by *in-situ* DPD simulations, which show continuous structural evolution across all cross-linking densities. Unlike AFM observations, in-situ simulations indicate a homogeneous microgel distribution at the interface and a smooth, gradual decrease in $d_{c\text{-}c}$ upon compression, without abrupt transitions or void formation. The discrepancy between *in-situ* and *ex-situ* observations is related to the substrate-mediated effects during monolayer transfer and drying. The substrate's hydrophobicity significantly influences these artefacts. Hydrophilic substrates promote more significant microgel clustering, leading to the structural inhomogeneities in AFM images. In contrast, hydrophobic substrates better preserve microgel organization, producing monolayer structures that more closely to the simulations. These findings highlight how deposition protocols and substrate interactions introduce artefacts in *ex-situ* AFM analysis, emphasizing the need to optimize transfer techniques and account for substrate hydrophobicity in interpreting interfacial microgel assemblies. This work underscores the critical interplay between material design, environmental factors, and methodological choices in soft matter engineering.

Future Perspectives

Building on the current findings and technical challenges identified in this study, several promising directions emerge for advancing the manipulation and characterization of microgel monolayers at fluid interfaces (for the first part of the study):

Optimized experimental and transfer protocols. During PTFE ring removal, the detachment process can create a liquid film between the ring and the water phase. This film arises due to interfacial tension between the aqueous subphase and air. When ruptured abruptly, the collapsing film generates local tension imbalances, severely disrupting the monolayer's initial size and uniformity. To minimize such disturbances, future studies could employ ultra-thin PTFE sheets (reducing film formation area) or automated mechanical systems for controlled, gradual detachment. These modifications would minimize film-derived artifacts, particularly at higher SDS concentrations (e.g., 0.5–1.0 mM).

Advanced Surfactant Systems and Additive Synergy. Future research could explore alternative surfactants and polymer-based additives to refine interfacial tension control and expand the range of accessible surface properties. Integrating synergistic additives, such as salts or copolymers, with linear PNIPAM could further extend the tunable interfacial tension range (currently 42.5–72.8 mN/m) and introduce responsive behaviours. This approach would enhance the precision and versatility of interfacial tension modulation, providing new strategies for dynamic and adaptive monolayer engineering.

And for the second part of the study:

Advancing *in-situ* imaging and dynamic analysis. The nano-scale dimensions of the studied microgels (~300 nm in diameter) present challenges for direct optical visualization of their interfacial behaviour, requiring reliance on *ex-situ* AFM imaging and simulations. To overcome this limitation, future research could employ advanced *in-situ* imaging techniques such as liquid/liquid interface AFM imaging[207] or Langmuir trough combined with small-angle light scattering[59]. These methods would enable real-time observation of microgel interfacial behaviours, minimizing the artefacts associated with *ex-situ* analysis.

Tailored substrate engineering for controlled deposition. While MPS-modified glass substrates provided hydrophobic surfaces in this study, future research could explore alternative surface modification strategies to systematically adjust hydrophobicity, roughness, and chemical functionality. Techniques such as polymer brush coatings, nanostructured surfaces, or stimuli-responsive layers (e.g., temperature- or pH-sensitive polymers) could offer deeper insights into how substrate properties influence monolayer adhesion, ordering, and stability during transfer. Additionally, investigating the effects of surface topography, including patterned roughness, on microgel deformation and assembly could refine deposition protocols, allowing for precise control over 2D lattice parameters for applications in photonics, sensing, and advanced material fabrication.

By addressing these challenges, future research can enhance the precision of microgel monolayer manipulation and characterization. Optimized transfer protocols will minimize artifacts, while advanced surfactant systems will expand tunable interfacial properties. Improved *in-situ* imaging will bridge the gap between real-time behaviour and *ex-situ* analysis, and tailored substrate engineering will refine deposition control.

These advancements will enable more scalable and functional microgel-based materials for diverse applications.

References

1. Zhang, Y., et al., *Programming Hydrogen Production via Controllable Emulsification/Demulsification in a Switchable Oil–Water System.* ACS Sustainable Chemistry & Engineering, 2019. **7**(8): p. 7768-7776.
2. Merkel, T.J., et al., *Using mechanobiological mimicry of red blood cells to extend circulation times of hydrogel microparticles.* Proc Natl Acad Sci U S A, 2011. **108**(2): p. 586-91.
3. Shimizu, K., H. Fujita, and E. Nagamori, *Oxygen plasma-treated thermoresponsive polymer surfaces for cell sheet engineering.* Biotechnology and Bioengineering, 2010. **106**(2): p. 303-310.
4. Twaites, B.R., et al., *Thermoresponsive polymers as gene delivery vectors: Cell viability, DNA transport and transfection studies.* Journal of Controlled Release, 2005. **108**(2): p. 472-483.
5. Plamper, F.A. and W. Richtering, *Functional Microgels and Microgel Systems.* Accounts of Chemical Research, 2017. **50**(2): p. 131-140.
6. Camerin, F., et al., *Microgels Adsorbed at Liquid–Liquid Interfaces: A Joint Numerical and Experimental Study.* ACS Nano, 2019. **13**(4): p. 4548-4559.
7. Rey, M., et al., *Poly-N-isopropylacrylamide Nanogels and Microgels at Fluid Interfaces.* Accounts of Chemical Research, 2020. **53**(2): p. 414-424.
8. Li, W., et al., *Comparison of the Responsivity of Solution-Suspended and Surface-Bound Poly(N-isopropylacrylamide)-Based Microgels for Sensing Applications.* ACS Appl Mater Interfaces, 2017. **9**(31): p. 26539-26548.
9. Jgamadze, D., et al., *Thermoswitching microgel carriers improve neuronal cell growth and cell release for cell transplantation.* Tissue Eng Part C Methods, 2015. **21**(1): p. 65-76.
10. Ponomareva, E., et al., *The fuzzy sphere morphology is responsible for the increase in light scattering during the shrinkage of thermoresponsive microgels.* Soft Matter, 2022. **18**(4): p. 807-825.
11. Snowden, M.J., et al., *Colloidal copolymer microgels of N-isopropylacrylamide and acrylic acid: pH, ionic strength and temperature effects.* Journal of the Chemical Society, Faraday Transactions, 1996. **92**(24): p. 5013-5016.
12. Wong, J.E., A.M. Díez-Pascual, and W. Richtering, *Layer-by-Layer Assembly of Polyelectrolyte Multilayers on Thermoresponsive P(NiPAM-co-MAA) Microgel: Effect of Ionic Strength and Molecular Weight.* Macromolecules, 2009. **42**(4): p. 1229-1238.
13. Ashraf, S., et al., *Snapshot of phase transition in thermoresponsive hydrogel PNIPAM: Role in drug delivery and tissue engineering.* Macromolecular Research, 2016. **24**(4): p. 297-304.
14. Islam, M.R., et al., *Poly (N-isopropylacrylamide) microgel-based optical devices for sensing and biosensing.* Sensors, 2014. **14**(5): p. 8984-8995.
15. Lin, T., et al., *Poly(N-isopropylacrylamide)-based smart hydrogels: Design, properties and applications.* Progress in Materials Science, 2021. **115**: p. 100702.
16. Fernandez-Rodriguez, M.A., M.N. Antonopoulou, and L. Isa, *Near-zero surface pressure assembly of rectangular lattices of microgels at fluid interfaces for colloidal lithography.* Soft Matter, 2021. **17**(2): p. 335-340.

17. Tsuji, S. and H. Kawaguchi, *Colored Thin Films Prepared from Hydrogel Microspheres.* Langmuir, 2005. **21**(18): p. 8439-8442.
18. Nemiroski, A., et al., *Engineering shadows to fabricate optical metasurfaces.* ACS nano, 2014. **8**(11): p. 11061-11070.
19. Volk, K., et al., *Time-Controlled Colloidal Superstructures: Long-Range Plasmon Resonance Coupling in Particle Monolayers.* Adv Mater, 2015. **27**(45): p. 7332-7.
20. Volk, K., et al., *Reversible Tuning of Visible Wavelength Surface Lattice Resonances in Self-Assembled Hybrid Monolayers.* Advanced Optical Materials, 2017. **5**(9).
21. Halperin, A., M. Kröger, and F.M. Winnik, *Poly (N‐isopropylacrylamide) phase diagrams: fifty years of research.* Angewandte Chemie International Edition, 2015. **54**(51): p. 15342-15367.
22. Cole, M.A., et al., *Stimuli-responsive interfaces and systems for the control of protein–surface and cell–surface interactions.* Biomaterials, 2009. **30**(9): p. 1827-1850.
23. Gil, E.S. and S.M. Hudson, *Stimuli-reponsive polymers and their bioconjugates.* Progress in Polymer Science, 2004. **29**(12): p. 1173-1222.
24. Pelton, R., *Temperature-sensitive aqueous microgels.* Advances in Colloid and Interface Science, 2000. **85**(1): p. 1-33.
25. Pelton, R.H. and P. Chibante, *Preparation of aqueous latices with N-isopropylacrylamide.* Colloids and Surfaces, 1986. **20**(3): p. 247-256.
26. McPhee, W., K.C. Tam, and R. Pelton, *Poly(N-isopropylacrylamide) Latices Prepared with Sodium Dodecyl Sulfate.* Journal of Colloid and Interface Science, 1993. **156**(1): p. 24-30.
27. von Nessen, K., M. Karg, and T. Hellweg, *Thermoresponsive poly-(N-isopropylmethacrylamide) microgels: Tailoring particle size by interfacial tension control.* Polymer, 2013. **54**(21): p. 5499-5510.
28. Peters, A. and S. Candau, *Kinetics of swelling of polyacrylamide gels.* Macromolecules, 1986. **19**(7): p. 1952-1955.
29. Heskins, M. and J.E. Guillet, *Solution Properties of Poly(N-isopropylacrylamide).* Journal of Macromolecular Science: Part A - Chemistry, 1968. **2**(8): p. 1441-1455.
30. Wu, T., Z. Ge, and S. Liu, *Fabrication of Thermoresponsive Cross-Linked Poly(N-isopropylacrylamide) Nanocapsules and Silver Nanoparticle-Embedded Hybrid Capsules with Controlled Shell Thickness.* Chemistry of Materials, 2011. **23**(9): p. 2370-2380.
31. Nguyen, H.H., et al., *Thermoresponsive Properties of PNIPAM-Based Hydrogels: Effect of Molecular Architecture and Embedded Gold Nanoparticles.* Langmuir, 2015. **31**(16): p. 4761-4768.
32. Xu, X., et al., *A Near-Infrared and Temperature-Responsive Pesticide Release Platform through Core–Shell Polydopamine@PNIPAm Nanocomposites.* ACS Applied Materials & Interfaces, 2017. **9**(7): p. 6424-6432.
33. Contreras-Cáceres, R., et al., *Au@pNIPAM Thermosensitive Nanostructures: Control over Shell Cross-linking, Overall Dimensions, and Core Growth.* Advanced Functional Materials, 2009. **19**(19): p. 3070-3076.
34. Karg, M., et al., *Surface Plasmon Spectroscopy of Gold−Poly-N-isopropylacrylamide Core−Shell Particles.* Langmuir, 2011. **27**(2): p. 820-827.

35. Karg, M., T. Hellweg, and P. Mulvaney, *Self - Assembly of Tunable Nanocrystal Superlattices Using Poly - (NIPAM) Spacers.* Advanced Functional Materials, 2011. **21**(24): p. 4668-4676.
36. Somerville, W.R.C., et al., *Pattern formation in two-dimensional hard-core/soft-shell systems with variable soft shell profiles.* Soft Matter, 2020. **16**(14): p. 3564-3573.
37. Menath, J., et al., *Defined core–shell particles as the key to complex interfacial self-assembly.* Proceedings of the National Academy of Sciences, 2021. **118**(52): p. e2113394118.
38. Karg, M., et al., *Well defined hybrid PNIPAM core-shell microgels: size variation of the silica nanoparticle core.* Colloid and Polymer Science, 2011. **289**(5): p. 699-709.
39. McGrath, J.G., et al., *Self-Assembly of "Paint-On" Colloidal Crystals Using Poly(styrene-co-N-isopropylacrylamide) Spheres.* Chemistry of Materials, 2007. **19**(7): p. 1584-1591.
40. Zhou, M., et al., *A facile method to assemble PNIPAM-containing microgel photonic crystals.* Chemphyschem, 2009. **10**(3): p. 523-6.
41. Guillermo, A., et al., *NMR investigations into heterogeneous structures of thermosensitive microgel particles.* Journal of Polymer Science Part B: Polymer Physics, 2000. **38**(6): p. 889-898.
42. Fernandez-Barbero, A., et al., *Structural modifications in the swelling of inhomogeneous microgels by light and neutron scattering.* Phys Rev E Stat Nonlin Soft Matter Phys, 2002. **66**(5 Pt 1): p. 051803.
43. Wu, X., et al., *The kinetics of poly(N-isopropylacrylamide) microgel latex formation.* Colloid and Polymer Science, 1994. **272**(4): p. 467-477.
44. Varga, I., et al., *Effect of Cross-Link Density on the Internal Structure of Poly(N-isopropylacrylamide) Microgels.* The Journal of Physical Chemistry B, 2001. **105**(38): p. 9071-9076.
45. Hoare, T. and D. McLean, *Kinetic Prediction of Functional Group Distributions in Thermosensitive Microgels.* The Journal of Physical Chemistry B, 2006. **110**(41): p. 20327-20336.
46. Stieger, M., et al., *Small-angle neutron scattering study of structural changes in temperature sensitive microgel colloids.* J Chem Phys, 2004. **120**(13): p. 6197-206.
47. Höfl, S., et al., *Volume phase transition of "smart" microgels in bulk solution and adsorbed at an interface: A combined AFM, dynamic light, and small angle neutron scattering study.* Polymer, 2007. **48**(1): p. 245-254.
48. Acciaro, R., T. Gilányi, and I. Varga, *Preparation of Monodisperse Poly(N-isopropylacrylamide) Microgel Particles with Homogenous Cross-Link Density Distribution.* Langmuir, 2011. **27**(12): p. 7917-7925.
49. Witte, J., et al., *A comparison of the network structure and inner dynamics of homogeneously and heterogeneously crosslinked PNIPAM microgels with high crosslinker content.* Soft Matter, 2019. **15**(5): p. 1053-1064.
50. Mehrabian, H., J. Harting, and J.H. Snoeijer, *Soft particles at a fluid interface.* Soft Matter, 2016. **12**(4): p. 1062-1073.
51. Style, R.W., L. Isa, and E.R. Dufresne, *Adsorption of soft particles at fluid interfaces.* Soft Matter, 2015. **11**(37): p. 7412-9.
52. Destribats, M., et al., *Soft microgels as Pickering emulsion stabilisers: role of particle deformability.* Soft Matter, 2011. **7**(17).

53. Pinaud, F., et al., *Adsorption of microgels at an oil–water interface: correlation between packing and 2D elasticity.* Soft Matter, 2014. **10**(36): p. 6963-6974.
54. Geisel, K., L. Isa, and W. Richtering, *Unraveling the 3D Localization and Deformation of Responsive Microgels at Oil/Water Interfaces: A Step Forward in Understanding Soft Emulsion Stabilizers.* Langmuir, 2012. **28**(45): p. 15770-15776.
55. Style, R.W., L. Isa, and E.R. Dufresne, *Adsorption of soft particles at fluid interfaces.* Soft Matter, 2015. **11**(37): p. 7412-7419.
56. Scotti, A., et al., *How Softness Matters in Soft Nanogels and Nanogel Assemblies.* Chem Rev, 2022.
57. Geisel, K., et al., *Hollow and Core–Shell Microgels at Oil–Water Interfaces: Spreading of Soft Particles Reduces the Compressibility of the Monolayer.* Langmuir, 2015. **31**(48): p. 13145-13154.
58. Vialetto, J., et al., *Effect of Internal Architecture on the Assembly of Soft Particles at Fluid Interfaces.* ACS Nano, 2021. **15**(8): p. 13105-13117.
59. Kuk, K., et al., *Compression of colloidal monolayers at liquid interfaces: in situ vs. ex situ investigation.* Soft Matter, 2022.
60. Kuk, K., et al., *Drying of Soft Colloidal Films.* Advanced Science. **n/a**(n/a): p. 2406977.
61. Deshmukh, O.S., et al., *Hard and soft colloids at fluid interfaces: Adsorption, interactions, assembly & rheology.* Advances in Colloid and Interface Science, 2015. **222**: p. 215-227.
62. Wellert, S., et al., *Responsive Microgels at Surfaces and Interfaces.* Zeitschrift für Physikalische Chemie, 2015. **229**(7-8): p. 1225-1250.
63. Monteillet, H., et al., *Ultrastrong Anchoring Yet Barrier-Free Adsorption of Composite Microgels at Liquid Interfaces.* Advanced Materials Interfaces, 2014. **1**(7).
64. Goulet, P.J.G., et al., *Surface-Enhanced Raman Scattering on Dendrimer/Metallic Nanoparticle Layer-by-Layer Film Substrates.* Langmuir, 2005. **21**(12): p. 5576-5581.
65. Maier, S.A., et al., *Local detection of electromagnetic energy transport below the diffraction limit in metal nanoparticle plasmon waveguides.* Nature Materials, 2003. **2**(4): p. 229-232.
66. Hayakawa, T., et al., *Second Harmonic Generation from Coupled Surface-Plasmon Resonances in Self-Assembled Gold-Nanoparticle Monolayers Coated with an Aminosilane.* Advanced Materials, 2004. **16**(16): p. 1408-1412.
67. Vogel, N., et al., *Wafer-Scale Fabrication of Ordered Binary Colloidal Monolayers with Adjustable Stoichiometries.* Advanced Functional Materials, 2011. **21**(16): p. 3064-3073.
68. Feller, D. and M. Karg, *Fluid interface-assisted assembly of soft microgels: recent developments for structures beyond hexagonal packing.* Soft Matter, 2022. **18**(34): p. 6301-6312.
69. Menath, J., et al., *Acoustic Crystallization of 2D Colloidal Crystals.* Advanced Materials, 2023. **35**(2).
70. He, G.Z., et al., *Regulating two-dimensional colloidal crystal assembly through contactless acoustic annealing.* Journal of Applied Physics, 2024. **135**(14).
71. Geisel, K., W. Richtering, and L. Isa, *Highly ordered 2D microgel arrays: compression*

self-assembly. Soft Matter, 2014. **10**(40): p. 7968-7976.
72. Rey, M., et al., *A Dirty Story: Improving Colloidal Monolayer Formation by Understanding the Effect of Impurities at the Air/Water Interface.* Langmuir, 2019. **35**(1): p. 95-103.
73. Nishizawa, Y., et al., *Controlling the shell structure of hard core/hydrogel shell microspheres.* Colloid and Polymer Science, 2022. **300**(4): p. 333-340.
74. Kuk, K., et al., *Micron-Sized Silica-PNIPAM Core-Shell Microgels with Tunable Shell-To-Core Ratio.* Gels, 2022. **8**(8).
75. Jaber, S., et al., *2D assembly of gold-PNIPAM core-shell nanocrystals.* Physical Chemistry Chemical Physics, 2011. **13**(13): p. 5576-5578.
76. Karg, M., *Functional Materials Design through Hydrogel Encapsulation of Inorganic Nanoparticles: Recent Developments and Challenges.* Macromolecular Chemistry and Physics, 2016. **217**(2): p. 242-255.
77. Geisel, K., W. Richtering, and L. Isa, *Highly ordered 2D microgel arrays: compression versus self-assembly.* Soft Matter, 2014. **10**(40): p. 7968-7976.
78. Kralchevsky, P.A. and K. Nagayama, *Capillary forces between colloidal particles.* Langmuir, 1994. **10**(1): p. 23-36.
79. Kralchevsky, P.A. and K. Nagayama, *Capillary interactions between particles bound to interfaces, liquid films and biomembranes.* Advances in Colloid and Interface Science, 2000. **85**(2): p. 145-192.
80. Honold, T., et al., *Tunable plasmonic surfaces*

colloid assembly. Journal of Materials Chemistry C, 2015. **3**(43): p. 11449-11457.
81. Meng, X. and D. Qiu, *Gas-Flow-Induced Reorientation to Centimeter-Sized Two-Dimensional Colloidal Single Crystal of Polystyrene Particle.* Langmuir, 2014. **30**(11): p. 3019-3023.
82. Vogel, N., et al., *A Convenient Method to Produce Close- and Non-close-Packed Monolayers using Direct Assembly at the Air–Water Interface and Subsequent Plasma-Induced Size Reduction.* Macromolecular Chemistry and Physics, 2011. **212**(16): p. 1719-1734.
83. Guo, Q., C. Arnoux, and R.E. Palmer, *Guided Assembly of Colloidal Particles on Patterned Substrates.* Langmuir, 2001. **17**(22): p. 7150-7155.
84. Gu, Z.-Z., A. Fujishima, and O. Sato, *Patterning of a Colloidal Crystal Film on a Modified Hydrophilic and Hydrophobic Surface.* Angewandte Chemie International Edition, 2002. **41**(12): p. 2067-2070.
85. Fan, F. and K.J. Stebe, *Assembly of Colloidal Particles by Evaporation on Surfaces with Patterned Hydrophobicity.* Langmuir, 2004. **20**(8): p. 3062-3067.
86. Zhang, J. and B. Yang, *Patterning Colloidal Crystals and Nanostructure Arrays by Soft Lithography.* Advanced Functional Materials, 2010. **20**(20): p. 3411-3424.
87. Scriven, L.E. and C.V. Sternling, *The Marangoni Effects.* Nature, 1960. **187**(4733): p. 186-188.
88. Rauh, A., et al., *Compression of hard core–soft shell nanoparticles at liquid–liquid interfaces: influence of the shell thickness.* Soft Matter, 2017. **13**(1): p. 158-169.
89. Tang, J.S.J., et al., *Surface Patterning with SiO2@PNiPAm Core–Shell Particles.* ACS Omega, 2018. **3**(9): p. 12089-12098.
90. Rey, M., et al., *Isostructural solid-solid phase transition in monolayers of soft core-shell particles at fluid interfaces: structure and mechanics.* Soft Matter, 2016. **12**(15): p. 3545-57.

91. Ickler, M., et al., *Interfacial self-assembly of SiO2–PNIPAM core–shell particles with varied crosslinking density.* Soft Matter, 2022. **18**(30): p. 5585-5597.
92. Alvarez, L.H., et al., *Controlling microgel deformation via deposition method and surface functionalization of solid supports.* Physical Chemistry Chemical Physics, 2021. **23**(8): p. 4927-4934.
93. Levy, D. and M. Zayat, *The Sol-Gel Handbook, 3 Volume Set: Synthesis, Characterization, and Applications*. Vol. 2. 2015: John Wiley & Sons.
94. Stöber, W., A. Fink, and E. Bohn, *Controlled growth of monodisperse silica spheres in the micron size range.* Journal of Colloid and Interface Science, 1968. **26**(1): p. 62-69.
95. Romanov, S.G., et al., *Probing guided modes in a monolayer colloidal crystal on a flat metal film.* Physical Review B, 2012. **86**(19): p. 195145.
96. Badley, R.D., et al., *Surface modification of colloidal silica.* Langmuir, 1990. **6**(4): p. 792-801.
97. Hunkeler, D., *Mechanism and kinetics of the persulfate-initiated polymerization of acrylamide.* Macromolecules, 1991. **24**(9): p. 2160-2171.
98. Schild, H.G., *Poly(N-isopropylacrylamide): experiment, theory and application.* Progress in Polymer Science, 1992. **17**(2): p. 163-249.
99. Kuk, K., et al., *Micron-Sized Silica-PNIPAM Core-Shell Microgels with Tunable Shell-To-Core Ratio.* Gels, 2022. **8**(8): p. 516.
100. Contreras‐Cáceres, R., et al., *Encapsulation and growth of gold nanoparticles in thermoresponsive microgels.* Advanced Materials, 2008. **20**(9): p. 1666-1670.
101. Contreras-Cáceres, R., et al., *Encapsulation and Growth of Gold Nanoparticles in Thermoresponsive Microgels.* Advanced Materials, 2008. **20**(9): p. 1666-1670.
102. Schmid, A.J., et al., *Multi-Shell Hollow Nanogels with Responsive Shell Permeability.* Scientific Reports, 2016. **6**(1): p. 22736.
103. Zha, L.S., et al., *Monodisperse Temperature-Sensitive Microcontainers.* Advanced Materials, 2002. **14**(15).
104. Meng, Z., M.H. Smith, and L.A. Lyon, *Temperature-programmed synthesis of micron-sized multi-responsive microgels.* Colloid and Polymer Science, 2009. **287**(3): p. 277-285.
105. Meunier, F., C. Pichot, and A. Elaïssari, *Effect of thiol-containing monomer on the preparation of temperature-sensitive hydrogel microspheres.* Colloid and Polymer Science, 2006. **284**(11): p. 1287-1292.
106. Reculusa, S., et al., *Synthesis of Daisy-Shaped and Multipod-like Silica/Polystyrene Nanocomposites.* Nano Letters, 2004. **4**(9): p. 1677-1682.
107. Rauh, A., T. Honold, and M. Karg, *Seeded precipitation polymerization for the synthesis of gold-hydrogel core-shell particles: the role of surface functionalization and seed concentration.* Colloid and Polymer Science, 2016. **294**(1): p. 37-47.
108. Maeda, Y., T. Higuchi, and I. Ikeda, *Change in Hydration State during the Coil−Globule Transition of Aqueous Solutions of Poly(N-isopropylacrylamide) as Evidenced by FTIR Spectroscopy.* Langmuir, 2000. **16**(19): p. 7503-7509.
109. Mura, S., J. Nicolas, and P. Couvreur, *Stimuli-responsive nanocarriers for drug delivery.* Nature materials, 2013. **12**(11): p. 991-1003.
110. Jaber, S., et al., *2D assembly of gold–PNIPAM core–shell nanocrystals.* Physical Chemistry Chemical Physics, 2011. **13**(13): p. 5576-5578.

111. Guerzoni, L.P., et al., *Microfluidic fabrication of polyethylene glycol microgel capsules with tailored properties for the delivery of biomolecules.* Biomaterials science, 2017. **5**(8): p. 1549-1557.
112. Ilmain, F., T. Tanaka, and E. Kokufuta, *Volume transition in a gel driven by hydrogen bonding.* Nature, 1991. **349**(6308): p. 400-401.
113. Karg, M., et al., *Temperature, pH, and ionic strength induced changes of the swelling behavior of PNIPAM− poly (allylacetic acid) copolymer microgels.* Langmuir, 2008. **24**(12): p. 6300-6306.
114. Flory, P.J. and J. Rehner, Jr., *Statistical Mechanics of Cross-Linked Polymer Networks I. Rubberlike Elasticity.* The Journal of Chemical Physics, 1943. **11**(11): p. 512-520.
115. Flory, P.J., *Principles of polymer chemistry*. 1953: Cornell university press.
116. Quesada-Pérez, M., et al., *Gel swelling theories: the classical formalism and recent approaches.* Soft Matter, 2011. **7**(22): p. 10536-10547.
117. Hertle, Y., et al., *Responsive P(NIPAM-co-NtBAM) microgels: Flory–Rehner description of the swelling behaviour.* Colloid and Polymer Science, 2010. **288**(10): p. 1047-1059.
118. Balaceanu, A., et al., *Microgel Heterogeneous Morphology Reflected in Temperature-Induced Volume Transition and 1H High-Resolution Transverse Relaxation NMR. The Case of Poly(N-vinylcaprolactam) Microgel.* Macromolecules, 2011. **44**(7): p. 2161-2169.
119. Lopez, C.G. and W. Richtering, *Does Flory–Rehner theory quantitatively describe the swelling of thermoresponsive microgels?* Soft Matter, 2017. **13**(44): p. 8271-8280.
120. R.G.M, *Biopolymer gel swelling analysed with scaling laws and Flory–Rehner theory.* Food Hydrocolloids, 2015. **48**: p. 94-101.
121. Andersson, M. and S.L. Maunu, *Structural studies of poly (N-isopropylacrylamide) microgels: Effect of SDS surfactant concentration in the microgel synthesis.* Journal of Polymer Science Part B: Polymer Physics, 2006. **44**(23): p. 3305-3314.
122. Cipelletti, L., V. Trappe, and D.J. Pine, *Scattering Techniques*, in *Fluids, Colloids and Soft Materials: An Introduction to Soft Matter Physics*. 2016. p. 131-148.
123. Karg, M., et al., *Thermoresponsive core–shell microgels with silica nanoparticle cores: size, structure, and volume phase transition of the polymer shell.* Physical Chemistry Chemical Physics, 2008. **10**(44): p. 6708-6716.
124. Ballauff, M., *SAXS and SANS studies of polymer colloids.* Current Opinion in Colloid & Interface Science, 2001. **6**(2): p. 132-139.
125. Kratz, K., T. Hellweg, and W. Eimer, *Structural changes in PNIPAM microgel particles as seen by SANS, DLS, and EM techniques.* Polymer, 2001. **42**(15): p. 6631-6639.
126. Svaneborg, C. and J.S. Pedersen, *Block copolymer micelle coronas as quasi-two-dimensional dilute or semidilute polymer solutions.* Physical Review E, 2001. **64**(1): p. 010802.
127. Karg, M., et al., *A versatile approach for the preparation of thermosensitive PNIPAM core-shell microgels with nanoparticle cores.* Chemphyschem, 2006. **7**(11): p. 2298-301.
128. Lim, J., et al., *Characterization of magnetic nanoparticle by dynamic light scattering.* Nanoscale Research Letters, 2013. **8**(1): p. 381.

129. Stetefeld, J., S.A. McKenna, and T.R. Patel, *Dynamic light scattering: a practical guide and applications in biomedical sciences.* Biophysical reviews, 2016. **8**(4): p. 409-427.
130. Goldburg, W.I., *Dynamic light scattering.* American Journal of Physics, 1999. **67**(12): p. 1152-1160.
131. Berne, B.J. and R. Pecora, *Dynamic light scattering: with applications to chemistry, biology, and physics*. 2000: Courier Corporation.
132. Frisken, B.J., *Revisiting the method of cumulants for the analysis of dynamic light-scattering data.* Applied Optics, 2001. **40**(24): p. 4087-4091.
133. Pecora, R., *Dynamic light scattering: applications of photon correlation spectroscopy*. 2013: Springer Science & Business Media.
134. Koppel, D.E., *Analysis of Macromolecular Polydispersity in Intensity Correlation Spectroscopy: The Method of Cumulants.* The Journal of Chemical Physics, 1972. **57**(11): p. 4814-4820.
135. Nishi, K., et al., *SANS and DLS Study of Tacticity Effects on Hydrophobicity and Phase Separation of Poly(N-isopropylacrylamide).* Macromolecules, 2013. **46**(15): p. 6225-6232.
136. Musial, W., et al., *Morphological characteristics of modified freeze-dried poly(N-isopropylacrylamide) microspheres studied by optical microscopy, SEM, and DLS.* Chemical Papers, 2010. **64**(5): p. 602-612.
137. Kojima, H., et al., *Temperature dependent phase behavior of PNIPAM microgels in mixed water/methanol solvents.* Journal of Polymer Science Part B: Polymer Physics, 2013. **51**(14): p. 1100-1111.
138. Karg, M., et al., *Temperature, pH, and Ionic Strength Induced Changes of the Swelling Behavior of PNIPAM−Poly(allylacetic acid) Copolymer Microgels.* Langmuir, 2008. **24**(12): p. 6300-6306.
139. Derjaguin, B. and L. Landau, *Theory of the stability of strongly charged lyophobic sols and of the adhesion of strongly charged particles in solutions of electrolytes.* Progress in Surface Science, 1993. **43**(1): p. 30-59.
140. Ninham, B.W., *On progress in forces since the DLVO theory.* Advances in Colloid and Interface Science, 1999. **83**(1): p. 1-17.
141. Langford, A., M. Bruchsaler, and M. Gupta, *8 - Suspension properties and characterization of aluminum-adjuvanted vaccines*, in *Practical Aspects of Vaccine Development*, P. Kolhe and S. Ohtake, Editors. 2022, Academic Press. p. 225-266.
142. Senff, H. and W. Richtering, *Temperature sensitive microgel suspensions: Colloidal phase behavior and rheology of soft spheres.* The Journal of chemical physics, 1999. **111**(4): p. 1705-1711.
143. Senff, H. and W. Richtering, *Influence of cross-link density on rheological properties of temperature-sensitive microgel suspensions.* Colloid and Polymer Science, 2000. **278**(9): p. 830-840.
144. Eckert, T. and W. Richtering, *Thermodynamic and hydrodynamic interaction in concentrated microgel suspensions: Hard or soft sphere behavior?* The Journal of Chemical Physics, 2008. **129**(12).
145. Heyes, D.M. and A.C. Brańka, *Interactions between microgel particles.* Soft Matter, 2009. **5**(14): p. 2681-2685.
146. Deshmukh, O.S., et al., *Hard and soft colloids at fluid interfaces: Adsorption, interactions, assembly & rheology.* Adv Colloid Interface Sci, 2015. **222**: p. 215-27.

147. Masschaele, K., et al., *Finite Ion-Size Effects Dominate the Interaction between Charged Colloidal Particles at an Oil-Water Interface.* Physical Review Letters, 2010. **105**(4): p. 048303.
148. Wang, W. and B. Gu, *Self-Assembly of Two- and Three-Dimensional Particle Arrays by Manipulating the Hydrophobicity of Silica Nanospheres.* The Journal of Physical Chemistry B, 2005. **109**(47): p. 22175-22180.
149. Vassileva, N.D., et al., *Capillary Forces between Spherical Particles Floating at a Liquid−Liquid Interface.* Langmuir, 2005. **21**(24): p. 11190-11200.
150. Stamou, D., C. Duschl, and D. Johannsmann, *Long-range attraction between colloidal spheres at the air-water interface: The consequence of an irregular meniscus.* Physical Review E, 2000. **62**(4): p. 5263-5272.
151. Loudet, J.C., et al., *Capillary Interactions Between Anisotropic Colloidal Particles.* Physical Review Letters, 2005. **94**(1): p. 018301.
152. Rauh, A., et al., *Compression of hard core-soft shell nanoparticles at liquid-liquid interfaces: influence of the shell thickness.* Soft Matter, 2016. **13**(1): p. 158-169.
153. Picard, C., et al., *Organization of Microgels at the Air–Water Interface under Compression: Role of Electrostatics and Cross-Linking Density.* Langmuir, 2017. **33**(32): p. 7968-7981.
154. Butt, H.-J., et al., *Capillary forces between soft, elastic spheres.* Soft Matter, 2010. **6**(23): p. 5930-5936.
155. Butt, H.-J., *Capillary Forces: Influence of Roughness and Heterogeneity.* Langmuir, 2008. **24**(9): p. 4715-4721.
156. Okado, Y., et al., *Adsorption Behavior at the Air/Water Interface for PNIPAM-adsorbed Colloidal Silica.* Chemistry Letters, 2012. **41**(10): p. 1168-1170.
157. Vogel, N., et al., *Ordered arrays of gold nanostructures from interfacially assembled Au@PNIPAM hybrid nanoparticles.* Langmuir, 2012. **28**(24): p. 8985-93.
158. Han, Y., et al., *Unraveling the Growth Mechanism of Silica Particles in the Stöber Method: In Situ Seeded Growth Model.* Langmuir, 2017. **33**(23): p. 5879-5890.
159. Haynes, C.L. and R.P. Van Duyne, *Nanosphere Lithography: A Versatile Nanofabrication Tool for Studies of Size-Dependent Nanoparticle Optics.* The Journal of Physical Chemistry B, 2001. **105**(24): p. 5599-5611.
160. Haes, A.J. and R.P. Van Duyne, *A Nanoscale Optical Biosensor: Sensitivity and Selectivity of an Approach Based on the Localized Surface Plasmon Resonance Spectroscopy of Triangular Silver Nanoparticles.* Journal of the American Chemical Society, 2002. **124**(35): p. 10596-10604.
161. Micheletto, R., H. Fukuda, and M. Ohtsu, *A simple method for the production of a two-dimensional, ordered array of small latex particles.* Langmuir, 1995. **11**(9): p. 3333-3336.
162. Denkov, N., et al., *Mechanism of formation of two-dimensional crystals from latex particles on substrates.* Langmuir, 1992. **8**(12): p. 3183-3190.
163. Denkov, N.D., et al., *Two-dimensional crystallization.* Nature, 1993. **361**(6407): p. 26-26.
164. Park, S.H., D. Qin, and Y. Xia, *Crystallization of Mesoscale Particles over Large Areas.* Advanced Materials, 1998. **10**(13): p. 1028-1032.
165. Malaquin, L., et al., *Controlled Particle Placement through Convective and Capillary Assembly.* Langmuir, 2007. **23**(23): p. 11513-11521.

166. Prevo, B.G. and O.D. Velev, *Controlled, Rapid Deposition of Structured Coatings from Micro- and Nanoparticle Suspensions.* Langmuir, 2004. **20**(6): p. 2099-2107.
167. Scheidegger, L., et al., *Compression and deposition of microgel monolayers from fluid interfaces: particle size effects on interface microstructure and nanolithography.* Physical Chemistry Chemical Physics, 2017. **19**(13): p. 8671-8680.
168. Rey, M., et al., *Interfacial arrangement and phase transitions of PNiPAm microgels with different crosslinking densities.* Soft Matter, 2017. **13**(46): p. 8717-8727.
169. Fernández-Rodríguez, M.Á., et al., *Tunable 2D binary colloidal alloys for soft nanotemplating.* Nanoscale, 2018. **10**(47): p. 22189-22195.
170. Shalaka, K.K., et al., *A miniaturized radial Langmuir trough for simultaneous dilatational deformation and interfacial microscopy.* Journal of Colloid and Interface Science, 2021. **582**: p. 1085-1098.
171. Retsch, M., et al., *Fabrication of Large-Area, Transferable Colloidal Monolayers Utilizing Self-Assembly at the Air/Water Interface.* Macromolecular Chemistry and Physics, 2009. **210**(3-4): p. 230-241.
172. Ponomareva, E., et al., *Surface Lattice Resonances in Self-Assembled Gold Nanoparticle Arrays: Impact of Lattice Period, Structural Disorder, and Refractive Index on Resonance Quality.* Langmuir, 2020. **36**(45): p. 13601-13612.
173. Hayat, M., *Basic techniques for transmission electron microscopy*. 2012: Elsevier.
174. Contreras-Cáceres, R., et al., *Effect of the Cross-Linking Density on the Thermoresponsive Behavior of Hollow PNIPAM Microgels.* Langmuir, 2015. **31**(3): p. 1142-1149.
175. Albert, G.-C., et al., *In situ single particle characterization of the themoresponsive and co-nonsolvent behavior of PNIPAM microgels and silica@PNIPAM core-shell colloids.* Journal of Colloid and Interface Science, 2023. **635**: p. 552-561.
176. Gelissen, A.P.H., et al., *3D Structures of Responsive Nanocompartmentalized Microgels.* Nano Letters, 2016. **16**(11): p. 7295-7301.
177. Xing, Z., et al., *pH/temperature dual stimuli-responsive microcapsules with interpenetrating polymer network structure.* Colloid and Polymer Science, 2010. **288**(18): p. 1723-1729.
178. Alexander, S., et al., *An atomic - resolution atomic - force microscope implemented using an optical lever.* Journal of Applied Physics, 1989. **65**(1): p. 164-167.
179. Binnig, G., C.F. Quate, and C. Gerber, *Atomic Force Microscope.* Physical Review Letters, 1986. **56**(9): p. 930-933.
180. Volk, K., et al., *Moiré and honeycomb lattices through self-assembly of hard-core/soft-shell microgels: experiment and simulation.* Physical Chemistry Chemical Physics, 2019. **21**(35): p. 19153-19162.
181. Sorrell, C.D. and L.A. Lyon, *Deformation Controlled Assembly of Binary Microgel Thin Films.* Langmuir, 2008. **24**(14): p. 7216-7222.
182. Tanaka, H., T. Hayashi, and T. Nishi, *Application of digital image analysis to pattern formation in polymer systems.* Journal of Applied Physics, 1986. **59**(11): p. 3627-3643.

183. Bretonnet, J.-L., *Thermodynamic perturbation theory of simple liquids*. 2011: IntechOpen.
184. Jiqing, Z., et al., *Microstructure evaluation of polymer-modified bitumen by image analysis using two-dimensional fast Fourier transform.* Materials & Design, 2018. **137**: p. 164-175.
185. Heckbert, P., *Fourier transforms and the fast Fourier transform (FFT) algorithm.* Computer Graphics, 1995. **2**(1995): p. 15-463.
186. Peter, J.Y., et al., *Physics in ordered and disordered colloidal matter composed of poly(N-isopropylacrylamide) microgel particles.* Reports on Progress in Physics, 2014. **77**(5): p. 056601.
187. Ziman, J.M., *Models of disorder: the theoretical physics of homogeneously disordered systems*. 1979: Cambridge university press.
188. Contreras, M. and J. Valenzuela, *A two-dimensional model of a liquid: The pair-correlation function.* Journal of Chemical Education, 1986. **63**(1): p. 7.
189. Masalov, V.M., et al., *Mechanism of formation and nanostructure of Stöber silica particles.* Nanotechnology, 2011. **22**(27): p. 275718.
190. Volk, K., et al., *Moire and honeycomb lattices through self-assembly of hard-core/soft-shell microgels: experiment and simulation.* Physical Chemistry Chemical Physics, 2019. **21**(35): p. 19153-19162.
191. Zhou, Y., J.J. Crassous, and M. Karg, *Core–Shell Microgels at Air/Water Interfaces: Role of Interfacial Tension in Monolayer Evolution.* Langmuir, 2025.
192. Wu, C. and X. Wang, *Globule-to-coil transition of a single homopolymer chain in solution.* Physical Review Letters, 1998. **80**(18): p. 4092.
193. Menath, J., et al., *Acoustic Crystallization of 2D Colloidal Crystals.* Advanced Materials, 2023. **35**(2): p. 2206593.
194. Lotito, V. and T. Zambelli, *Self-Assembly of Single-Sized and Binary Colloidal Particles at Air/Water Interface by Surface Confinement and Water Discharge.* Langmuir, 2016. **32**(37): p. 9582-9590.
195. Matsuoka, K., et al., *Micelle Formation of Dodecanoic Acid with Alkali Metal Counterions.* Journal of Oleo Science, 2023. **72**(9): p. 831-837.
196. Kuk, K., et al., *Drying of Soft Colloidal Films.* Advanced Science. **10.1002/advs.202406977**.
197. Kuk, K., et al., *Compression of colloidal monolayers at liquid interfaces: in situ vs. ex situ investigation.* Soft Matter, 2023. **19**: p. 175-188.
198. Scotti, A., et al., *How Softness Matters in Soft Nanogels and Nanogel Assemblies.* Chem Rev, 2022. **122**(13): p. 11675–11700.
199. Tuckermann, R., *Surface tension of aqueous solutions of water-soluble organic and inorganic compounds.* Atmospheric Environment, 2007. **41**(29): p. 6265-6275.
200. Zhang, J. and R. Pelton, *Poly(N-isopropylacrylamide) Microgels at the Air−Water Interface.* Langmuir, 1999. **15**(23): p. 8032-8036.
201. Karg, M., et al. *Poly-NIPAM Microgels with Different Cross-Linker Densities*. 2013. Cham: Springer International Publishing.
202. Tadgell, B., et al., *Temperature-Jump Spectroscopy of Gold–Poly(N-isopropylacrylamide) Core–Shell Microgels.* The Journal of Physical Chemistry C, 2022. **126**(8): p. 4118-4131.
203. Vasudevan, S.A., et al., *Stable in Bulk and Aggregating at the Interface: Comparing Core–Shell Nanoparticles in Suspension and at Fluid Interfaces.* Langmuir, 2018. **34**(3): p. 886-895.

204. Pinaud, F., et al., *Adsorption of microgels at an oil-water interface: correlation between packing and 2D elasticity.* Soft Matter, 2014. **10**(36): p. 6963-74.
205. Bochenek, S., et al., *Influence of Architecture on the Interfacial Properties of Polymers: Linear Chains, Stars, and Microgels.* Langmuir, 2023. **39**(50): p. 18354-18365.
206. Hoppe Alvarez, L., et al., *Deformation of Microgels at Solid–Liquid Interfaces Visualized in Three-Dimension.* Nano Letters, 2019. **19**(12): p. 8862-8867.
207. Costa, L., et al., *Liquid–Liquid Interfacial Imaging Using Atomic Force Microscopy.* Advanced Materials Interfaces, 2017. **4**(16): p. 1700203.

Appendix

A.1 Compariason of one-batch and two batch synthesized CS_5 microgels

The one-batch synthesized CS_5 microgels were prepared and purified following the protocol outlined in the Experiment section. The feeding amounts of NIPAM, BIS, KPS and SDS were 563.3 mg, 40.8 mg, 10.5 mg and 7 mg, respectively. The reaction mixture was dissolved in 100 mL water. The amount of functionalized SiO_2 particle dispersion used was 5639 µL with the number concentration of 0.077 µM. The two-batch synthesized CS_5 microgels here were used in this work.

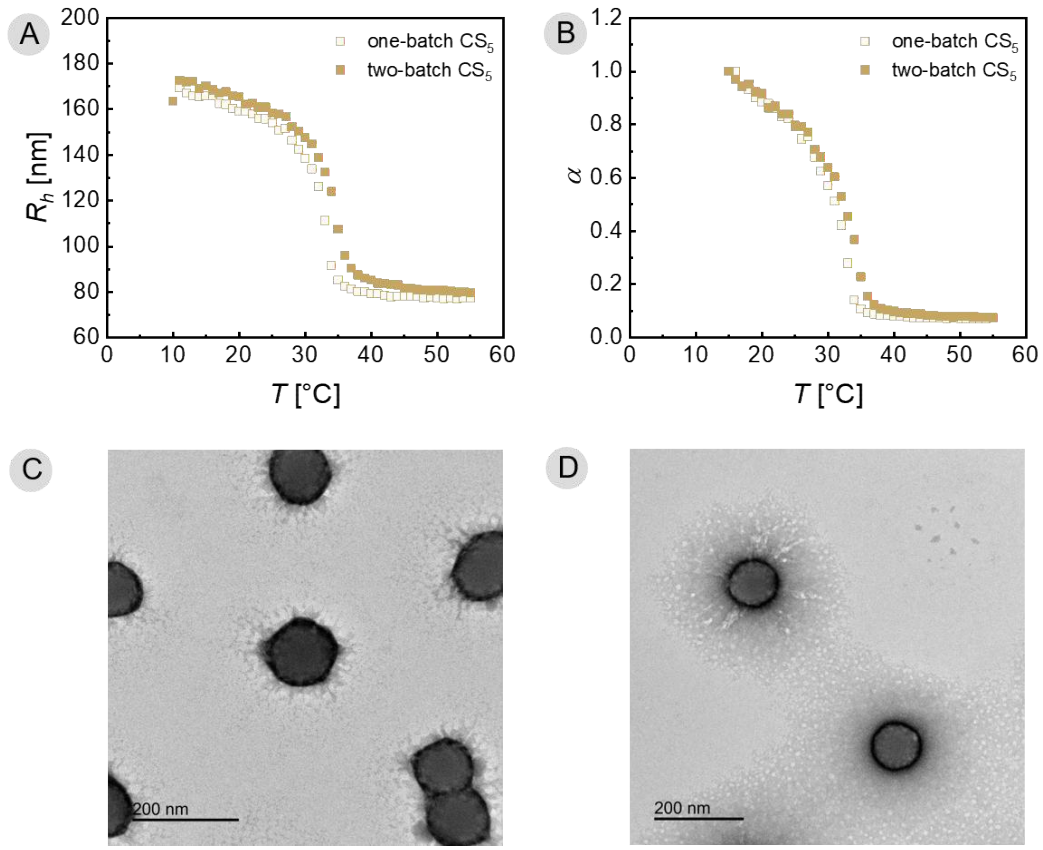

Figure A. 1. (A). The temperature-dependent DLS measurements of one-batch and two-batch synthesized CS_5 microgels; (B) The de-welling ratio, α, as a function of temperature. The TEM images of stained one-batch and two-batch synthesized CS_5 microgels are showed in (C) and (D), respectively.

A.2 TEM images of the silica core and CS microgels

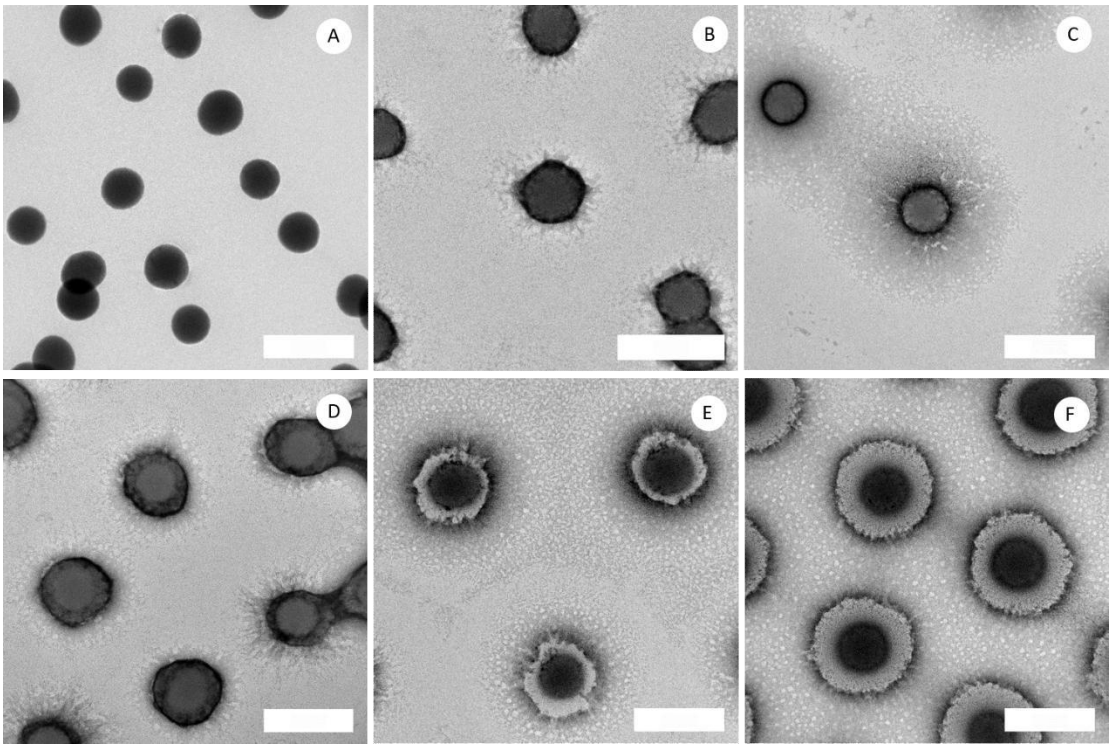

Figure A. 2. TEM images of unstained silica core (A) and stained CS microgel with different cross-link densities (from B to F, the cross-link densities are 2.5 mol%, 5 mol%, 7.5 mol%, 10 mol% and 15 mol%, respectively). The scale bars correspond to 200 nm.

A.3 Internal structure of the CS microgels

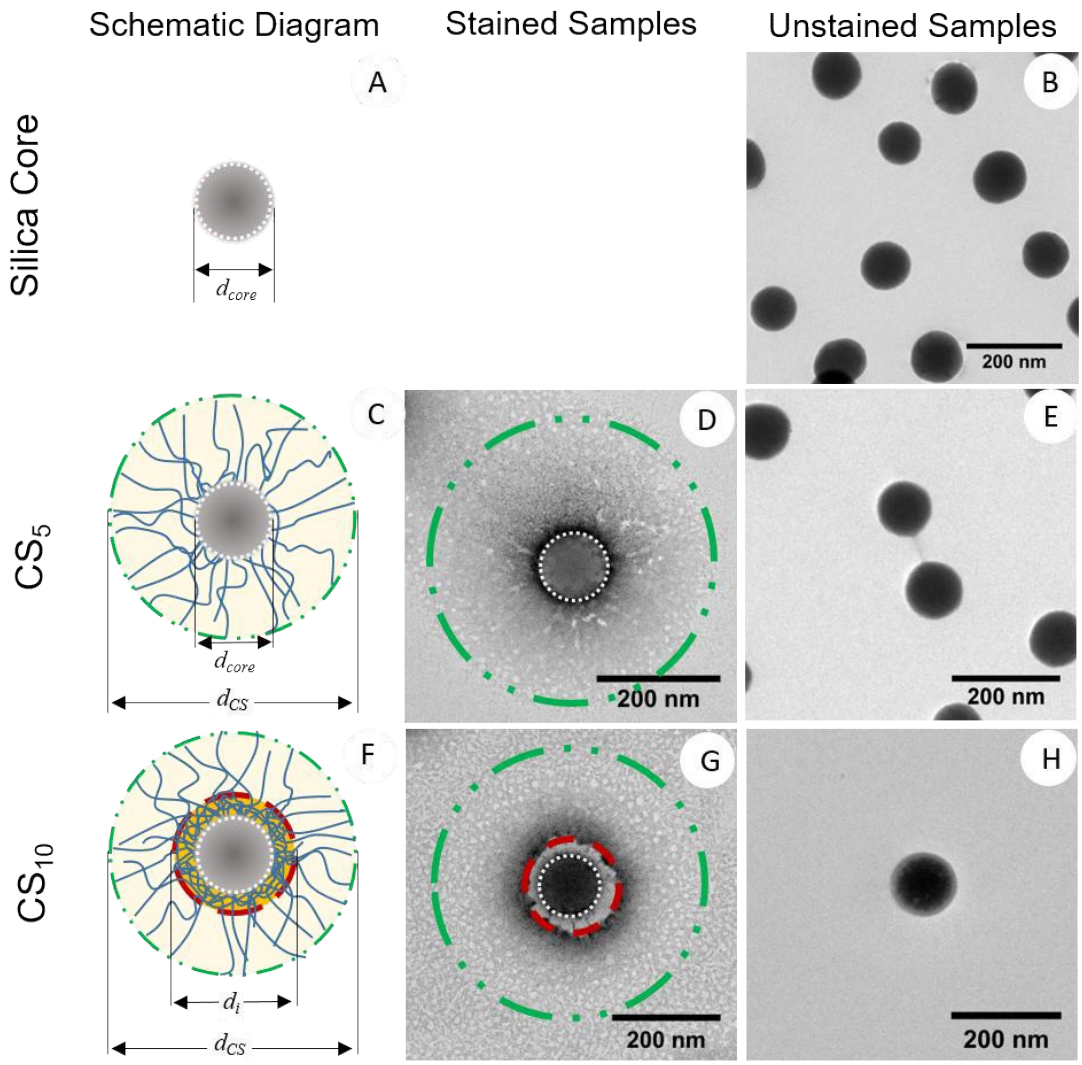

Figure A. 3. TEM images and schematic diagrams of the silica cores and the CS_5 and CS_{10} microgels. (A, C, F) Schematic illustrations of the silica core microgels. The silica cores (white dotted circle) are in the centre of the CS microgels. The higher cross-linked inner shell (red dotted circle, d_i) of CS_{10} is surrounded by a loosely lower cross-linked outer shell (green dotted circle, d_{cs}); (D, G). The TEM images of CS_{10} and CS_{10} microgels stained with uranyl acetate and dried in room temperature; (E, H) TEM images recorded from the CS_{10} and CS_{10} microgels without staining.

A.4 Calculation of N_p

The number of microgels in the monolayer was determined by analyzing AFM images of monolayers transferred at compression state II. N_p was obtained from the scanned area of these images, and their densities $N_p/Area$ were calculated. At least three AFM images captured from different points at compression state II were analyzed to calcu-

late the average of $N_p/Area$. Since at compression state II it is ensured that the distribution of the microgels is homogeneous, and the interface is fully covered by the monolayer, this density is multiplied by the monolayer area to estimate total N_p. Here, the monolayer area equals to the area between the Langmuir-Blodgett Trough's two barriers. The estimated total N_p is further used to plot the isotherm based on the assumption that the total N_p does not change during compression. Therefore, at other compression states, the estimated N_p /area was calculated using total N_p estimated at compression state II divided by area corresponding to that compression state. It's worth noting that at high compression states, the N_p/Area calculated from the AFM images was significantly lower than the expected N_p/Area corresponding to that surface pressure. This discrepancy suggests the possibility that microgels might desorb from the interface during compression, impacting the accuracy of the plotted isotherm.

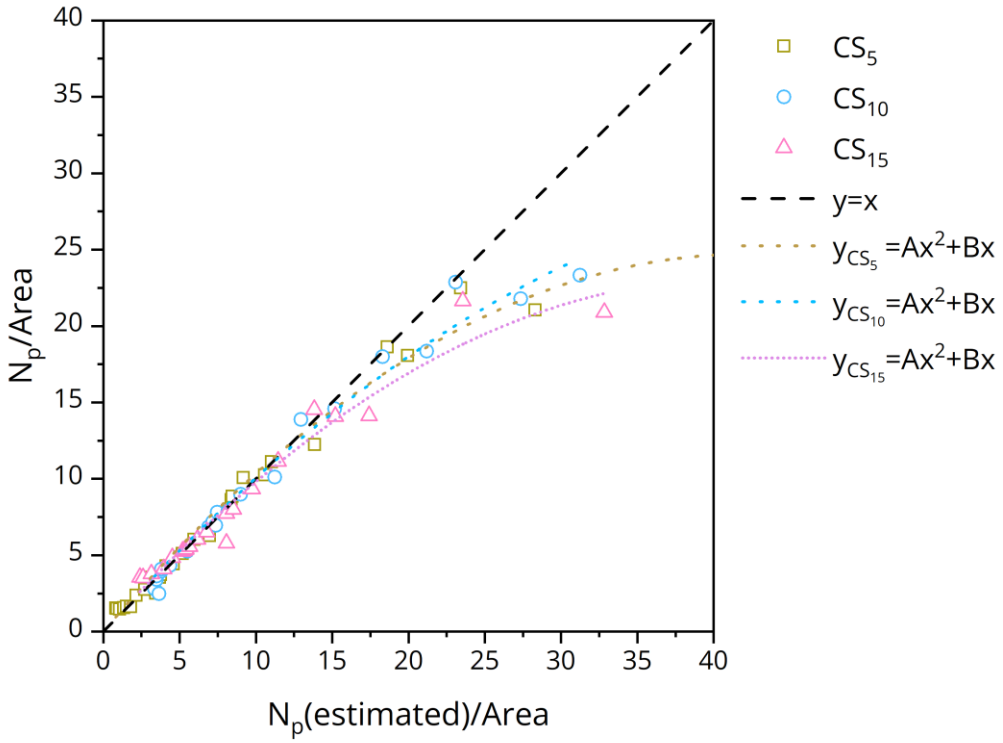

Figure A. 4. The correlation analysis of the theoretical and actual relationship between the estimated N_p/Area and N_p/Area. The x-axis and y-axis represent the estimated N_p/Area at a specific surface pressure and the N_p/Area calculated from AFM images of the monolayer transferred at the same surface pressure.

A.5 Compression isotherms

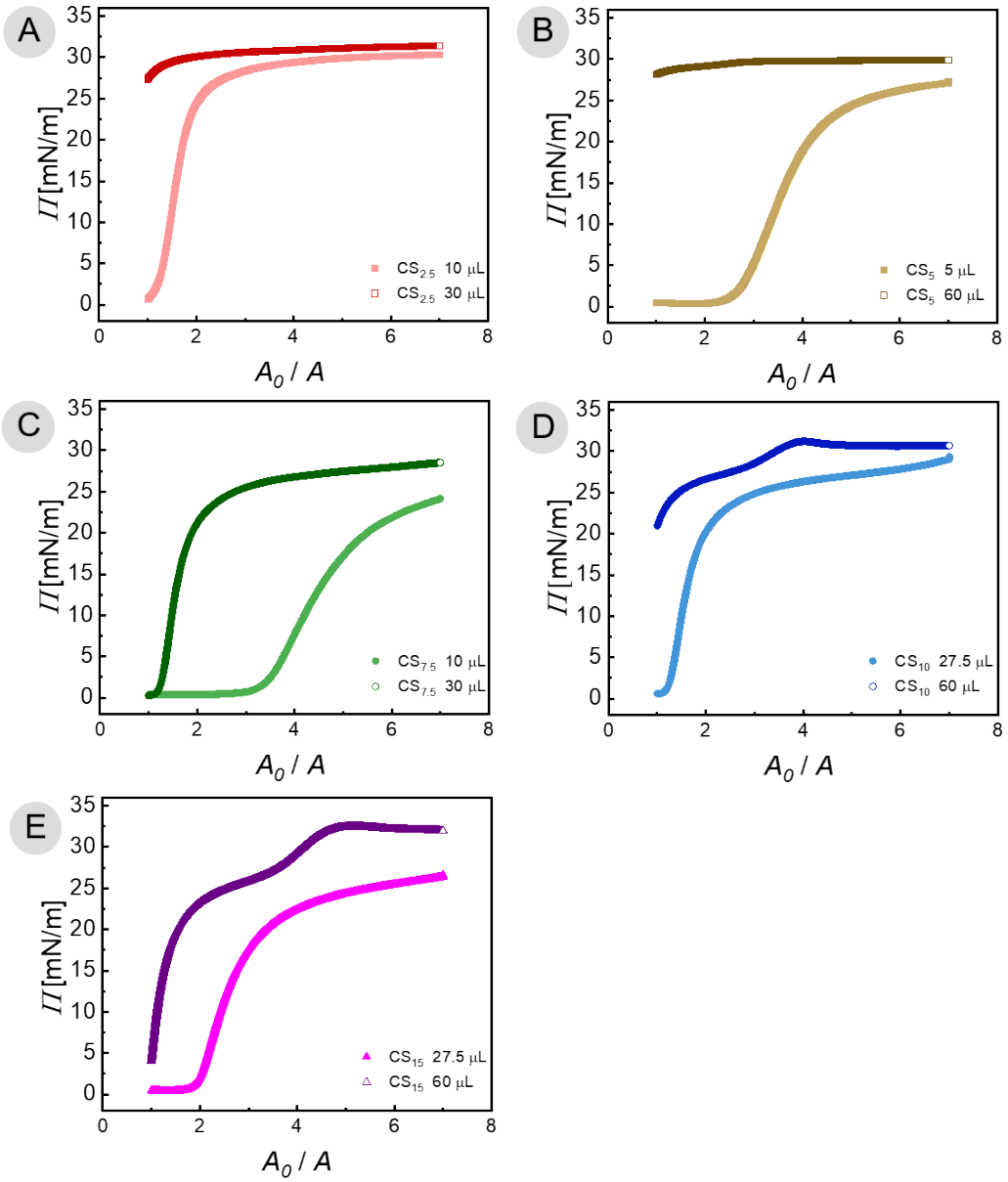

Figure A. 5. The compression isotherms of $CS_{2.5}$, CS_5, $CS_{7.5}$, CS_{10} and CS_{15} microgels are presented in the form of A_0/A versus Π in (A) to (E), respectively. The isotherms depict the surface pressure measured upon injecting relative amounts of 1 wt% microgel suspensions. Here A represent the area between the two barriers in the Langmuir-Blodgett trough, A_0 represent the initial area.

A.6 Absorption experiment of linear PNIPAM at the air/water interface

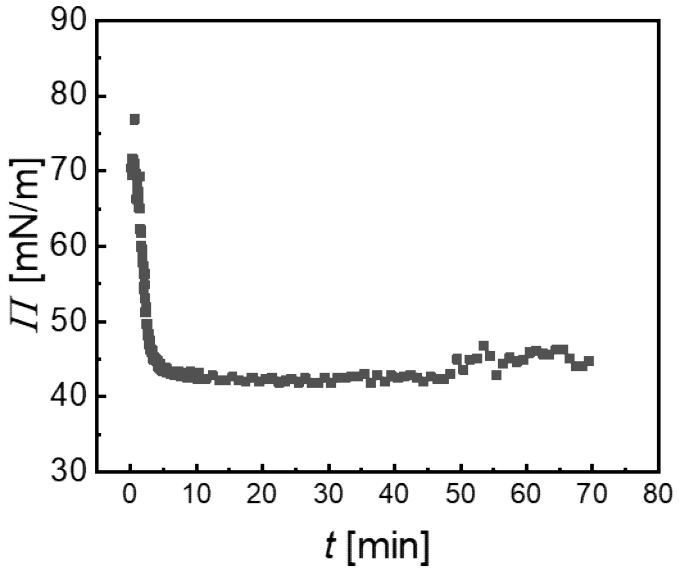

Figure A. 6. The surface tension as a function of time for a 0.001 wt% aqueous solution of linear PNIPAM, measured as a 'naked' drop in air.

A.7 Simulation of the spherical core-shell microgels

A.7.1 Computational details

Dissipative Particle Dynamics (DPD) simulations have been employed to investigate CS microgels with diverse architectures adsorbed at the interface. The study is basedon an extended DPD parametrization model for fluids and bead-spring models representing entangled macromolecules. The investigation delves into the distinctive features and general trends governing the evolution of structure and morphology in ensembles of CS microgels under compression.

Specifically focusing on PNIPAM-based microgels in proximity to the air-water interface, four distinct types of coarse-grained particles are considered: water (W) beads, air (A) beads, core (C) beads and polymeric (S) beads, forming microgel shell with varying architectures. A comprehensive description of the computer simulation design

of 5, 10 and 15% cross-linked microgels, namely CS_5, CS_{10}, and CS_{15}, respectively, can be found in the Supporting Information (Synthesis section, chapters 2.1-2.3).

The system was mapped based on the fluid particle model using the water-mapping scheme with a coarse-graining degree, $N_m = 4$. In this configuration, each bead possesses mass (m, except air beads, which was 0.001m), volume (V), and an effective size (r_c) corresponding to that of a cluster of four water molecules.

The interactions among beads are governed by potentials, expressed in units of thermal energy (k_BT), with their impact diminishing to zero at distances exceeding r_c. We conducted an extensive parametrization of W-S, A-S, and W-A interactions. and succinctly summarized in **Appendix A.7**. Additionally, we used an advanced conservative force model to capture interactions between liquid and gas beads, W-A. This model demonstrates a promising tool for reproducing the experimental values of the surface tension coefficient and density variation of air/water across their interface.

The simulations of the compression of the monolayers were performed as follows: swollen microgels ($N_p = 16$) of the same architecture were randomly placed near the air/water interface. A sufficiently large simulation box was used to ensure that the microgels did not touch each other after adsorption. Similar to the experiment, we characterized the compression state by the inverse area per particle, $N_p/Area = N_p / (L_x \cdot L_y)$, where L_x, L_y are the dimensions of the simulation box in X and Y directions. The first point we started modeling monolayers was $N_p/Area = 2.4 \cdot 10^{-4} r_c^{-2}$. After equilibration, the simulation box was gradually compressed along the x- and y-axis simultaneously. 12 cycles of compression until reaching $N_p/Area = 25.0 \cdot 10^{-4} r_c^{-2}$ had been performed. For clarity, we will indicate the compression state with index *(i)*

where $i \in [1; 13]$. An increase in i specifies area reduction and states with higher surface pressure. The indexes i are consistent across all the figures.

Interfacial tension coefficient (IFT). The DPD interfacial tension, γ_{DPD}, of the coexisting air-liquid phases was calculated using the diagonal components of the local pressure[32,33]:

$$\gamma_{DPD} = \int_0^{L_z} < \Delta p(z) > dz. \quad \text{(A. 1)}$$

where L_Z is the length of the simulation box in the direction normal to the interface, $\Delta p\ (z)$ is a difference in the normal and tangential components of the pressure tensor with respect to the interface, angle brackets indicate the ensemble(time) average.

$$\Delta p(z) = p_{\perp}(z) - p_{\parallel}(z) = p_{zz}(z) - \frac{1}{2}[p_{xx}(z) + p_{yy}(z)] \quad \text{(A. 2)}$$

where rescaled $z = z/r_c$ and $p_{zz}(z),\ p_{xx}(z),\ p_{yy}(z)$ are diagonal components of the local dimensionless pressure tensors calculated using the Irving-Kirkwood formalism [32,33]. Subsequently, the surface pressure change is calculated as

$$\Pi = \gamma_{DPD,\ pure} - \gamma_{DPD,\ microgel}, \quad \text{(A. 3)}$$

where $\gamma_{DPD,\ pure}$ is the interfacial tension of the bare liquid interfaces.

The evaluated γ_{DPD} and Π are in DPD units. It can be converted into real units measured experimentally, via

$$\gamma[mN/m] = (k_B T/{r_c}^2) \cdot \gamma_{DPD} \quad \text{(A. 4)}$$

Order parameters. To assess the structural difference between random and hexatic phases of the monolayers of microgels, we used the two-dimensional sixfold bond orientation order parameter calculated by the following expression:

$$\langle \boldsymbol{\Psi_6} \rangle = \left\langle \left| \frac{1}{N} \sum_{k=1}^{N} \psi_6^k (\boldsymbol{r_k}) \right| \right\rangle \quad \text{(A. 5)}$$

where $\psi_6^k(\boldsymbol{r_k})$ is the local orientational order parameter vector corresponding to the microgel k:

$$\psi_6^k(\boldsymbol{r_k}) = \frac{1}{N_k} \sum_{j=1}^{N_k} exp(\, i6\theta_{kj}) \quad \text{(A. 6)}$$

where θ_{kj} is the angle between the vector connecting the centres of masses microgel k with its neighbor j and a chosen fixed reference vector. N_k is the number of first neighbors for microgel k based on the Voronoi tessellation of the system. The $|\langle \Psi_6 \rangle|$ characterize the degree of hexagonal ordering of the particles in the monolayer so it is equal to zero in a fully disordered state and to one in the case of the perfect hexagonal phase[34].

Three core-shell microgels with a spherical solid core and inhomogeneous polymeric shells, CS_5, CS_{10} and CS_{15}, have been prepared. Indexes 5,10 and 15 represent the average fraction of cross-linkers % in the polymeric shells. The core-shell microgels were designed as follows. A unit cell of the diamond crystal lattice where the vertexes correspond to tetrafunctional cross-linkers was constructed. Then two cubic supercells S50 and S25 consisting of 50 × 50 × 50- and 25 × 25 × 25-unit cells, respectively, were assembled. Supercell S50 is considered as a template for the solid nanoparticle, while S25 is used as a template for the polymeric shell.

In the experiment, the MPS-modified silica core has a spherical shape of the diameter d_{core} = 105 ± 6 nm regardless of the sample. Similarly, same size spherical solid nanoparticle has been created, see **Table A. 1**. It was constructed by inscribing the spherically shaped frame into S50 supercell and cropping all the beads which are outside of the sphere. Beads forming the nanoparticle are denoted by C.

Table A. 1. Characteristics of the core-shell microgels with an anisotropic distribution of cross-links.

sample	Core	Inner shell				Outer shell				Shell(Total)	
	N_{beads}	N_{beads}	$N_{cross\text{-}links}$	$\bar{l}$	σ_l	N_{beads}	$N_{cross\text{-}links}$	$\bar{l}$	σ_l	N_{total}	% cross-links
CS_5	3020	1572	192	7	1	7978	222	12	1	9550	4.3
CS_{10}	3020	4342	778	3	1	12654	810	6	1	16996	9.4
CS_{15}	3020	4413	1295	2	1	17916	2112	3	1	22329	15.2

DLS measurements reveal the average hydrodynamic diameter, d_h, of the samples $CS_{2.5}$ - CS_{15} in the swollen state (T = 25 ˚C) of approximately 300 nm. To be precise the values are, d_h = 306 ± S_5, d_h = 316 ± 5 nm for CS_{10} and d_h = 305 ± 7 nm for CS_{15}. TEM images of the CS microgels, stained by uranyl acetate, demonstrate a double-layer structure of the polymer shell: a highly cross-linked inner and a less cross-linked outer region (**Figure A. 2**). The shell of the CS_5 microgels has practically no highly cross-linked inner parts and is mainly composed of a homogeneous fuzzy outer part. The thickness and the cross-linker density of the inner region of the shell increased for the CS_{10} and CS_{15} samples, respectively.

To be consistent with experimental observations, polymeric shell of the samples CS_5, CS_{10} and CS_{15} with inhomogeneous cross-link distribution in the inner and outer regions in a simulation was created. A scaled S25 supercell was used to construct the polymeric shell around the solid nanoparticle. All the bonds between the tetrafunctional atoms were replaced by polymer subchains of different lengths. The length of

the subchains determines the degree of a cross-link of the microgel: the shorter the subchains, the higher the cross-link density of the microgel and vice versa. Different laws can describe the distribution of the chain lengths. We will use symmetric Gaussian distribution with an average value of $\bar{l}$, and a standard deviation of σ_l. $\sigma_l = 0$ corresponds to the case of an ideal diamond-like network used in many simulations. The higher the value of σ_l the stronger the discrepancy of the network from the ideal regular structure. Then three spherical frames of different radii were inscribed into the modified supercell. The small frame is necessary for forming the void in the polymeric network of the same size as the solid nanoparticle one. The sizes of the middle, R_M, and large, R_L, frames control the thickness of the polymeric shell's inner and outer regions, respectively. All beads were cropped inside the small and outside of the large ellipsoidal frames. The rest of the beads forming the microgel shell was denoted as S. Pair of ($\bar{l}_{in}$, σ_{in}) and ($\bar{l}_{out}$, σ_{out}) sets the distribution of the cross-linkers within the regions. Such a procedure allows us to synthesize various polymeric shells with highly cross-linked inner parts and gradually decreasing cross-linker concentration towards the outer part. The solid nanoparticle was inserted into the void of the microgel with further grafting of the dangling chains of the polymeric shell to the nanoparticle surface. The dangling chains of the polymeric shell were physically attached to the nanoparticle surface. Going through all of the free ends of the dangling chains, we monitor whether the distance between it and the closest bead at the surface of the solid core satisfies the condition: $|r_{end} - r_{surf}| \leqslant r_c$. If so, a bond between the free end of the dangling chains and the bead of the surface of the solid core was formed. Only one bond could be formed between the free end and the solid core.

As a result of the self-consistent sampling of the radii ($\bar{l}_{in}$, σ_{in}) and ($\bar{l}_{out}$, σ_{out}) it was succeeded in obtaining the microgels which demonstrate similar to the experimental

sample a) ratio between the sizes of the core and the shell and b) swelling behaviour and size changes in bulk as a function of the temperature. The resulting parameters and characteristics are presented in **Table A. 1.**

A.7.2 Coarse-grain levels

One of the most important parameters that can be tuned within a DPD simulation is the interaction parameters a_{ii} and a_{ij} describing repulsions between similar and dissimilar unbonded DPD beads, respectively. The interaction parameters are expressed in units of k_BT/r_c. There are several methodologies to choose it to describe phase separating fluids or fluid mixtures. Following the parametrization method employed by Groot and Warren and Maiti & McGrother, one could represent a DPD particle as a multiple, N_m liquid molecules. Based on the assumption of $a_{ii} = a_{jj}$, $r_{c,i} = r_{c,j}$ and maintaining the constant density in the box, the DPD a_{ij} parameters could be related to the Flory-Huggins theory:

$$a_{ij} = (a_{ii} + 3.27\chi_{ij})k_BT/r_c \quad \text{(A. 7)}$$

To preserve the compressibility of liquid, κ^{-1}, at different coarse-grained levels, a_{ii} has to be related to the density, ρ_{DPD}, within the simulation box and to the degree of coarse-graining, N_m, as

$$a_{ii} = k_BT\,\frac{\kappa^{-1}N_m - 1}{2\alpha\rho_{DPD}} \quad \text{(A. 8)}$$

where α is considered to be a constant equal to 0.1 and independent of ρ_{DPD} and a_{ii}. We set the total number density of the system as $\rho_{DPD} = 3{r_c}^{-3}$. Using a water-mapping scheme, $\kappa^{-1} = 16.15$, and the degree of coarse-graining $N_m = 4$, the interaction parameters between the beads of the same species $a_{ii} = 106.5k_BT/r_c$. The

characteristic size and molecular weight of the single bead, r_c = 0.71 nm and m = 72 Da.

There are four different types of particles in our system: water (W), Air (A), the beads forming the microgel shell (S), and the solid core (C). Thus, it is necessary to set all a_{ij} where i and j ∈ (W, A, S, C) to establish the interactions between the different constituents. The properties of all types of beads are summarized in Table A. 2.

Table A. 2. DPD Conservative Repulsion Parameters a_{ij}* and Bond Parameters.

conservative repulsion parameters a_{ij} (k_BT/r_c), T = 25°C*					
bead type	fragment	**C**	**S**	**W**	**A**
C	silica core	106.5			
S	NIPAm shell	116	106.5		
W	water	120	106.5	106.5	
A	air, a_{Aj}	25.6	25.6	25.6	106.5
	b_{Aj}	20	20	20	n/a
bond parameters, $\boldsymbol{U_{ij}^{bonds}}$					
bond	bond type	$K_b(k_BT/r_c^2)$		$r_0(r_C)$	
S-S, S-C	harmonic	10		0.7	
C-C	harmonic	100		0.7	
angle parameters, $\boldsymbol{U_{ij}^{angles}}$					
angle	angle type	$K_a(k_BT/r_c^2)$		θ_0	
C-C-C	harmonic	100		109.47	

Parameters a_{Aj} and b_{Aj} for j ≠ A correspond to the hard-core interaction force (equation A. 11).

A.7.3 Parametrization of Liquid/Microgel interaction

We constructed a series of microgels having different radii ($\bar{l}_{in}$, σ_{in}) and ($\bar{l}_{out}$, σ_{out}) and tried to find out a reliable set of parameters to reproduce the swelling/deswelling behavior of the microgels CS_5, CS_{10} and CS_{15}.

To model the subchains in the microgel shell and the solid core, we use a bead-spring model where DPD beads are connected using a harmonic bond potential. The bond potential is given by

$$U_{ij}^{bonds} = K_{b,ij}(r_{ij} - r_{0,ij})^2 \quad \text{(A. 9)}$$

where $k_{bond\,ij}$ is the bond stiffness, and r_0 is the equilibrium bond length.

The angle potential, which is necessary to prevent the solid particles from deformation at the interfaces upon compression, is given by

$$U_{ijk}^{angles} = K_{a,ij}(\theta - \theta_{0,ijk}) \quad \text{(A. 10)}$$

where $K_{a,ij}$ is the bending stiffness, and θ_0 is the angle between two pairs of connected beads sharing a common bead.

At T = 25 ˚C NIPAM based microgels in water are fully swollen. Thus, polymeric shell – water, S – W, interaction is favorable with mismatch parameter $\Delta a_{SW} = a_{SW} - a_{ii} = 0$, where a_{ii} are the interaction parameters between the beads of the same species $a_{ii} = 106.5k_BT/r_c$. The interaction parameters between solid core (C) and polymeric shell (S) beads $a_{CS} = 116k_BT/r_c$ allow mimicking the moderate incapability of the core and shell beads. While the C−W interaction is unfavorable with $\Delta a_{CW} = 13.5k_BT/r_c$. To model the swelling/deswelling process, we alter the poly-

mer-liquid repulsion a_{SW} in a range between $a_{SW} = 106.5k_BT/r_c$ and $a_{SW} = 115k_BT/r_c$

The simulations of the swelling/deswelling process of CS_5, CS_{10}, and CS_{15} of different architectures in a water solution were performed in the NVT ensemble in cubic boxes of a constant volume V = Lx × Ly × Lz = 60 × 60 × 60 r_c^3 with periodic boundary conditions in all directions. The necessary amount of water beads, W, was added to the simulation box. The friction coefficient γ was 3.0. The equations of motion are integrated in time with a modified velocity-Verlet algorithm with a time step $\Delta t = 0.01\tau$, where $\tau = r_c(m/k_BT)^{1/2}$. The equilibration run comprised 10^6 steps followed by a production phase comprising 10^6 steps. The gyration radius, hydrodynamic radius, and density profiles were averaged over the production run.

A.7.4 Liquid/Gas DPD Model

It is worth noting that the beads described by the regular DPD force have a soft-core repulsive nature. The DPD equation of state is quadratic in density that prohibits the real gas/liquid coexistence as well as the sharp variation of the density of the beads at the gas/liquid interface. Nevertheless, similar to the free volume approaches in the self-consistent field theory (SCFT), it is possible to represent the gas phase in DPD as built of fictitious bubble beads, having hard-core nature. Parametrization of the model provides the ability to mimic the density variation across the gas/liquid interface as well as the gas−liquid surface tension of reference systems.

To simulate the air phase (A), we use the following assumptions. A-bead has the same size and number density as the other beads. The A−A interaction is described by the original soft-core linear repulsive force with $a_{AA} = a_{ii} = 106.5k_BT/r_c$. The mass of the A-bead is equal to 0.015m to keep the relative mass density in correspondence to

the water beads. The form of the conservative repulsive force between the A-bead and all nonA-beads has undergone a noticeable change. Soft pairwise linearly decaying force has been replaced by the exponential pairwise force of the following form:

$$\boldsymbol{F}_{Aj}^{exp} = \begin{cases} a_{Aj}\left(\frac{e^{b_{Aj}}-e^{b_{Aj}}}{1-e^{b_{Aj}}}\right)\hat{\boldsymbol{r}}_{Gj}, & if\ r_{Aj} < r_c \\ 0 \end{cases} \qquad \text{(A. 11)}$$

where a_{Aj}, and b_{Aj} define the strength and the steepness of the force. The combination of the (a_{Aj}, b_{Aj}) allows to control of the overlapping limits of the beads and could represent both soft-particles at $b_{Aj} \to 0$ and hard-core particles at $b_{Aj} \to \infty$. The parameters a_{AW} and b_{AW} are properly matched with the experimental surface tension and interfacial density profiles of the water/air interface obtained by atomistic simulations. We tune the a_{Aj} and b_{Aj}, for j ∈ (S, C) by matching the reduction of surface tension after the adsorption of the linear PNIPAM polymers and PNIPAM-based microgels at the water/air interface (see Supporting Information). The resulting values of a_{Aj} and b_{Aj} parameters are shown in Table A. 2. Such a choice of parameters at 25 °C provides the value of the interfacial tension of pure water/air interface equal to 72 ± 3 mN/m, and reduction of surface tension after the adsorption of PNIPAM-based microgels to 30 ± 2 mN/m which is in good agreement with the experimental value 31 and 71.8 mN/m

For the fullness of the description, let us note that using regular DPD potential for A-beads will lead to the wrong interfacial density profiles and an underestimation of the air/water surface tension. For the current coarse-graining regime, $N_m = 4$, the interfacial tension of the water/air interface could not exceed 40 mN/m for any reasonable a_{AW} value.

A.7.5 Parametrization of Microgel/Gas Interactions

Using the gas phase model, a simulation of linear NIPAM polymer chains (consisting of S-beads) placed at the flat water/air interface has been performed to find an appropriate set of (a_{AS}, b_{AS}) parameters.

The simulations were performed in the NVT ensemble in rectangular boxes of a constant volume V = Lx × Ly × Lz = 100 × 100 × 25 r_c^3 with periodic boundary conditions in all directions. The water (W) and air (A) beads were placed at the bottom and top regions of the simulation box respectively. The W: A composition of beads is maintained constant at a ratio of 2:1. The resulting two parallel interfacial boundaries between the water and air beads were perpendicular to the z-axis. The linear PNIPAM chains were placed in the water phase near the top interface, while the bottom interface remains free. Adsorption of polymers at the interface took place to minimize the interfacial energy.

Several simulations were performed by varying the initial number of linear PNIPAM chains at the interface, and the interfacial surface tension (IFT) and surface pressure change were estimated using equation (A. 8) and equation (A. 9) respectively.

The friction coefficient was 3.0. The equations of motion are integrated in time with a modified velocity-Verlet algorithm with a time step $\Delta t = 0.01\,\tau$, where $\tau = r_c(m/k_BT)^{1/2}$. The equilibration run comprised of 10^6 steps followed by a production phase comprising 10^6 steps. The interfacial tension, and the surface area of polymers, were averaged over the production run.

The final values of (a_{AS} , b_{AS}) are shown in Table A. 2 which enable the pursuit of Π = 30 ± 2 mN/m for PNIPAM chains which is in good agreement with the experimental value.

A.8 Simulations of core-shell microgels in bulk and at the air/water interface

By analogy with experiments, we prepared three types of monolayers, consisting of either CS_5, CS_{10} and CS_{15} microgels. The microgel monolayers were formed by 16 microgels randomly placed at the air/water interface. The initial size of the simulation box was Lx × Ly × Lz = 260 × 260 × 50 r_c^3. The ratio between the numbers of water and air beads was 3:1, and the total number of beads in the simulation box was more than 10^7. 16 collapsed microgels have been located near the water/air interface. After the first equilibration for 2.5 × 10^6 steps, the systems were simultaneously compressed along the x- and y-axis. We perform N = 12 cycles of compression until the simulation boxes become Lx × Ly × Lz = 80 × 80 × 50r_c^3 . On each of the first 8 cycles, we gradually decrease Lx and Ly of the simulation box by 20r_c within the 0.5×10^6 timesteps. After the compression, the system was equilibrated during the 2.5×10^6 timesteps and the next stage of compression began. Compression was accompanied by removing the water and air beads while preserving the 3:1 ratio (Lz was constant). The last cycles, starting from Lx × Ly × Lz = 100 × 100 × 50r_c^3 Lx and Ly values of the simulation box were decreased by 5r_c within the 0.5×10^6 timesteps. After the compression, the system was equilibrated during the 2.5×10^6 timesteps and the next compression stage began. Compression was accompanied by changing Lz size, preserving the volume of the simulation box. Such a scheme is predicated on preserv-

ing enough space for the microgels in a water phase due to their mobility and deformation in a normal to the interface direction at a high compression degree.

We applied several criteria to judge the equilibrium in a system, including the equilibrium of energy, the equilibrium of gel sizes, and the equilibrium of the surface tension coefficient. We waited until values of all these characteristics reached a plateau, i.e., when they become invariable or have small fluctuation around the average value.

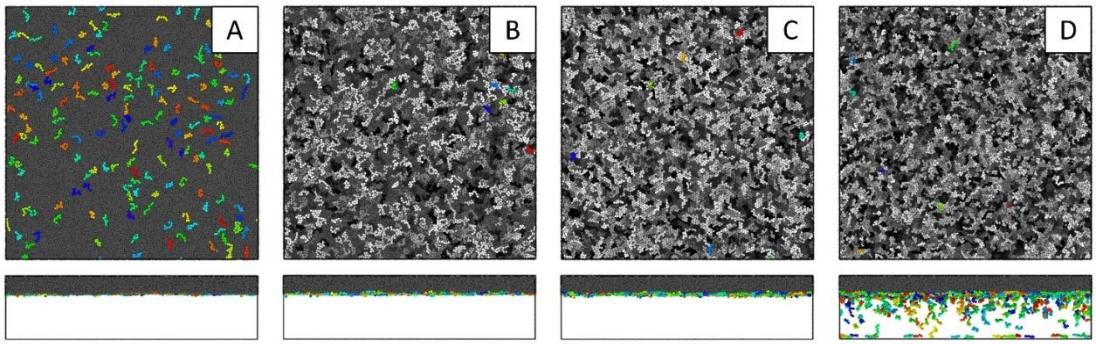

Figure A. 7. Snapshots of linear PNIPAM monolayers (L=8 beads) for different surface coverage, Ap = A), C), and D). View from the water phase and side view. For clarity, different linear chains are marked by rainbow colours.

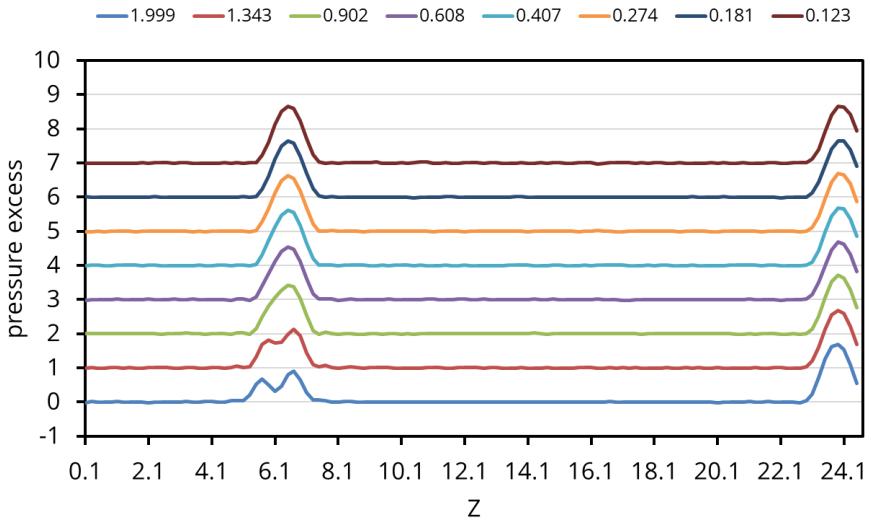

Figure A. 8. Pressure excess for the system of linear PNIPAM chains (L=8 beads) for different surface coverage as a function of normal coordinates perpendicular to the interfaces.

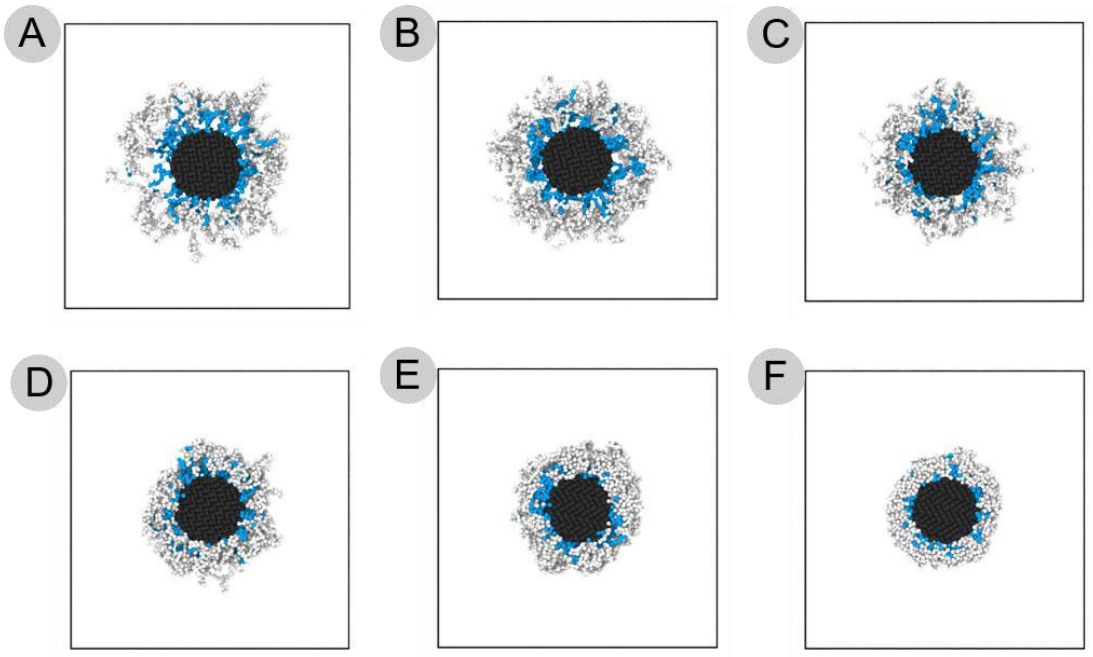

Figure A. 9. Equilibrium structure of the CS_5 microgels at different a_{SW} values: A) 106.5; B) 107.5; C) 108.5; D) 109.5; E)110.5; F) 115 k_BT/r_c. The cross-sections of the thickness of d = $2r_c$. Polymeric shell depicted in blue (inner region) and grey (outer region), solid nanoparticle – in black, water beads are not shown.

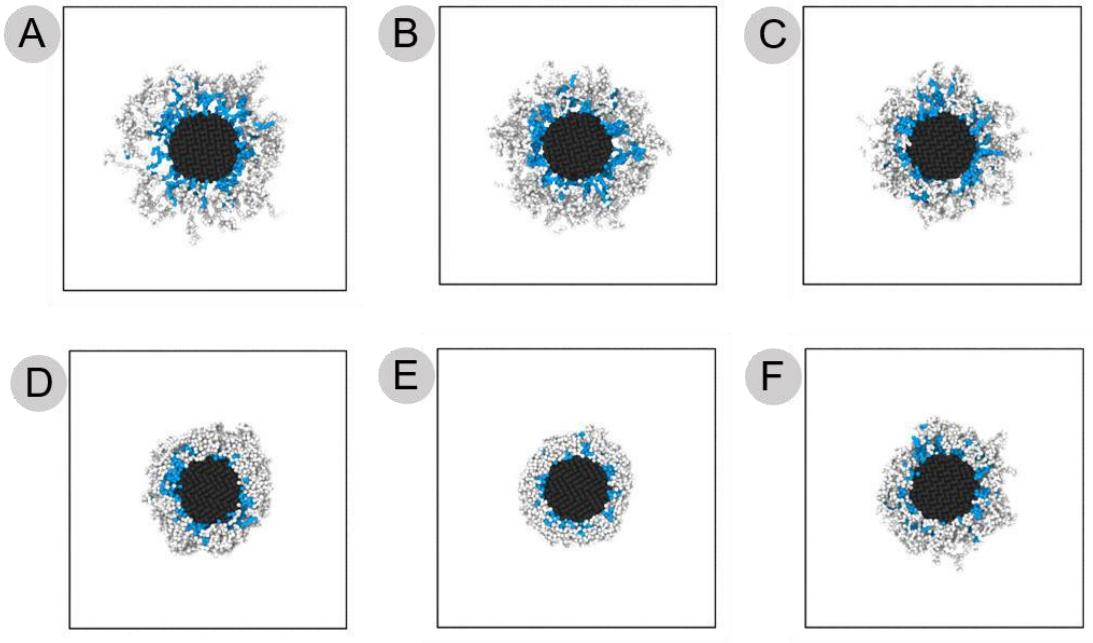

Figure A. 10. Equilibrium structure of the CS_{10} microgels at different a_{SW} values: A) 106.5; B) 107.5; C) 108.5; D) 109.5; E)110.5; F) 115 k_BT/r_c. The cross-sections of the thickness of $d = 2r_c$. Polymeric shell depicted in blue (inner region) and grey (outer region), solid nanoparticle – in black, water beads are not shown.

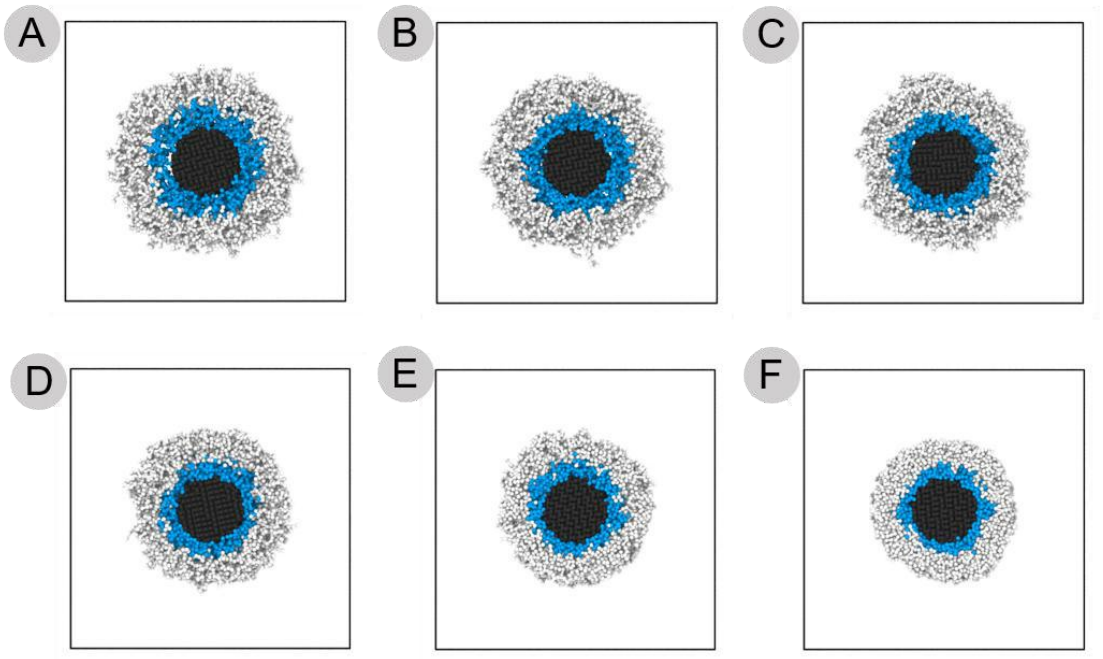

Figure A. 11. Equilibrium structure of the CS_{15} microgels at different a_{SW} values: A) 106.5; B) 107.5; C) 108.5; D) 109.5; E)110.5; F) 115 k_BT/r_c. The cross-sections of the thickness of $d = 2r_c$. Polymeric shell depicted in blue (inner region) and grey (outer region), solid nanoparticle (black), water beads are not shown.

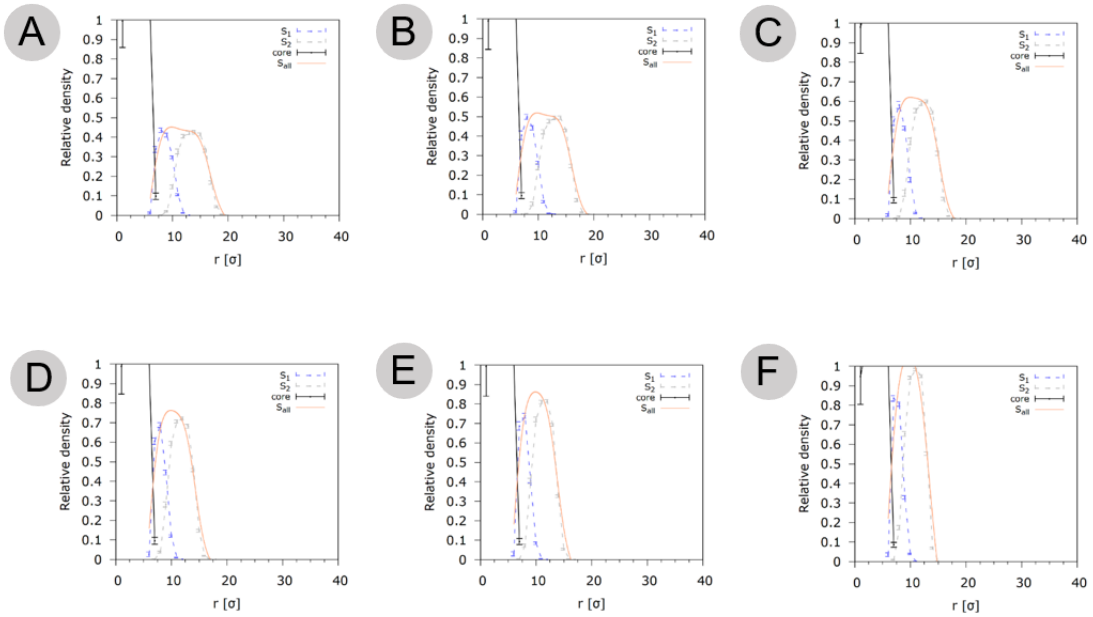

Figure A. 12. Relative density profiles as a function of the distance from centre of mass of the CS_{15} microgels at different a_{SW} values: A) 106.5; B) 107.5; C) 108.5; D) 109.5; E)110.5; F) 115 k_BT/r_c. Blue and grey curves correspond to the distribution of polymer, S, in the inner and outer region of the microgels. Orange curve is the overall polymeric distribution. Black curves represent the C-beads of the solid core.

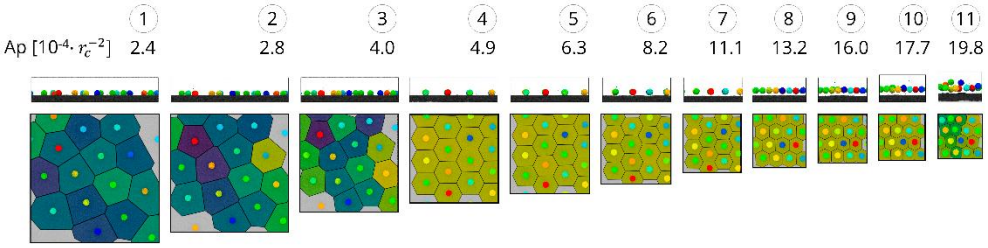

Figure A. 13. Snapshots of CS_{10} microgel monolayers for different degrees of compression (surface coverage). First row – side view. Second row – view from the waterside. Only cores and air phase are shown. For clarity, the cores of different microgels are marked by rainbow colours. Voronoi diagrams are presented, where each Voronoi cell was coloured by the value of the local orientational order parameter corresponding to the relevant cell, $|\psi_6^k(r_k)|$. The darker the colour the closer the $|\psi_6^k(r_k)|$ to 0.

A.9 Relative monomer density profiles in the lateral slices of the CS microgels

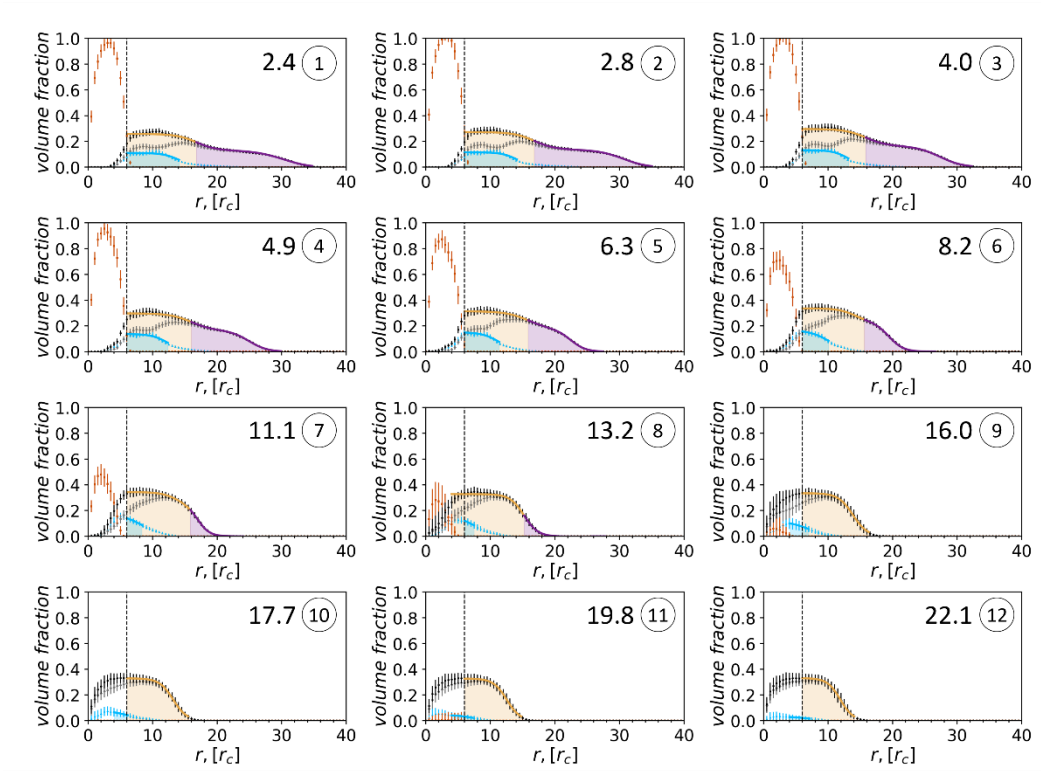

Figure A. 14. Relative monomer density profiles in the lateral slices of the CS_5 microgels at the air/water interface at different $A_p = N_p/Area$ values. The slices were made in the lateral direction of the interface. The thickness of the slices is equal to $4r_c$.

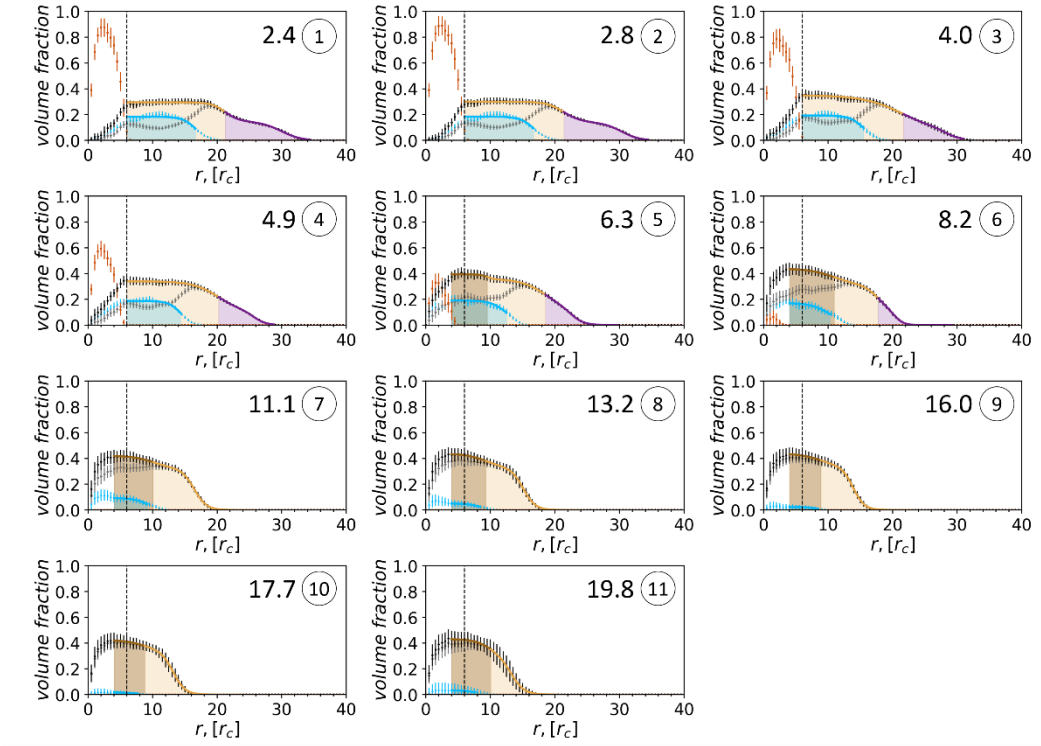

Figure A. 15. Relative monomer density profiles in the lateral slices of the CS_{10} microgels at the air/water interface at different $A_p = N_p/Area$ values. The slices were made in the lateral direction of the interface. The thickness of the slices is equal to $4r_c$.

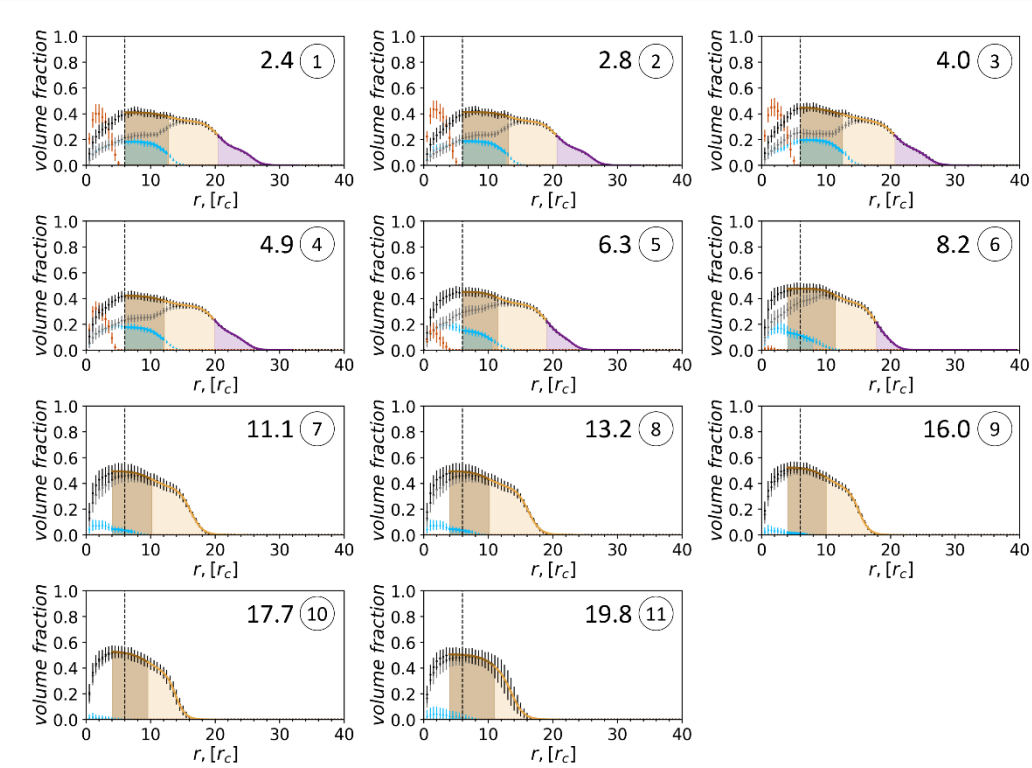

Figure A. 16. Relative monomer density profiles in the lateral slices of the CS_{15} microgels at the air/water interface at different $A_p = N_p/Area$ values. The slices were made in the lateral direction of the interface. The thickness of the slices is equal to $4r_c$.

A.10 Microgel monolayers Cluster analysis based on AFM images

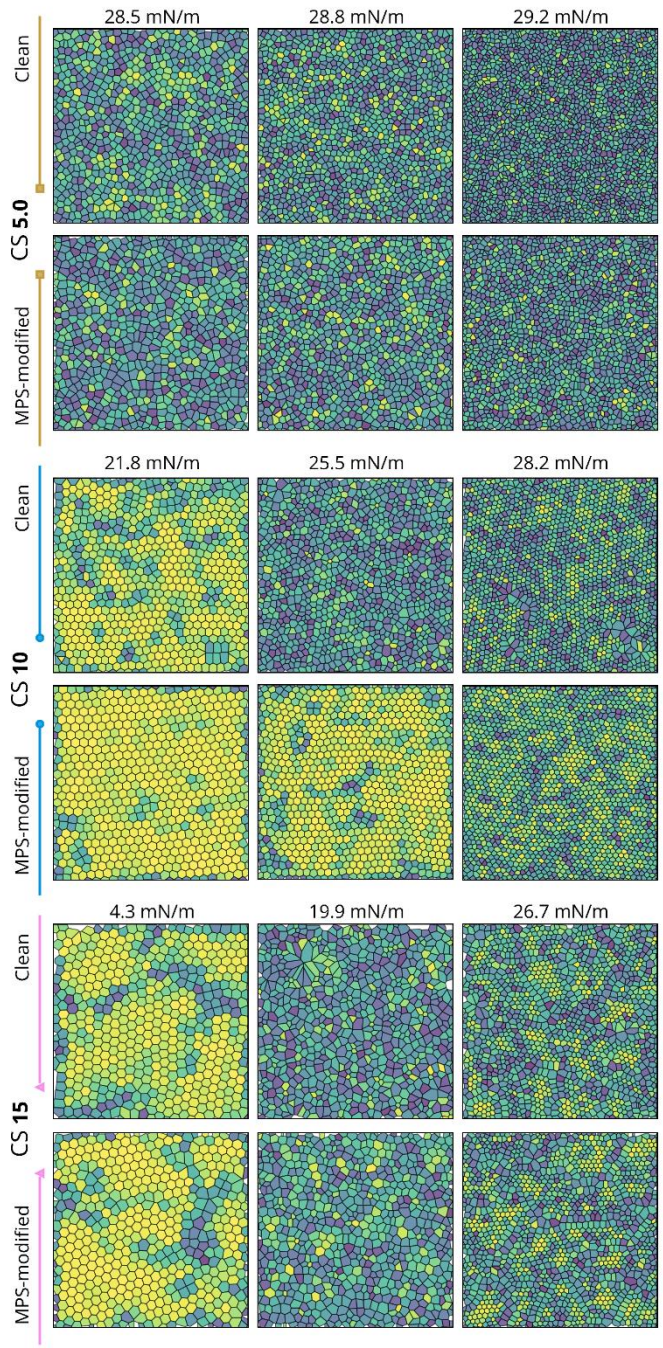

Figure A. 17. Voronoi diagram of the AFM height images of CS_5, CS_{10}, and CS_{15} monolayers deposited onto hydrophilic and hydrophobic (MPS-modified) glass substrates. Each Voronoi cell is coloured by the value of the local orientational order parameter corresponding to the relevant cell, $|\psi_6^k(r_k)|$, see equation (A. 6). The darker the colour, the closer the $|\psi_6^k(r_k)|$ to 0. The size of the AFM images is 10 µm × 10 µm.

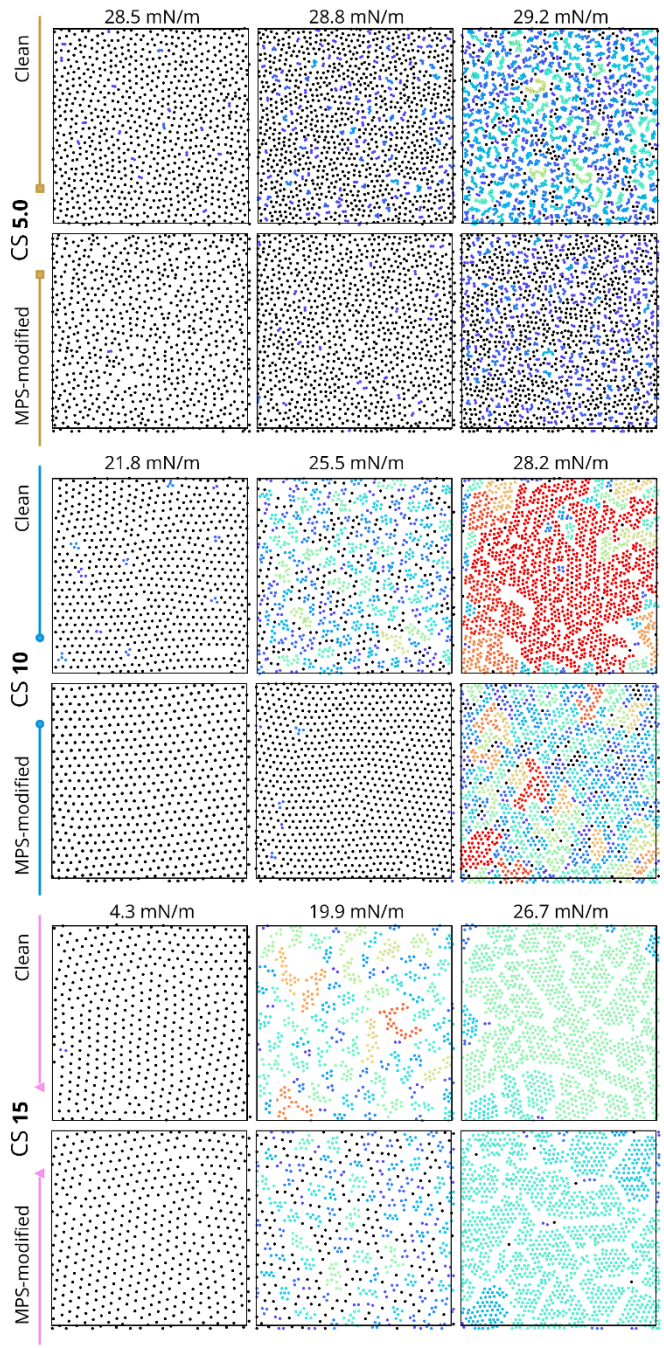

Figure A. 18. Cluster analysis of the microstructures of AFM height images of CS_5 (r_c = 150 nm), CS_{10} (r_c = 220 nm), and CS_{15} (r_c = 300 nm) monolayers deposited onto hydrophilic and hydrophobic (MPS-modified) glass substrates. The size of the AFM images is 10 µm × 10 µm. Black colour corresponds to the primitive cluster of a size of single particle.

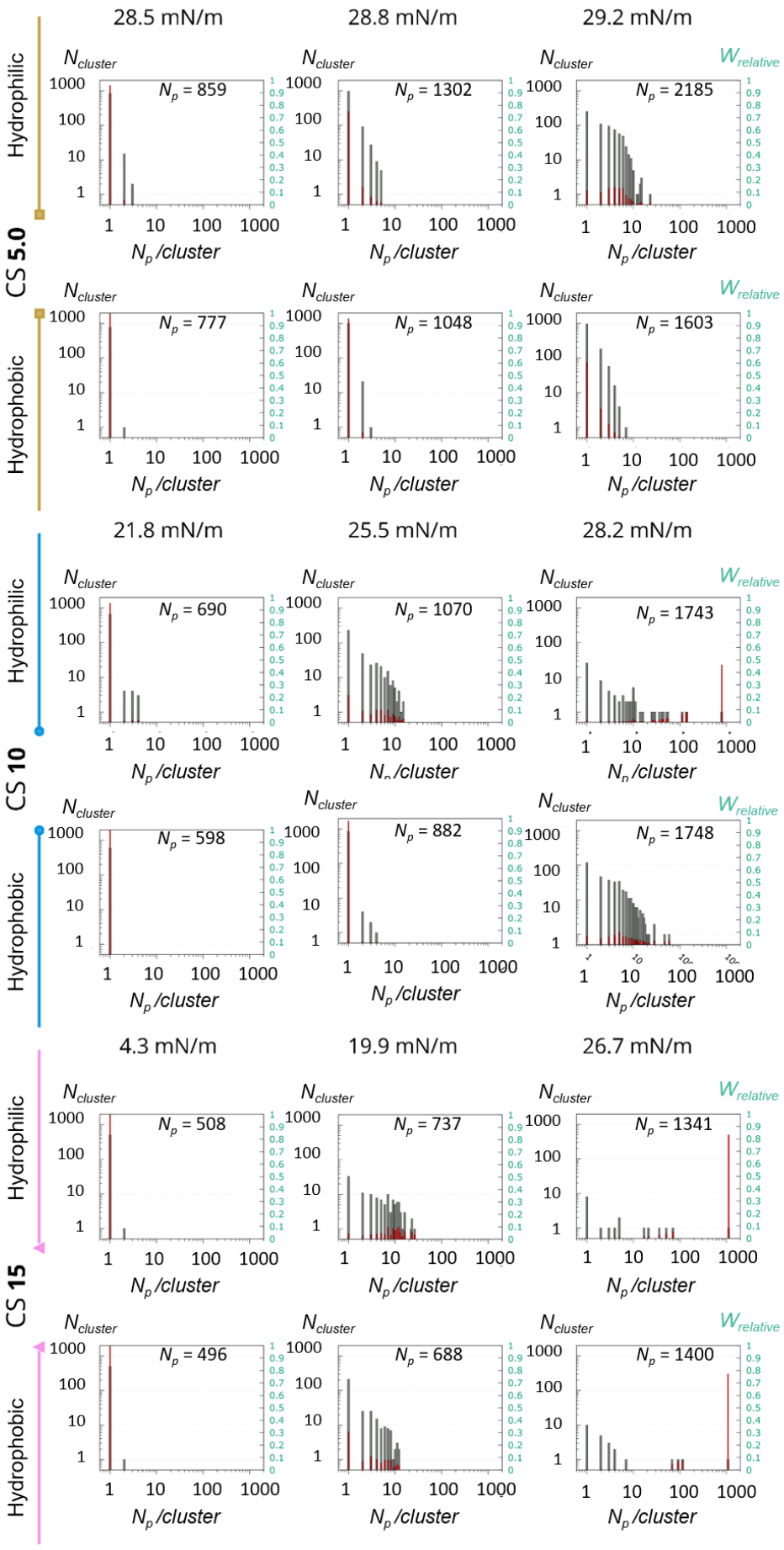
28.5 mN/m
28.8 mN/m
29.2 mN/m
Hydrophilic
CS 5.0
Hydrophobic
$N_{cluster}$
$W_{relative}$
N_p = 859
N_p = 1302
N_p = 2185
N_p = 777
N_p = 1048
N_p = 1603
N_p /cluster
21.8 mN/m
25.5 mN/m
28.2 mN/m
CS 10
N_p = 690
N_p = 1070
N_p = 1743
N_p = 598
N_p = 882
N_p = 1748
4.3 mN/m
19.9 mN/m
26.7 mN/m
CS 15
N_p = 508
N_p = 737
N_p = 1341
N_p = 496
N_p = 688
N_p = 1400

Figure A. 19. The related cluster analysis of the AFM images showed in **Figure 6. 12**. Black bars demonstrate number of the cluster. $N_{cluster}$, as a function of $N_p/cluster$. Red bars demonstrate the relative weight of certain cluster.

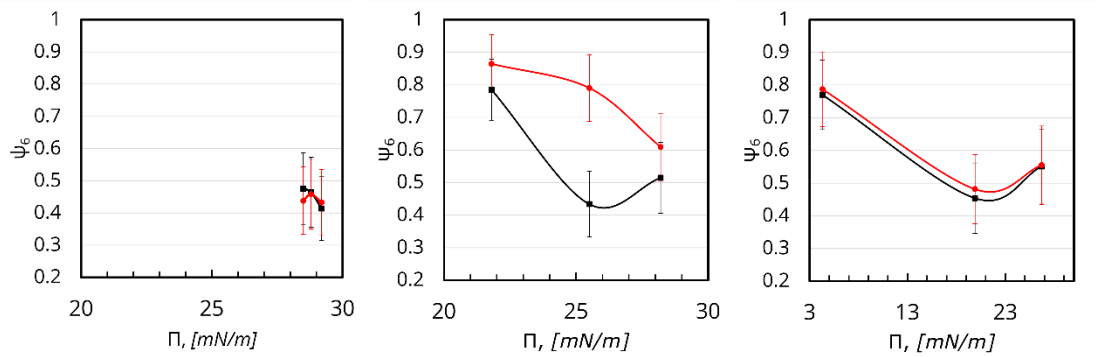

Figure A. 20. The hexagonal order parameters Ψ_6 for CS_5 (left), CS_{10} (middle) and CS_{15} (right) microgel monolayers transfterred to hydrophilic (red) and hydrophobic (black) glass substrates are plotted versus their surface pressure during transferred.

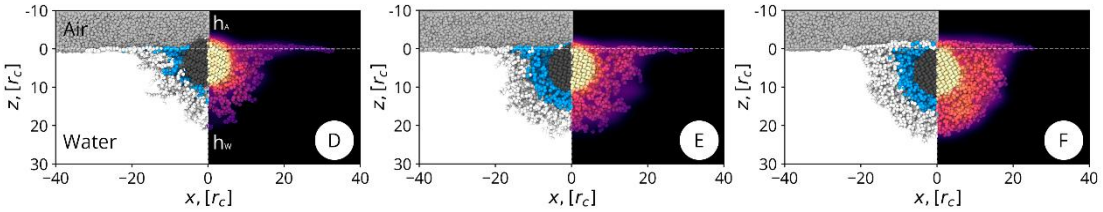

Figure A. 21. Snapshots of CS_5, CS_{10}, and CS_{15}, microgels at the air/water interface: (A-C) side view of cross-sections of thickness of $4r_c$ through the microgel`s centre of mass, polymeric density is colour-coded using an inferno scheme. Insets provide additional detail, recolouring the core, inner shell, and outer shell beads in black, blue, and white, respectively.